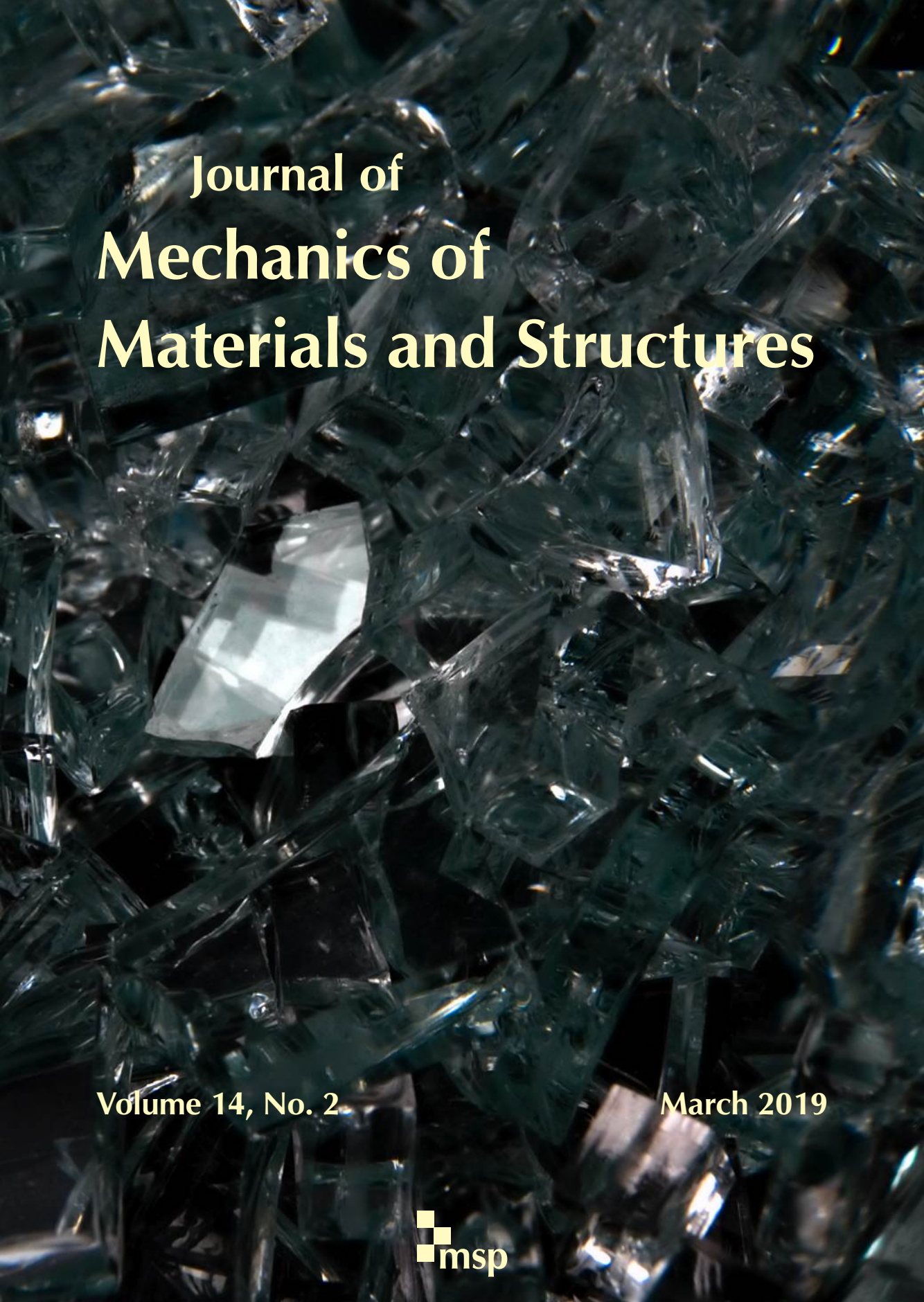

Journal of Mechanics of Materials and Structures

Volume 14, No. 2 March 2019

msp

JOURNAL OF MECHANICS OF MATERIALS AND STRUCTURES

msp.org/jomms

Founded by Charles R. Steele and Marie-Louise Steele

Cover photo: Mando Gomez, www.mandolux.com

See msp.org/jomms for submission guidelines.

JoMMS (ISSN 1559-3959) at Mathematical Sciences Publishers, 798 Evans Hall #6840, c/o University of California, Berkeley, CA 94720-3840, is published in 10 issues a year. The subscription price for 2019 is US $635/year for the electronic version, and $795/year (+$60, if shipping outside the US) for print and electronic. Subscriptions, requests for back issues, and changes of address should be sent to MSP.

JoMMS peer-review and production is managed by EditFLOW® from Mathematical Sciences Publishers.

PUBLISHED BY

mathematical sciences publishers

nonprofit scientific publishing

http://msp.org/

JOURNAL OF MECHANICS OF MATERIALS AND STRUCTURES
Vol. 14, No. 2, 2019
dx.doi.org/10.2140/jomms.2019.14.193

A MODE-DEPENDENT ENERGY-BASED DAMAGE MODEL FOR PERIDYNAMICS AND ITS IMPLEMENTATION

CHRISTIAN WILLBERG, LASSE WIEDEMANN AND MARTIN RÄDEL

The mathematical modeling of failure mechanisms in solid materials and structures is a long standing problem. In recent years, peridynamics has been used as a theoretical basis for numerical studies of fracture initiation, evolution and propagation. In order to investigate damage phenomena numerically, suitable material and damage models have to be implemented in an efficient numerical framework. This framework should be highly parallelizable in order to cope with the computational effort due to the high spatial and, depending on the problem, temporal resolution required for high accuracy. The open-source peridynamic framework Peridigm offers a computational platform upon which new developments of the peridynamic theory can be implemented. Today, isotropic material models and a very simple damage model are implemented in Peridigm.

This paper proposes three energy-based damage criteria. The implementation approach as well as the extension of Peridigm with these physically motivated models is described. The original criterion of Foster et al. is adapted for ordinary state based material. The other two criteria utilize the decomposition of peridynamic states in isotropic and deviatoric parts to account for the failure-mode dependency.

The original criterion is verified by the numerical simulation of two mechanical problems. At first, a virtual double cantilever beam (DCB) experiment is performed to determine the energy release rate. This value is the fundamental material property required for the proposed criteria. Additionally, the DCB problem is then used to investigate the convergence of the numerical scheme implemented in Peridigm. In a second step, a model of a plate with a cylindrical hole under tensile loading is compared with an extended finite element method solution. Results of both numerical solutions are in good agreement. Finally, a fiber reinforced micro structure model is used to analyze the effect of the different criteria to the damage initiation and crack propagation under a more complex loading condition.

A list of symbols can be found on page 215.

1. Introduction

Today, the full exploitation of the lightweight potential of fiber reinforced plastics (FRPs) is limited due to the lack of reliability of failure predictions of real structures. Compared to isotropic materials, the failure mechanisms in FRPs are very complex, as shown in Figure 1 on the next page. The photograph on the left shows the crack pattern in a uniaxial test of an FRP specimen including fiber ondulations as typical manufacturing deviations. The crack is curved and multiple delaminations occur if the specimen fails. The photo on the right illustrates a FRP microstructure under tensile loading perpendicular to the fiber direction. In such specimens cracking starts at multiple locations where the stress concentration is greatest [Gamstedt and Sjögren 1999]. If the load is increased further, local cracks begin to merge, resulting in the complete failure of the specimen [Krause 2016a].

Keywords: peridynamics, damage model, open source.

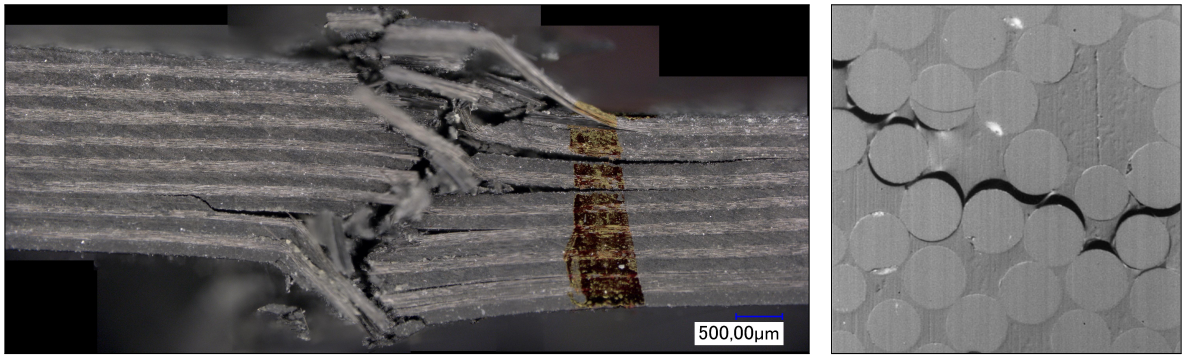

Figure 1. Exemplary failure mechanisms in FRP materials: crack in a CFRP specimen (left, courtesy DLR) and matrix failure (right) [Gamstedt and Sjögren 1999; Krause 2016a].

Accurate modeling of such damage and fracture phenomena, including static and dynamic crack propagation, is an active and open challenge among researchers. The main difficulty inherent in such problems arise from the fact that crack nucleation and propagation in materials cannot be accurately predicted by the majority of currently available computational techniques based on classical continuum theory of mechanics [Boyce et al. 2014].

The current state-of-the-art methods used in industry and research for failure prediction are based on classical continuum mechanics (CM) and its numerical implementation using the finite element method (FEM). Classical CM is well suited to stress analyses of undamaged structures. With proper restrictions, the resulting PDEs are elliptic in equilibrium problems. Due to assumptions made in classical CM (see Section 2), this theory is unable to properly model damage evolution after initiation [Silling 2017; Silling 2000]. To overcome this, additional theories, such as fracture mechanics, are required. However, most of these techniques still suffer from unsatisfactory accuracy and low efficiency when dealing with specific problems, such as three-dimensional crack propagation in bodies under complex loading conditions [Mossaiby et al. 2017].

Motivated by ideas of molecular dynamics, Stewart Silling developed peridynamic theory as an alternative theory to classical CM, starting with [Silling 2000]. Also known as peridynamics (PD), this theory provides a promising approach for simulating damage initiation, evolution and interaction in any material. It is a nonlocal theory taking long-range forces between material points in a certain neighborhood into account. In this theory the divergence term of the governing PDE is replaced by an integral term. Constitutive models in peridynamics depend on relative deformation vectors as opposed to classical constitutive models, which depend on deformation gradients [Seleson et al. 2016]. In addition, spatial derivatives in the governing equations of classical CM are replaced by integral terms in peridynamics. These integral terms can be evaluated at any point whether or not a discontinuity in the displacement function, e.g. caused by a crack, exists. The original bond-based peridynamics (BB-PD) formulation was introduced in [Silling 2000] and is based on the interaction forces between two material points. Therein, linear isotropic materials are limited to a Poisson ratio of 0.25 for 3D and 2D plane strain problems and 0.33 for 2D plane stress problems [Silling et al. 2007]. To overcome these limitations, Silling et al. [2007] introduced a state-based peridynamics (SB-PD) formulation. It is based on the collective interaction forces between a given material point and material points in a finite neighborhood of this point, called

the point's *family* and here denoted by $\mathcal{H}$. In this paper, it is assumed that these forces act along the direction vectors between the material points near the natural state. This is called the ordinary state-based (OSB) approach and considers bond forces depending on deformations of all neighboring material points. State-based PD is able to describe materials with arbitrary Poisson's ratios [Silling et al. 2007].

Silling et al. [2009] compared classical CM and PD for the conservation of linear momentum. The classical CM uses a differential equation, whereas PD uses an integral formulation:

$$\rho(\boldsymbol{x})\,\ddot{\boldsymbol{u}}(\boldsymbol{x},t) = \operatorname{div}\boldsymbol{\sigma} + \boldsymbol{b}(\boldsymbol{x},t), \tag{1-1}$$

where t, $\boldsymbol{b}$, ρ, $\boldsymbol{\sigma}$ and $\ddot{\boldsymbol{u}}$ are the time, external forces, mass density, Cauchy stresses and acceleration for the position $\boldsymbol{x}$. If a problem described by classic CM has a discontinuity, the model assumptions for this region are no longer valid. Classical CM loses its validity, as $\operatorname{div}\boldsymbol{\sigma}$ is no longer defined. Therefore, classical CM is no longer able to provide physically meaningful solutions. This vadility problem does not exist in PD. The integral formulation ensures the conservation of linear momentum at any point, even at discontinuities. No model adjustments or extensions need to be made. If the medium of the integration domain is continuous and the deformation is twice continuously differentiable for $\lim_{\mathcal{H}\to 0}$, the PD solution converges to the classical CM solution [Silling and Lehoucq 2008].

To model damage initiation and propagation in PD theory, failure criteria are required, ideally referring to physically measurable values. These criteria are needed to assess whether individual bonds, the interactions of points within $\mathcal{H}$, have exceeded their load-bearing capacity. The most common criterion used in PD compares the *stretch* (relative change in distance) between two discrete points with a reference value, the critical stretch [Madenci and Oterkus 2014]. If the stretch between the two discrete points exceeds a certain value, the bond is irreversibly deleted. The damage starts and there is no load transfer via the broken bond. The critical stretch model works well for brittle materials and has been validated for several problems [Silling and Askari 2005; Ghajari et al. 2014]. However, the critical stretch is not a physically measurable material property. It is recalculated using assumptions from PD theory and includes a discretization dependency [Madenci and Oterkus 2014]. Although bonds can break under shear deformation, this criterion only considers the volumetric part of the deformation, being insensitive to the deviatoric part. Hence it is unsuitable for simulating the fractures observed in elasto-visco-plastic materials [Dipasquale et al. 2017].

Foster et al. [2009; 2011] described an energy-based failure criterion. They used a J-integral calculation at the crack tip to determine a critical bond energy density from the experimentally measurable energy release rate. The critical energy density of each bond is compared with this critical value. If the value is exceeded, the bond breaks. In the case of crack propagation, the sum of the local bond energy densities, related to the crack surface, leads back to the global value of the energy release rate.

Three energy-based criteria considering mixed mode conditions and an implementation strategy are presented here. The implementation is verified and a convergence study is performed. The implemented failure criteria are used to analyze damage propagation in a micro structure model of a FRPs structure. The code and models are published in [Rädel and Willberg 2018] for further use.

2. Theoretical background

Ordinary state-based peridynamics (OSB-PD) is used to overcome the restrictions of BB-PD. Foster et al.

[2011] noted that within state-based PD the word bond is used loosely. It only describes the relationship between two material points and can be abstractly thought of as an interaction potential. There is not necessarily a notion of direct connectivity, such as a spring-like force. To illustrate the later derivation for the energy criterion consistently and comprehensibly, the derivation of the linear elastic material law for OSB-PD is illustrated. The notation follows [Silling et al. 2007].

In contrast to spring-like forces, the magnitude of the force density vector states may not be equal for the OSB-PD formulation; that is, in general $|\underline{\boldsymbol{T}}[\boldsymbol{x}, t]\langle \boldsymbol{x}' - \boldsymbol{x}\rangle| \neq |\underline{\boldsymbol{T}}[\boldsymbol{x}', t]\langle \boldsymbol{x} - \boldsymbol{x}'\rangle|$. See Figure 2 for the linear case with infinitesimal deformations. The equation of motion of OSB-PD is

$$\rho(\boldsymbol{x})\ddot{\boldsymbol{u}}(\boldsymbol{x}, t) = \int_{\mathcal{H}} \left(\underline{\boldsymbol{T}}[\boldsymbol{x}, t]\langle \boldsymbol{x}' - \boldsymbol{x}\rangle - \underline{\boldsymbol{T}}[\boldsymbol{x}', t]\langle \boldsymbol{x} - \boldsymbol{x}'\rangle\right) \mathrm{d}V + \boldsymbol{b}(\boldsymbol{x}, t), \tag{2-1}$$

where $\mathcal{H}$ is a spherical neighborhood of radius δ, called the horizon, centered at $\boldsymbol{x}$. All points $\boldsymbol{x}'$ within the horizon of $\boldsymbol{x}$ are called the family of $\boldsymbol{x}$. The force density vector state $\underline{\boldsymbol{T}}$ maps the bond $\langle \boldsymbol{x}' - \boldsymbol{x}\rangle$ to force per unit volume squared in the deformed configuration [Silling et al. 2007]. $\underline{\boldsymbol{T}}$ has to be consistent with basic physical principles as the balance of linear momentum. To describe a material, constitutive models are needed. These models map specific deformation vector states $\underline{\boldsymbol{Y}}$ into the force density vector state $\underline{\boldsymbol{T}}$.

Following [Silling et al. 2007], to determine the force density per volume square for a PD material, it is assumed that there exists a strain energy density function W such that

$$\underline{\boldsymbol{T}} = \nabla W(\underline{\boldsymbol{Y}}), \tag{2-2}$$

where ∇ is the Fréchet derivative.

It is further assumed that the elastic strain energy in a PD solid is equal to the energy of the CM model. In that case, it is supposed that there is a PD strain energy density function $W : V \to \mathbb{R}$ such that, for some choice of the deformation gradient $\boldsymbol{F}$,

$$\underline{\boldsymbol{Y}}(\boldsymbol{\xi}) = \boldsymbol{F}\boldsymbol{\xi} = \boldsymbol{F}\langle \boldsymbol{x}' - \boldsymbol{x}\rangle \quad \text{for all } \boldsymbol{\xi} \in \mathcal{H}. \tag{2-3}$$

Then the PD corresponds to the classical constitutive model. This means that the classical CM and PD models are identical for homogeneous deformations of a homogeneous body with deformation gradient $\boldsymbol{F}$ [Silling et al. 2007; Aguiar and Fosdick 2014].

For the isotropic case and considering infinitesimal deformations the undeformed scalar state is defined as $\underline{x} = |\underline{\boldsymbol{X}}\langle \boldsymbol{\xi}\rangle|$ and the deformation scalar state is defined as $\underline{y} = |\underline{\boldsymbol{Y}}\langle \boldsymbol{\xi}\rangle|$. Then, the extension scalar state $\underline{e}$

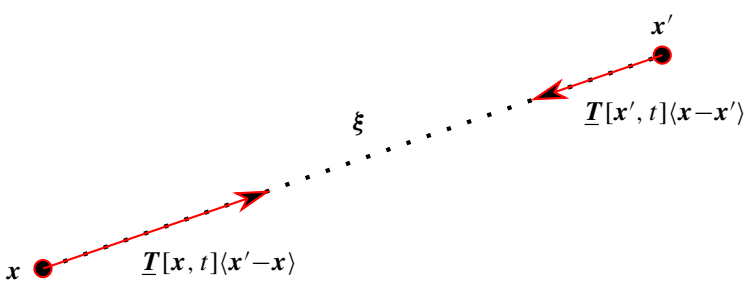

Figure 2. Illustration of OSB forces for the linear case with infinitesimal deformations.

for a PD linear solid can be defined as

$$\underline{e} = \underline{y} - \underline{x} = |\boldsymbol{\eta}|. \tag{2-4}$$

It must be noted that for a general material $\underline{y} - \underline{x} \neq |\boldsymbol{\eta}|$. To obtain the force density scalar state $\underline{t} = |\underline{\boldsymbol{T}}|$ of a single bond for an isotropic elastic PD solid, the extension scalar state is decomposed into its isotropic and deviatoric parts [Silling et al. 2007]. The decomposition of states utilizes a orthogonal deformation basis and therefore the deviatoric and isotropic deformations can be considered independently as

$$\underline{e}^d\langle\boldsymbol{\xi}\rangle = \epsilon^d_{ij}\xi_i\frac{\xi_j}{|\boldsymbol{\xi}|} \qquad \text{and} \qquad \underline{e}^i\langle\boldsymbol{\xi}\rangle = \epsilon_{ii}\xi_i\frac{\xi_i}{|\boldsymbol{\xi}|}. \tag{2-5}$$

By comparing classical the CM strain energy with the PD one, material parameters based on the classical CM model are obtained. Specifically, one creates a strain energy function W_{PD} using (2-5) and compares it with W_{CM}:

$$\begin{aligned} W_{\mathrm{CM}} &= \tfrac{1}{2}K\left[\epsilon_{kk}\right]^2\delta_{ij} + 2G\left[\epsilon^d_{ij}\right]^2 \stackrel{!}{=} W_{\mathrm{PD}}, \\ W_{\mathrm{PD}} &= \frac{A}{2}\int_{\mathcal{H}}\underline{\omega}\langle\boldsymbol{\xi}\rangle\left[\epsilon^d_{ij}\xi_i\frac{\xi_j}{|\boldsymbol{\xi}|}\right]^2 \mathrm{d}V_{\boldsymbol{\xi}} + \frac{B}{2}\int_{\mathcal{H}}\underline{\omega}\langle\boldsymbol{\xi}\rangle\left[\epsilon_{ii}\xi_i\frac{\xi_i}{|\boldsymbol{\xi}|}\right]^2 \mathrm{d}V_{\boldsymbol{\xi}}. \end{aligned} \tag{2-6}$$

Because of the state decomposition, the unknowns A and B can be obtained solving the integrals and setting one deformation state to zero in each case. This results in

$$A = \frac{3K}{m_V} \quad \text{and} \quad B = \frac{15G}{m_V}, \tag{2-7}$$

Here K and G are the bulk and shear moduli of the classical theory of linear elasticity. Introducing A and B into (2-6) we obtain the PD strain energy density as

$$W = \frac{3K}{2m_V}\int_{\mathcal{H}}\underline{\omega}\langle\boldsymbol{\xi}\rangle\left[\underline{e}^i\langle\boldsymbol{\xi}\rangle\right]^2\mathrm{d}V_{\boldsymbol{\xi}} + \frac{15G}{2m_V}\int_{\mathcal{H}}\underline{\omega}\langle\boldsymbol{\xi}\rangle\left[\underline{e}^d\langle\boldsymbol{\xi}\rangle\right]^2\mathrm{d}V_{\boldsymbol{\xi}}, \tag{2-8}$$

with the weighted volume m_V and the nonlocal dilatation θ given by

$$m_V = \int_{\mathcal{H}}\underline{\omega}\langle\boldsymbol{\xi}\rangle\underline{x}\,\underline{x}\,\mathrm{d}V_{\boldsymbol{\xi}} \quad \text{and} \quad \theta = \frac{3}{m_V}\int_{\mathcal{H}}\underline{\omega}\langle\boldsymbol{\xi}\rangle\underline{x}\,\underline{e}\langle\boldsymbol{\xi}\rangle\,\mathrm{d}V_{\boldsymbol{\xi}}. \tag{2-9}$$

Using (2-2), one can derive the contribution of a single bond and its force density scalar state $\underline{t}$:

$$\underline{t}\langle\boldsymbol{\xi}, t\rangle = \frac{\underline{\omega}\langle\boldsymbol{\xi}\rangle}{m_V}\left[3K\theta\underline{x} + 15G\underline{e}^d\right]. \tag{2-10}$$

To obtain $\underline{\boldsymbol{T}}$, the force density scalar state has to be transformed from bond coordinates to global Cartesian coordinates. For small deformations and isotropic material the transformation can be done as

$$\underline{\boldsymbol{T}} = \underline{t}\frac{\underline{\boldsymbol{Y}}}{|\underline{\boldsymbol{Y}}|}. \tag{2-11}$$

The complete derivation is given in [Silling et al. 2007].

3. Damage model

Foster et al. [2009; 2011] described an energy-based failure criterion which is valid for state-based analysis. The criterion converts the globally measurable energy release rate into a local critical bond energy density. For a given horizon δ, the critical micro potential w_C can be determined using the energy release rate G_0:

$$w_C = \frac{4G_0}{\pi\delta^4}. \tag{3-1}$$

If the bond micro potential is greater than this value, the bond is removed and an initial failure occurs. With the history-dependent scalar-valued function $\chi(\boldsymbol{\xi}, t)$ defined by

$$\chi(\underline{e}\langle\boldsymbol{\xi}\rangle, t) = \begin{cases} 1 & \text{if } w(\underline{e}\langle\boldsymbol{\xi}\rangle) < w_C, \\ 0 & \text{otherwise,} \end{cases} \tag{3-2}$$

the damage model can be included in (2-10) as

$$\underline{t} = \chi(\underline{e}\langle\boldsymbol{\xi}\rangle, t)\left(\frac{3K\theta}{m_V}\underline{\omega x} + \frac{15G}{m_V}\underline{\omega e}^d\right). \tag{3-3}$$

In an OSB formulation the bond energy can be determined as

$$w = \int_{\boldsymbol{\eta}} \left(\underline{\boldsymbol{T}}[\boldsymbol{x}, t]\langle\boldsymbol{x}' - \boldsymbol{x}\rangle - \underline{\boldsymbol{T}}[\boldsymbol{x}', t]\langle\boldsymbol{x} - \boldsymbol{x}'\rangle\right) \mathrm{d}\boldsymbol{\eta} \tag{3-4}$$

where

$$\boldsymbol{\eta} = \boldsymbol{u}[\boldsymbol{x}', t] - \boldsymbol{u}[\boldsymbol{x}, t] \tag{3-5}$$

is the bond displacement vector state. We recall from Figure 2 that $\underline{\boldsymbol{T}}[\boldsymbol{x}, t]\langle\boldsymbol{x}' - \boldsymbol{x}\rangle$ and $\underline{\boldsymbol{T}}[\boldsymbol{x}', t]\langle\boldsymbol{x} - \boldsymbol{x}'\rangle$ are bond force density vector states. As Figure 2 shows for an OSB model, the force density scalar states $\underline{t}$ depend on the direction $\langle\boldsymbol{x} - \boldsymbol{x}'\rangle$ and $\langle\boldsymbol{x}' - \boldsymbol{x}\rangle$. For an OSB formulation, the force density scalar state for the respective material point $\underline{t}\,[\boldsymbol{x}, t]$ and $\underline{t}\,[\boldsymbol{x}', t]$ has to be calculated. The distinction between contraction and extension is made by calculating the relative extension scalar state

$$\underline{e}_{\mathrm{rel}}\langle\boldsymbol{\xi}\rangle = \frac{\underline{e}\langle\boldsymbol{\xi}\rangle}{\underline{x}}. \tag{3-6}$$

Thus, the bond is contracted if $\underline{e}_{\mathrm{rel}}\langle\boldsymbol{\xi}\rangle < 0$ and extended if $\underline{e}_{\mathrm{rel}}\langle\boldsymbol{\xi}\rangle > 0$. Different bond micro potentials could be applied, if needed. Because the decomposition of states is already done, additional bond energy criteria could be defined evaluating the isotropic compression w_{cmp}, the isotropic tension w_{ten} and the shear part w_{shr}. The assumption behind this distinction is based on the crack modes of classical fracture mechanics [Anderson 2005]. A mode I fracture is dominated by the tensile stress within the material and therefore only the isotropic part of the model has to be compared to the G_{IC} energy. The same applies to the shear part w_{shr} of the model. This can be compared against the energy release rate G_{IC} from the shear-dominated mode II fracture type. The bond micro potential for compression and tension can be determined as

$$w_{\mathrm{cmp}} = w_{\mathrm{ten}} = \tfrac{1}{4}\chi(\underline{e}\langle\boldsymbol{\xi}\rangle, t)\left(\frac{K[\boldsymbol{x}]}{m_V[\boldsymbol{x}]}\theta^2[\boldsymbol{x}, t] + \frac{K[\boldsymbol{x}']}{m_V[\boldsymbol{x}']}\theta^2[\boldsymbol{x}', t]\right)\underline{x}^2, \tag{3-7}$$

Name	Criterion
Energy criterion	$w_{\text{bond}} > w_C$
Power law	$w^2_{\text{cmp}} + w^2_{\text{ten}} + w^2_{\text{shr}} > w^2_{C,\text{cmp}} + w^2_{C,\text{ten}} + w^2_{C,\text{shr}}$
Separated	$(w_{\text{cmp}} > w_{C,\text{cmp}}) \wedge (w_{\text{ten}} > w_{C,\text{ten}}) \wedge (w_{\text{shr}} > w_{C,\text{shr}})$

Table 1. Three types of energy-based damage criteria.

where the distinction between compression and tension can be made using (3-6), namely $\underline{e}_{\text{rel}}\langle\boldsymbol{\xi}\rangle < 0$ for contraction and $\underline{e}_{\text{rel}}\langle\boldsymbol{\xi}\rangle > 0$ for extension. The bond micro potential for the shear part is given as

$$w_{\text{shr}} = \tfrac{1}{4}\chi(\underline{e}\langle\boldsymbol{\xi}\rangle, t)\big(B[\boldsymbol{x}]\big(\underline{e}\langle\boldsymbol{\xi}\rangle - \tfrac{1}{3}\theta[\boldsymbol{x}, t]\underline{x}\big)^2 + B[\boldsymbol{x}']\big(\tfrac{1}{3}\theta[\boldsymbol{x}']\underline{x} - \underline{e}\langle\boldsymbol{\xi}\rangle\big)^2\big), \tag{3-8}$$

where B is given in (2-7).

To evaluate the bond damage condition one of three criteria from Table 1 can be chosen.

The factor $\frac{1}{4}$ results from the integration and the averaging of the bond force density state $\underline{t}$. This averaging is necessary, as the scalar force density is dependent on the direction [Silling 2017]. The energy criterion, with

$$w_{\text{bond}} = \tfrac{1}{4}\chi\left(\underline{e}\langle\boldsymbol{\xi}\rangle, t\right)\left(\underline{t}\left[\boldsymbol{x}, t\right] - \underline{t}\left[\boldsymbol{x}', t\right]\right)\underline{e}\langle\boldsymbol{\xi}\rangle \tag{3-9}$$

corresponds to the criterion from [Foster et al. 2011]. The power law criterion takes mixed mode fracture into account [Song 2006]. The separated energy criteria check the isotropic compression and tension energies as well as the shear energy separately. If critical values regarding the tension or shear energy are exceeded the bond breaks.

4. Implementation

Peridigm [Parks et al. 2012] is used in the context of the present study. It is an open-source state-based PD code developed at Sandia National Laboratories for massively parallel multi-physics simulations. Peridigm uses a FE mesh as basis for its discretization. Hexahedron and tetrahedron elements are transformed into PD collocation points and associated with the respective element volume. The entire data structure is divided into PD collocation points and their neighbours within the horizon. In theory each point and its interaction with his neighbours could be calculated at a single computer core. Points with the same properties, material and damage model, are bundled into blocks.

Algorithm 1 show the program structure for explicit Verlet time integration, implemented in Peridigm. After initialization, a loop is started on the number of time increments n_{timeStep}. New displacements and forces at the collocation points are determined for each time step in the loop. These are then synchronized between the definition blocks and computer cores. This is required, because the time integration of the neighboring collocation points do not necessarily have to be performed on the same core as the collocation point itself.

After the data has been synchronized, a loop is started over all blocks n_{blocks}. Within this loop, all collocation points n_{nodes} are looped twice. The first run calls the damage model routines and determines whether a bond between a collocation point and a neighbor within the family $n_{\text{neighbors}}$ must be broken. In the second loop, the force densities resulting from the interaction of every collocation point with its

neighborhood are determined. The data is synchronized in a global vector and the Verlet time integration schema is performed.

```
initialization;
for ndt ← 1 to n_timeStep do
    t = t + Δt;
    updateDisplacementsToBlocksAndCores;

    for blockID ← 1 to n_blocks do
        for i ← 1 to n_nodes do
            for j ← 1 to n_neighbors do
                calculateDamages;
        for i ← 1 to n_nodes do
            for j ← 1 to n_neighbors do
                calculateBondForces;
    synchronizeForcesInGlobalVector;
    timeIntegrationInGlobalVector;
```

Algorithm 1. Peridigm data structure.

For the implementation of the energy criterion, information from the collocation point $\boldsymbol{x}$ and $\boldsymbol{x}'$ is required. Therefore, the solution shown in Figure 3 has been implemented in Peridigm.

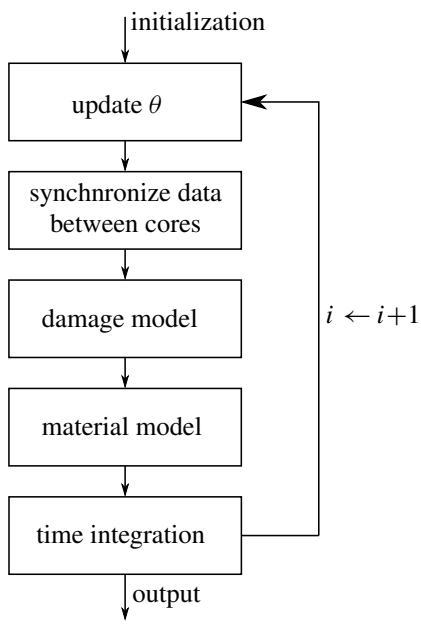

Figure 3. Workflow in Peridigm.

For each step, the dilatation θ is calculated for the actual model deformation state $\boldsymbol{y}_i$. These dilatations are stored in a global vector and synchronized between the computer cores and blocks. In a next step, the force density scalar states in node i and its neighbor j are determined:

$$\begin{aligned} \underline{t}_i &= \chi(\underline{e}\langle\boldsymbol{\xi}\rangle, t)\left(\frac{3K_i\theta_i}{m_{V,i}}\underline{\omega}\underline{x} + \frac{15G_i}{m_{V,i}}\underline{\omega}\underline{e}_i^d\right), \\ \underline{t}_j &= \chi(\underline{e}\langle\boldsymbol{\xi}\rangle, t)\left(\frac{3K_j\theta_j}{m_{V,j}}\underline{\omega}\underline{x} + \frac{15G_j}{m_{V,j}}\underline{\omega}\underline{e}_j^d\right). \end{aligned} \tag{4-1}$$

The bond micro potential then is

$$w = \tfrac{1}{4}\left(\operatorname{abs}(\underline{t}_i) + \operatorname{abs}(\underline{t}_j)\right)\operatorname{abs}(\underline{e}\langle\boldsymbol{\xi}\rangle). \tag{4-2}$$

The absolute values of the force density scalar states as well as $\underline{e}\langle\boldsymbol{\xi}\rangle$ are used in the numerical implementation to avoid problems with coordinate changes between the node and neighbor node reference.

The volumetric part of the discrete bond micro potential for tension and compression can be calculated as

$$w_{\text{ten}} = w_{\text{cmp}} = \tfrac{1}{4}\chi(\underline{e}\langle\boldsymbol{\xi}\rangle, t)\left(\frac{K_i}{m_{V,i}}\theta_i^2 + \frac{K_j}{m_{V,j}}\theta_j^2\right)\underline{x}^2 \tag{4-3}$$

and the deviatoric part as

$$w_{\text{shr}} = \tfrac{1}{4}\chi(\underline{e}\langle\boldsymbol{\xi}\rangle, t)\left(\alpha_i\left(\underline{e}\langle\boldsymbol{\xi}\rangle - \tfrac{1}{3}\theta_i\underline{x}\right)^2 + \alpha_j\left(\tfrac{1}{3}\theta_j\underline{x} - \underline{e}\langle\boldsymbol{\xi}\rangle\right)^2\right), \tag{4-4}$$

with

$$\alpha_i = \frac{15G_i}{m_{V,i}} \quad \text{and} \quad \alpha_j = \frac{15G_j}{m_{V,j}}. \tag{4-5}$$

The damage laws have been implemented in Peridigm as an open-source routine, found at [Rädel and Willberg 2018].

5. Verification

Three problems have been analyzed and evaluated for the validation of the proposed criteria and their implementation. The first problem is a virtual experiment used to determine the energy release rate. In this so-called DCB experiment, a specimen with rectangular cross section, with an initial crack is loaded by pulling the upper and lower half. This triggers a controlled crack propagation from the initial crack initiation tip. The energy release rate can be determined by analyzing the force-displacement curves in relation to the crack length. The result of this evaluation must correspond to the input parameter in order to verify the assumptions made in [Foster et al. 2011]. Additionally, a convergence study is conducted. The horizon δ and the point distance dx of a structured mesh are varied.

The example of a fracturing plate with a circular cutout under tensile loading is considered as a second problem. This model has an analytical solution in the context of classical linear elasticity [Lekhnitskii 1968] which yields to the position of the damage initiation. The PD solution is compared against an XFEM (extended FEM) analysis performed in the commercial finite element code Abaqus.

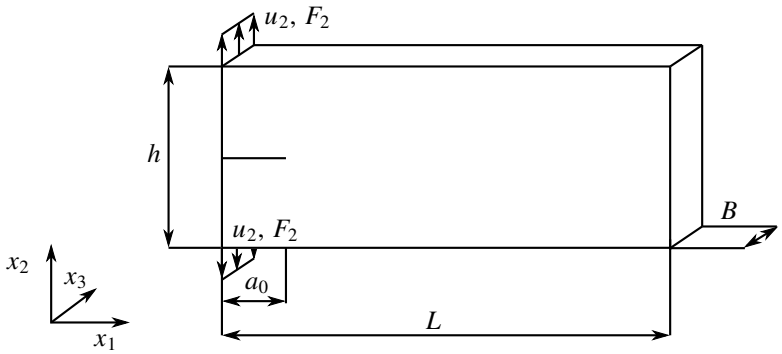

Figure 4. Setup of the DCB simulation with $a_0 = 0.005\,\text{m}$, $L = 0.05\,\text{m}$, $B = 0.006\,\text{m}$ and $h = 0.02\,\text{m}$. The displacement function was chosen to be $u_2^+(t) = 0.004\,\text{m/s} \cdot t$ above the precrack and $u_2^-(t) = -0.004\,\text{m/s} \cdot t$ underneath it.

5A. ***Double cantilever beam.*** The geometry and dimensions of the DCB model are given in Figure 4. The original finite elements are represented in Peridigm as points with corresponding volume. The numerical PD model has a structured discretization resulting in equally spaced PD collocation points. The distance between all points is $dx = 0.001\,\text{m}$ for all three spatial directions.

A pre-crack of length a_0 is defined in the x_2-center of the model at the left specimen boundary. Bonds in the domain of the crack are omitted. Nonlocal displacement boundary conditions are applied to the left edges along x_3 to induce a crack opening. The displacement conditions are applied uniformly on more than one x_1 row of collocation points, $u_2^+(t) = 0.004\,\text{m/s} \cdot t$ above and $u_2^-(t) = -0.004\,\text{m/s} \cdot t$ underneath the pre-crack. As a result, the upper part of the DCB model bends upwards and the lower part bends downwards. This results in a load concentration at the crack tip, which leads to a high bond micro potential. For an ideal homogeneous isotropic material, crack growth in x_1-direction occurs when the external load is further increased. The Python scripts for creating the model as well as the Peridigm input decks are given in [Rädel and Willberg 2018].

To solve the problem, a transient analysis is performed. This requires time integration. For all the analyzes presented here, the explicit Verlet time integration scheme is used. The material parameters are shown in Table 2. An energy release rate of $G_{IC} = 12\,\text{N/m}$ is chosen. This value is not representative of any standard material and was chosen low to reduce the computing time. The energy release rate determines the time of crack initiation and the degradation path after crack initiation.

In case the criteria are properly implemented, it must be possible to reproduce them in the virtual experiment, independent of the value itself.

To determine the energy release rate G_{IC}, the force-displacement $(F_2(t), u_2(t))$ curve are recorded and evaluated. The force function $F_2(t)$ is the summed resulting force of all nodes the displacement function $u_2(t)$ is applied on. The whole procedure is exemplarily explained for the horizon $\delta = 0.003\,\text{m}$, shown in Figure 5. Prior to initial damage, the force-displacement curve starts with a linear response.

$\rho = 2000\,\text{kg/m}^3$	$K = 1.75 \cdot 10^9\,\text{Pa}$	$G = 8.08 \cdot 10^8\,\text{Pa}$	$G_{IC} = 12\,\text{N/m}$

Table 2. Material data chosen for the verification.

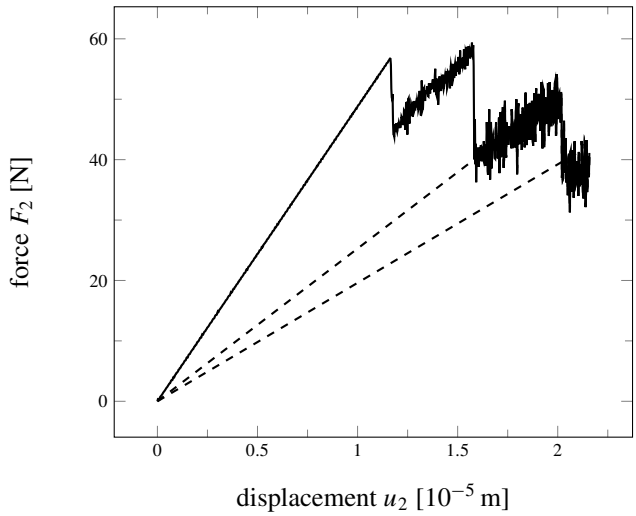

Figure 5. Force-displacement curve.

This is the pre-damage part of the simulation. After damage initiation the resulting force decreases, while the crack propagates. To determine the resulting energy release rate G_{IC}, the dissipated energy W_{diss} due to crack propagation within the material, is required.

Assuming no further energy dissipation occurs, the energy release rate can be determined by calculating the area between the force-displacement curve and a linear function. The linear function intersects the coordinate origin and the force-displacement curve of the model at an arbitrary time increment n_{cut}, shown as an example for one force-displacement curve and two linear functions in Figure 5. It corresponds to an idealized relief path within the virtual DCB experiment. The area between the two curves represents the dissipated energy.

To integrate the area between the curves the Riemann sum

$$W_{\text{diss}} = \Delta u \sum_{i=1}^{n_{\text{cut}}} (F_i - F_{i,\text{linear function}}) \tag{5-1}$$

is determined. The energy release rate can be determined by dividing the dissipated energy W_{diss} by the crack surface $A_{\text{crack}} = Bl_{\text{crack}}$ as

$$G_{IC} = \frac{W_{\text{diss}}}{Bl_{\text{crack}}}, \tag{5-2}$$

where l_{crack} is the crack length and B is the width of the model [Monteiro et al. 2015]. To determine the energy release rate G_{IC} for the increment n_{cut} the corresponded crack length l_{crack} is measured. For this purpose the damage index color map plots I_{damage} for increment n_{cut} is used, shown in Figure 6 for a point distance in all three spatial directions of $dx = 0.001$ m. The damage index is determined as

$$I_{\text{damage}} = n_{\text{broken}} / n_{\text{neighbors}}, \tag{5-3}$$

where n_{broken} is the number of broken bonds of a point and $n_{\text{neighbors}}$ is the initial number of all of its bonds.

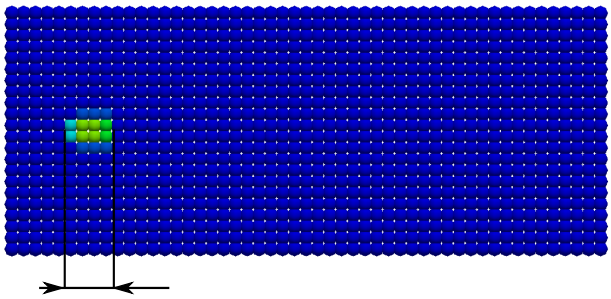

Figure 6. Crack length at $t = 2.21$ ms.

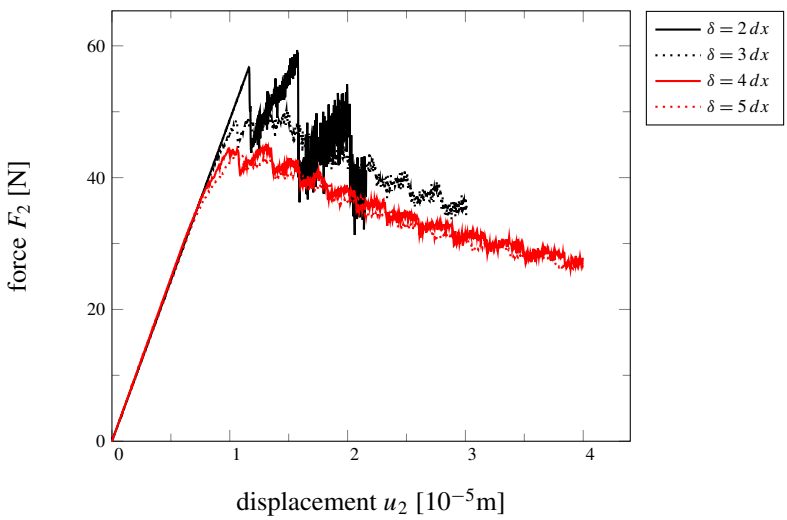

Figure 7. Force-displacement curves for $dx = 0.001$ m.

To show the independence of the horizon, four models with different horizons are calculated. To determine the energy release rate of the four models, two arbitrary linear functions are used for the respective curve similar to Figure 5. The time, the corresponding crack length and the resulting G_{IC} are given in Table 3. The force-displacement curves without the linear function for the DCB models with different horizons are shown in Figure 7.

Although the curves differ significantly from each other, the calculated energy release rates are well in line with the reference value of $G_{IC} = 12\,\mathrm{N/m}$ defined in the Table 2. The differences in the results have three main reasons

- The crack length is rounded to 0.001 m, which is the minimal distance between two nodes.
- The position of the crack tip is estimated using the damage index plot. This means that points that are not yet completely separated from each other would have a virtual crack length that cannot be clearly determined. The error is in the range ± 0.0005 m. For a higher resolution this error becomes smaller.

	linear function 1			linear function 2		
horizon δ [mm]	t [ms]	l_{crack} [m]	G_{IC} [N/m]	t [ms]	l_{crack} [m]	G_{IC} [N/m]
2.015	4.21	0.003	12.8	5.26	0.005	11.4
3.015	5.88	0.005	13.1	7.35	0.007	12.9
4.015	5.01	0.004	11.1	9.99	0.011	11.3
5.015	6.36	0.006	11.2	9.99	0.010	11.9

Table 3. Results of the verification.

dx [mm]	$\delta =$	$2\,dx$ [mm]	$3\,dx$ [mm]	$4\,dx$ [mm]	$5\,dx$ [mm]
0.5		1.0	1.5	2.0	2.5
0.3		0.66	0.99	1.32	1.65
0.25		0.5	0.75	1.0	1.25
0.125		0.25	0.375	0.5	0.625

Table 4. Combinations for convergence analysis.

- Due to the explicit time integration scheme without damping there is noise, which slightly influences the curve integration.

In conclusion, the results are accurate enough to demonstrate the functionality of the implemented failure models. The next step is to demonstrate the convergence of the model.

5B. ***Double cantilever beam: convergence.*** After the correct implementation is checked, the convergence behavior is analyzed. As described in Section 2, the PD solution for homogeneous material converges against the classic CM solution in case no damage is considered. Therefore, a model with linear elastic material behavior is created and solved with the FEM. The solution is used as a reference curve for the time before damage initiation. The geometry and material parameters are identical to the model data of the PD model.

The uniform point distance dx in all three model dimensions of a structured mesh as well as the corresponding horizon δ is given in Table 4. Four different scenarios are considered: $dx = 0.5$ mm, $dx = 0.33$ mm, and $dx = 0.25$ mm and $dx = 0.125$ mm. The model setup and material parameters are otherwise the same as in section 5A.

Only the results of two cases are presented here, as the others are very similar. The resulting curves described in Table 4 are shown in Figures 8 and 9. All discretizations dx reflect the undamaged behavior until crack initiation compared to the FEM result. The time of crack initiation and the necessary forces differ considerably. All curves show that the highest force is required at a horizon of $2\,dx$. The noise in the crack propagation area is also very high.

For the curves with a horizon of $3\,dx$, the forces are also higher compared to the curves where the horizons are larger than $3\,dx$. For horizons larger than $3\,dx$, the crack initiation time and the force are

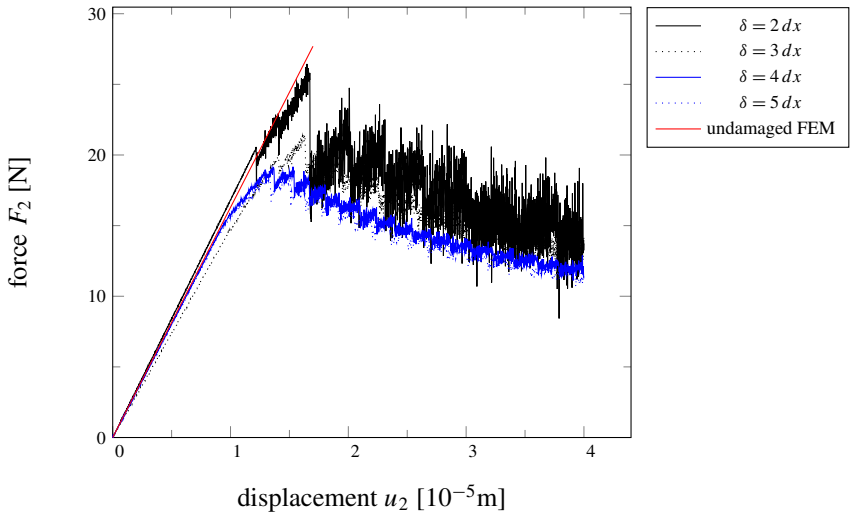

Figure 8. Force-displacement curves for discretization $dx = 0.5$ mm.

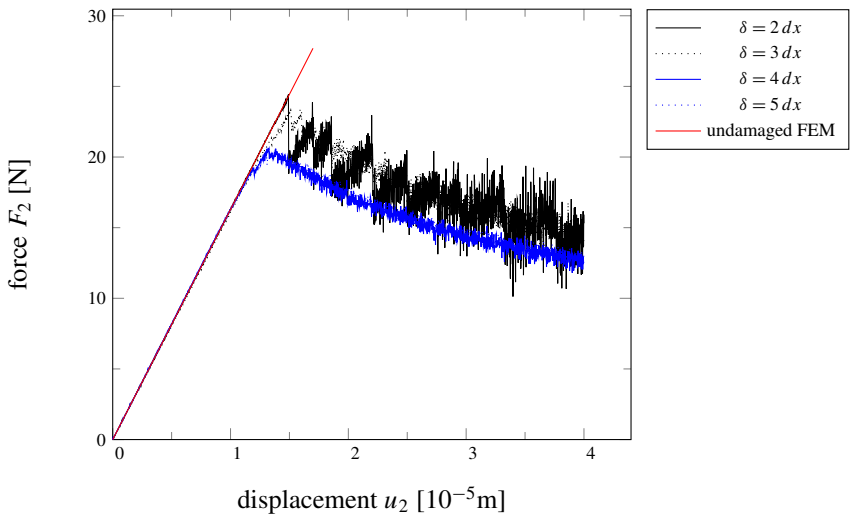

Figure 9. Force-displacement curves for discretization $dx = 0.125$ mm .

approximately equal for the respective discretization dx. The behaviour in the crack propagation area is also identical.

To analyze the discretizations, the curves $4\,dx$ and $5\,dx$ of the discretization $dx = 0.33$ mm, 0.25 mm and 0.125 mm are plotted in Figure 10.

The results of the three discretizations show the same behavior in the linear pre-crack part of the simulation. After crack initiation the resulting forces for both horizons $4\,dx$ and $5\,dx$ of $dx = 0.33$ mm are 10–15% higher compared to the models with the discretization of $dx = 0.25$ mm and $dx = 0.125$ mm. These curves are almost identical. They show the same, converged, damage initiation load of 20.5 N and the degredation path is similar.

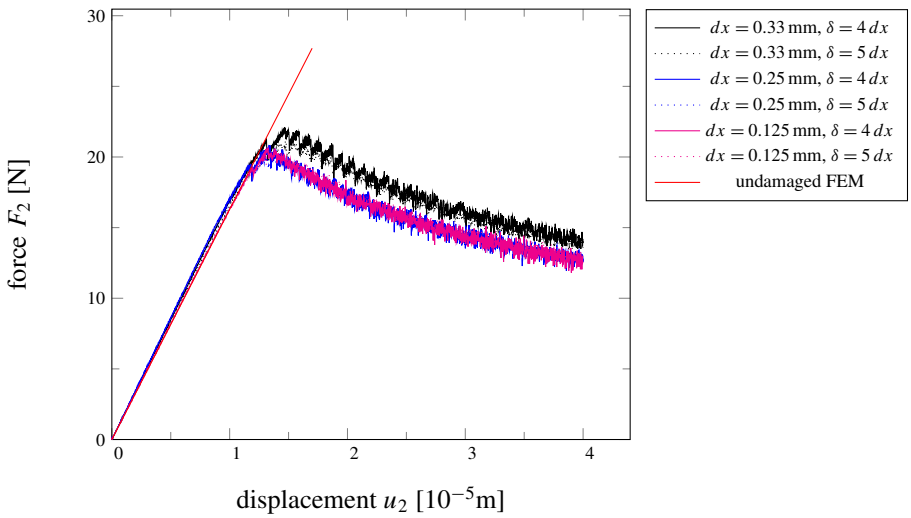

Figure 10. Force-displacement curves for horizons $4\,dx$ and $5\,dx$ for various discretizations dx.

In general, for horizons $\delta > 3\,dx$ the curves after crack initiation are smoother. The reason is, that for smaller horizons one bond caries more load, which leads to more noise if the bond breaks. This effect is smaller for larger horizons.

5C. ***Plate with hole.*** After the convergence of the PD energy criterion has been demonstrated a plate with a circular hole under tensile loading is analyzed.

The classical CM has analytical solutions for the stress distribution around the hole [Lekhnitskii 1968], which have been validated in experiments. This allows to predict the location of damage initiation. The crack is assumed to emerge from points on the boundary of the cutout perpendicular to the loading direction. This is due to the fact, that the maximum stress concentration under tensile loading occurs at these points in CM. Furthermore, the crack is predicted to propagate horizontally, transverse to the loading direction.

Additionally, the results are compared with a XFEM fracture model consisting of an initiation criterion and a propagation model. The standard FEM does not allow crack propagation through elements. It is only capable to represent crack growth by numerically expensive adaptive remeshing techniques around the crack front or the element deletion method, where energy is artificially dissipated from the model. An enhancement of the FEM is the XFEM which offers a possibility to simulate crack growth through the element domain by application of the "partition of unity" approach [Melenk and Babuška 1996; Belytschko et al. 2009]. The commercial FE code Abaqus offers an implementation of the XFEM.

For both the PD and XFEM analysis, a three-dimensional rectangular plate made of homogeneous, isotropic and linear elastic material with a circular cutout in its center is considered. The geometry of the plate is shown in Figure 11. The plate has a length and width of $L = M = 0.05$ m. The thickness of the plate is $h = 0.5$ mm. The hole diameter is $D = 0.01$ m.

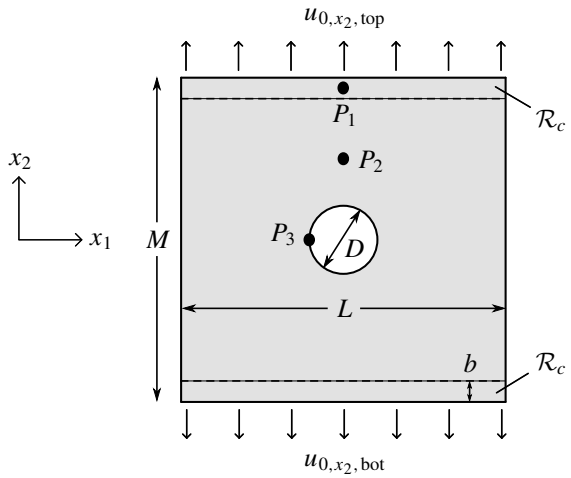

Figure 11. Model definition for a plate with a circular hole in its center; $L = M = 50\,\text{mm}$, $h = 0.5\,\text{mm}$ and $D = 10\,\text{mm}$.

The material properties are given in Table 5. The model is calculated using the energy criterion proposed in [Foster et al. 2011]. The boundary conditions $\dot{u}_{y,\text{top}}$ and $\dot{u}_{y,\text{bot}}$, the horizon δ and the average distance between mesh points dx are given in Table 6.

Peridigm is sensitive to the horizon size. The spacing between material points should be chosen uniformly in one block in order to reduce the effect of discretization errors. Thus, the underlying mesh has to consist of approximately uniformly spaced elements. The requirement of generating constant mesh elements of length $dx = 0.5\,\text{mm}$ is given to the mesh generator. This results in a constant horizon size of $\delta = 3.015 \cdot dx = 1.5075\,\text{mm}$.

To trigger damage, the plate is subjected to a constant uniaxial velocity along the horizontal edges in opposite direction, as illustrated in Figure 11.

The boundary conditions are applied to two constrained regions $\mathcal{R}_c$. They are defined along the bottom and top horizontal edges of the plate, as illustrated in Figure 11. Both regions have a depth of $b = 3 \cdot dx$. The imposed displacements are given by the prescribed velocities $\dot{u}_{x_2,\text{top}}$ for the top part and $\dot{u}_{x_2,\text{bot}}$ for the bottom part, each multiplied by the current calculation time. This results in a uniformly increasing displacement over time. Thus, the prescribed displacement applied on each PD material point in the top constrained region is given by $u_{0,x_2,\text{top}} = \dot{u}_{x_2,\text{top}} \cdot t$ and in the bottom constrained region is given by $u_{0,x_2,\text{bot}} = \dot{u}_{x-2,\text{bot}} \cdot t$. The prescribed velocities, the horizon δ and the time t_{end} are given in Table 6.

$\rho = 8000\,\text{kg/m}^3$	$E = 192\,\text{MPa}$	$\nu = 0.33$	$G_{IC} = 287\,072\,\text{N/m}$	$s_C = 0.02$

Table 5. Material data chosen for a plate with hole.

$\dot{u}_{y,\text{top}} = -\dot{u}_{y,\text{bot}} = 0.275\,41\,\text{m/s}$	$\delta = 1.515\,\text{mm}$	$t_{\text{end}} = 0.001\text{s}$	$dx = 0.5\,\text{mm}$

Table 6. Model parameters.

The XFEM analysis has been performed on a two-dimensional model utilizing the commercial code Abaqus. The thickness is considered irrelevant for the present plane-stress problem. For the application of the XFEM an extra damage initiation criterion is needed.

This assumption is necessary to change the underlying model within the FEM. Until damage occurs, the modeling of the FEM and XFEM is based on the approximate solution of the weak formulation of classical CM. After the crack has been initiated, the underlying assumptions lose their validity locally. Therefore, a fracture mechanical model describing the crack propagation within the XFEM elements is used. The maximum principal strain criterion is used as the initiation criterion. The strain value has been calculated using the energy release rate G_{0C} as provided by Madenci [2014] for 3D models:

$$\varepsilon_C = s_C = \sqrt{\frac{G_{0C}}{\left[3G + \left(\frac{3}{4}\right)^4 \left(K - \frac{5}{3}G\right)\right]\delta}}. \tag{5-4}$$

The assumption is only acceptable as long as no shear strain occurs in the known area of crack initiation. At the position of crack initiation the strain ε_{22} is approximately equal to the critical stretch. However, this assumption is not generalizable. A consistent derivation of the critical stretch from the energy release rate is not possible for OSB-PD [Willberg and Rädel 2018]. If the principal strain given by (5-4) exceeds the value, the crack starts and a bilinear traction separation law as illustrated in [Trilaksono et al. 2013] is used. The XFEM uses a quasi-static analysis. To avoid singularities in the stiffness matrix a viscous damping is introduced.

For the XFEM model, damage initiation occurs at time $t = 0.672\,\text{ms}$ for a total displacement of $u_y = 0.370\,\text{mm}$. The crack initiation and propagation is shown in a damage index plot in Figure 12.

The first damage is visible in the second pane of the figure, when the critical stretch value has been reached. In order to reach complete failure of an element, the critical separation has to reach the value Δ_{fail}, which is indicated by red elements in the damage plot. Note that the damage variable used in the damage plots for XFEM has a different definition compared to the damage plots for the PD solution. In Figure 12, blue color indicates undamaged elements, equivalent to entirely undamaged bonds of a material point in Peridigm. Red elements in an Abaqus damage plot indicate that an element has failed and a crack runs through it. In that case the element has a local damage value of 1. The damage index in Peridigm, given in (5-3), describes the ratio of broken to initially unbroken bonds within the family of a collocation point. If a crack occurs between two points, they are still connected with their neighboring nodes at their corresponded sites of the crack. For the definition of a complete fracture plane, comparable to the DCB model, a local damage value of approximately 0.41 is sufficient. The PD collocation point then is completely disconnected from his neighbors at the other site of the crack surface.

It can be seen in Figure 12 that the crack growth on both sides of the hole is not proceeding uniformly. This might be due to non-uniformity in the mesh. Thus, the crack growth behaves slightly different on both sides of the plate. The effect is especially noticeable for the propagation of the crack on the right side of the cutout from time $t = 0.7731\,\text{ms}$ (step 1273) to $t = 0.8264\,\text{ms}$ (step 1800). During this period, the crack on the right is not propagating further while the crack on the left side has already reached the left boundary of the plate. For the XFEM the unsymmetric mesh leads to a stagnation of the crack at one side and finally to an unsymmetric solution. In theory, this should not be the case for a perfectly homogeneous structural model without numerical inaccuracies in the FEM and the symmetric

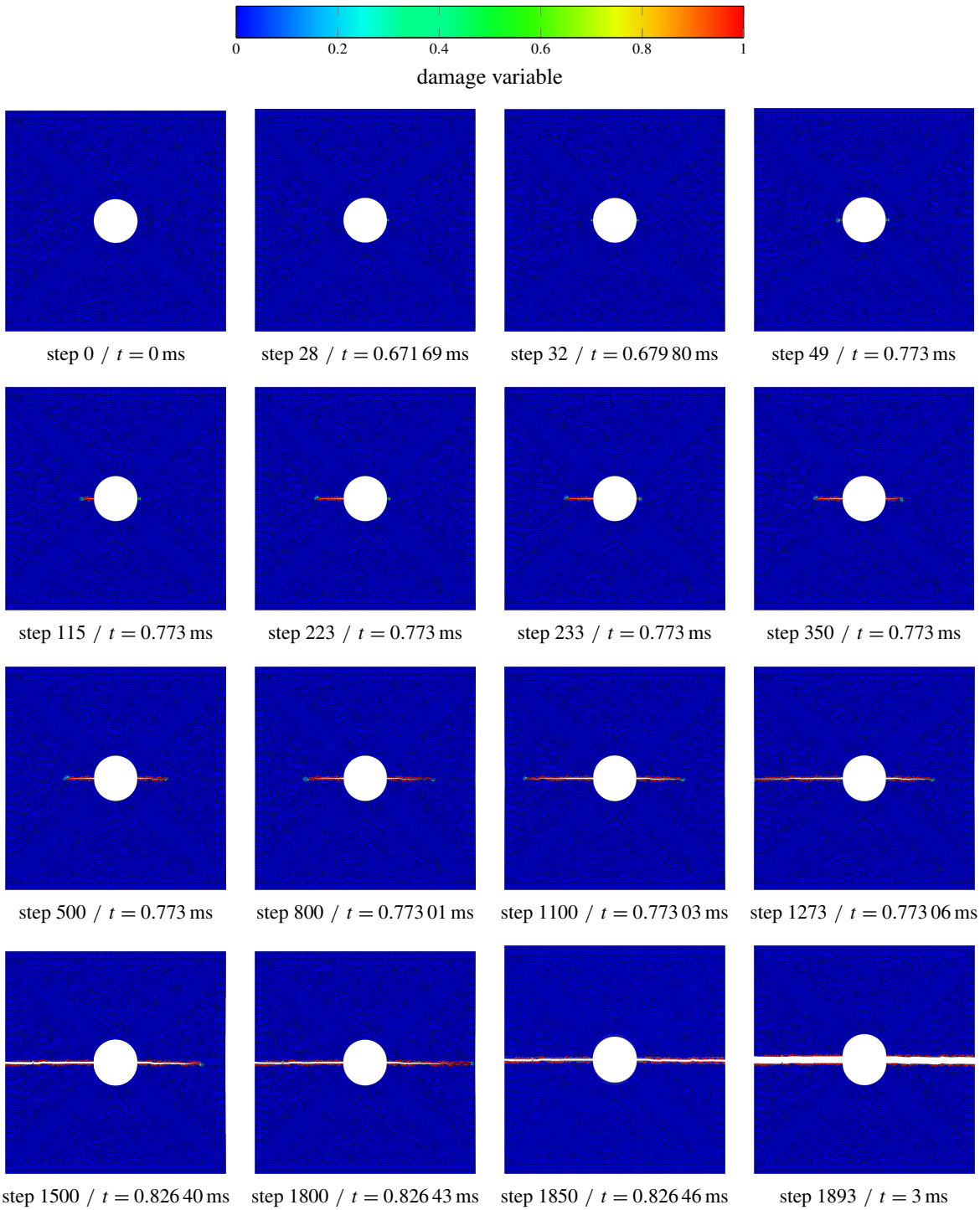

Figure 12. Damage plot of plate with circular cutout under tensile loading for different time steps computed with XFEM.

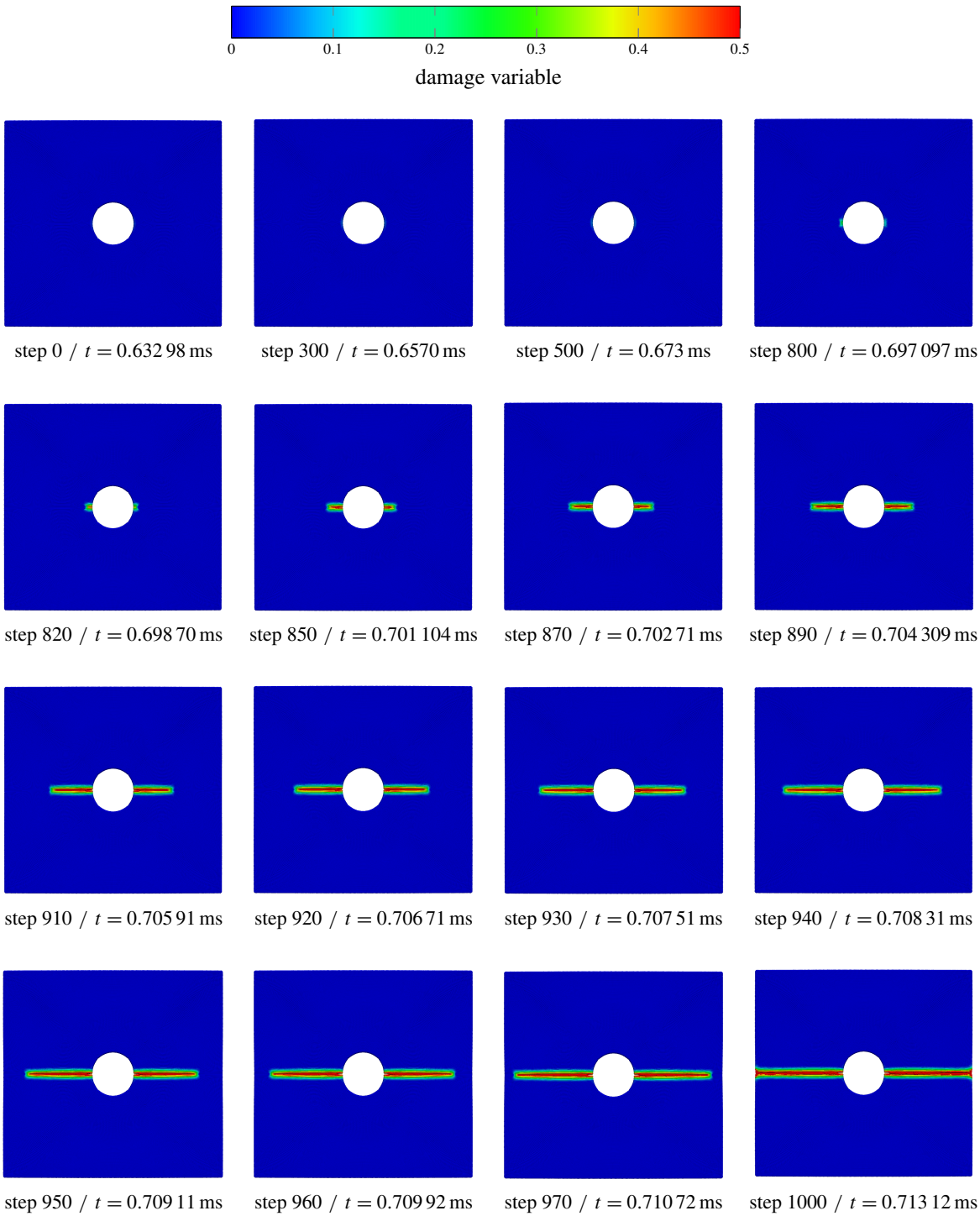

Figure 13. Damage plot of plate with circular cutout under tensile loading for different time steps computed with Peridigm.

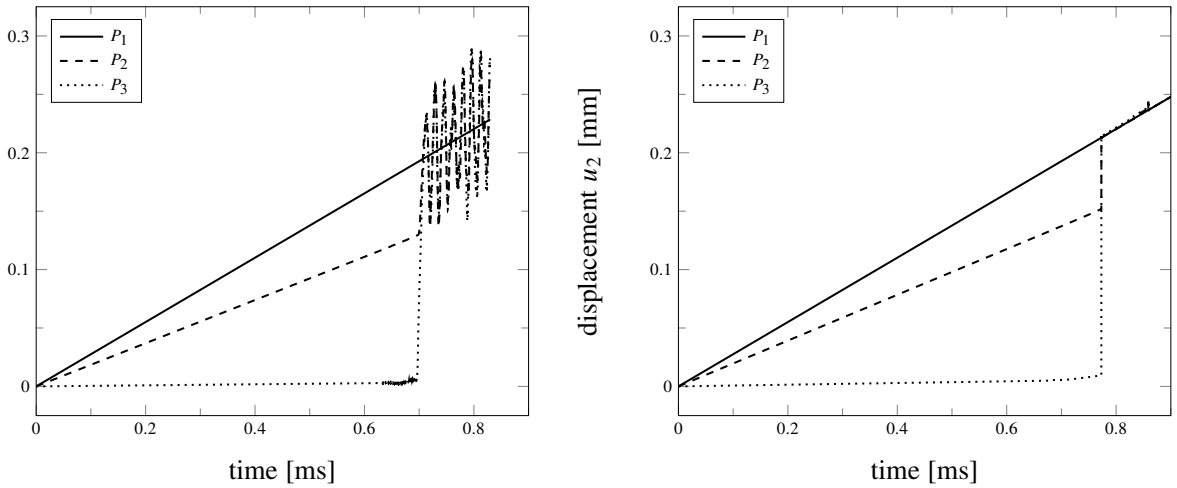

Figure 14. Comparison of displacement curves at given points P_1, P_2 and P_3 (see Figure 11) for the Peridigm model (left) the XFEM model with viscous damping of 0.0001 (right).

load application as well as the chosen boundary conditions. In contrast to the XFEM, the impact of the discretization to the result is lower for the PD result. This is because PD is implemented as a meshless method in Peridigm, which is independent of the composition of the mesh. Therefore, this can be seen as an advantage of PD compared to XFEM.

In the Abaqus computation total failure occurs at time $t = 0.872\,\text{ms}$ with a total displacement in x_2-direction of $u_{x_2,ult} = 0.456\,\text{mm}$.

The results obtained with Peridigm are shown in Figure 13 (see previous page). Damage initiation starts earlier compared to the XFEM solution. The crack propagates almost symmetrically in both directions. This is not caused by the underlying PD theory. Numerical implementation of PD problems similar to XFEM solution can occur.

Figure 14 shows the displacement curves at three points defined in Figure 11. Before damage initiation, the gradient of the three curves are equal. The PD result shows an earlier failure initiation compared to the XFEM analysis. The behaviour of the curves differ after crack initiation. This is caused by the use of different solving methods. Solving the XFEM model a quasi-static analysis is performed. The viscous damping in the XFEM solution decreases the noise in the displacement curves after the damage initiation occurs. The PD result uses an explicit time integration schema without damping. Thus the displacement solution shows oscillations.

In summary, it can be said that the energy criterion is able to reproduce the expected crack initiation propagation. The following possibilities have been identified as reasons for the different initiation times:

- Initiation criterion of XFEM differs from PD one.
- Dependency of the mesh in XFEM, which finally lead to an unsymmetrical crack.
- Step width and quasi-static solver of the XFEM analysis.

6. Composite modeling

To study the effect of the different energy-based failure criteria, a scaled representative volume element (RVE) of height $h_{\text{RVE}} = 0.025\,\text{m}$ consisting of a FRP material has been analyzed. This model is based on the work of Krause [Krause 2016a; Krause 2016b] and the fiber locations are randomly distributed. The model has been created utilizing a finite element preprocessor. The finite element input file, with the geometry and boundary conditions from Figure 15, has been automatically transformed into a input, readable by Peridigm.

The total model height is $h = h_{\text{RVE}} + 2h_b$. The height $h_b = 0.00167\,\text{m}$ is defined to ensure that the load introduced by the displacement function is equally distributed. The displacement function itself is applied at the top and bottom surface nodes of the RVE. Bonds within the boundary region cannot be damaged and the region is very stiff compared to the rest of the model.

Parameters for discretization were determined in [Rädel et al. 2017a; 2017b] and used within the model to obtain accurate results. The horizon is given by $\delta = 4\,dx = 0.002\,\text{m}$ based on the analysis in Section 5B and with $dx = 5 \cdot 10^{-4}\,\text{m}$ as the average distance between two points, because of computational limitations. The material properties of the fiber and the matrix made of resin are illustrated in Table 7 and the values for the different energy criteria are given in Table 8.

Figure 16 illustrates how the damage typically progresses in experiments under transverse tension. The cracks grow around single fibers, bridge the matrix-dominant area between fibers and finally interact with

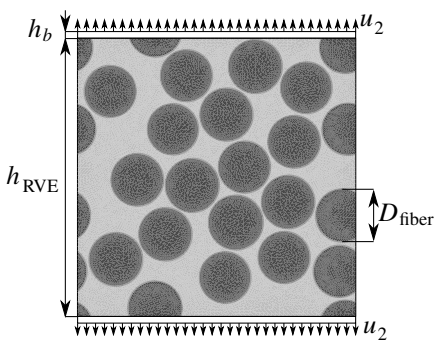

Figure 15. Setup of the RVE simulation: $D_{\text{fiber}} = 6.744\,\text{mm}$, $h_{\text{RVE}} = 25\,\text{mm}$ and $h_b = 1.67\,\text{mm}$. The displacement function is $u_2 = 0.213\,\text{m/s} \cdot t$.

Fiber	$\rho = 1800\,\text{kg/m}^3$	$K = 17.283\,\text{GPa}$	$G = 11.382\,\text{GPa}$
Resin	$\rho = 1300\,\text{kg/m}^3$	$K = 3.125\,\text{GPa}$	$G = 1.119\,\text{GPa}$

Table 7. Material data chosen for the verification.

$w_{\text{iso}} = 0.4 \cdot 10^{-3}\,\text{N/m}$	$w_{\text{cmp}} = 0.4 \cdot 10^{-3}\,\text{N/m}$	$w_{\text{ten}} = 0.38 \cdot 10^{-3}\,\text{N/m}$

Table 8. Critical energies chosen for the resin in the RVE model. Values are the same for the energy criterion (only w_{iso} applies), the power law criterion and the separated energy criterion.

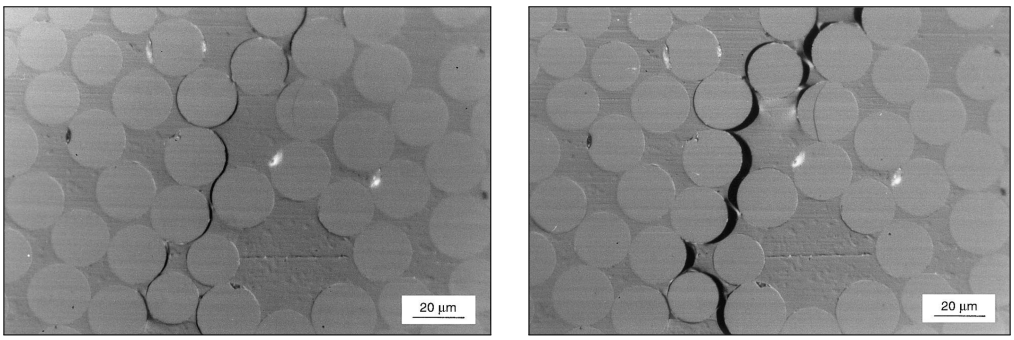

Figure 16. Phases of damage under transverse tension [Gamstedt and Sjögren 1999]: debond (left) and transverse crack (right).

each other. Experimental and numerical results show that debonding occurs around many fibers but only one dominant transverse crack is finally created [Krause 2016a].

Figure 17 shows the results obtained by using the three energy-based failure criteria, introduced in Table 1. Starting with the damage initiation, four different time steps are shown. It can be seen that

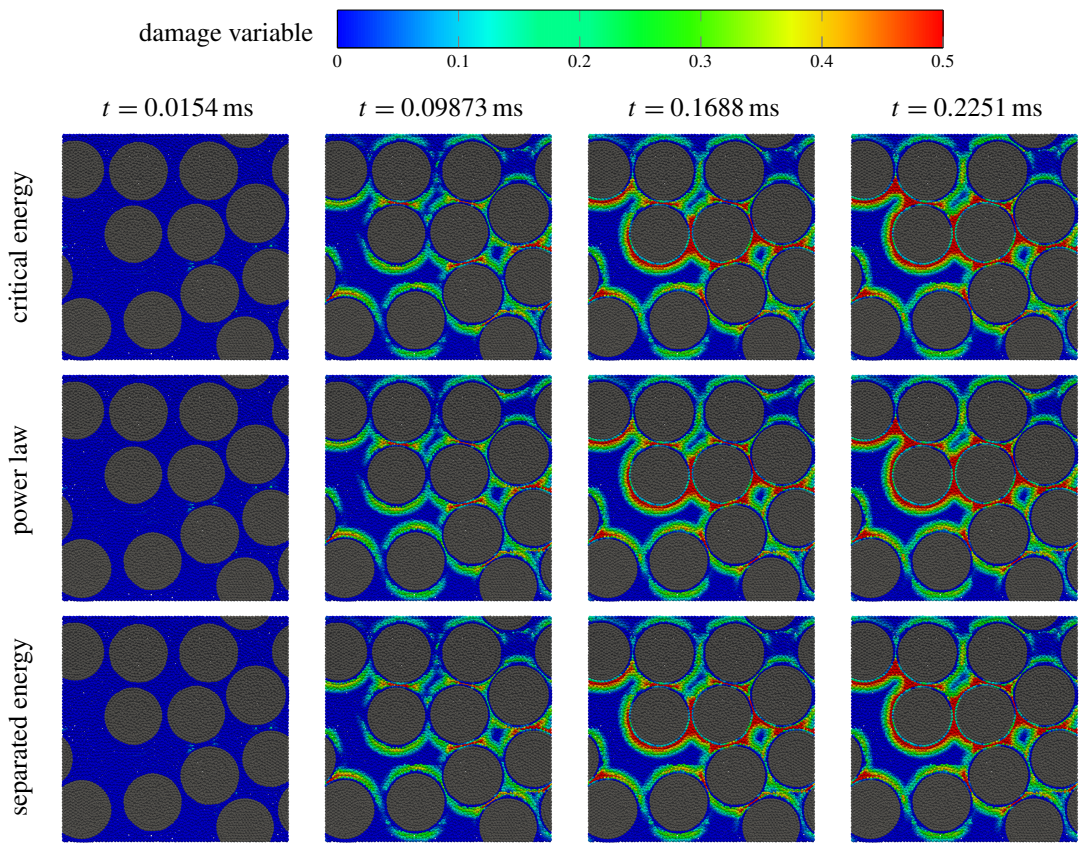

Figure 17. Damage plot of RVE utilizing the different energy criteria.

the damage initiation as well as the ongoing damage process is almost equal between all criteria. The damage initiates at the fiber-matrix interface. The cracks grow and interact with each other. In the event of a further load increase, the various individual cracks combine to form an overall crack. The tensile part of the energy is dominant compared to the shear part. Thus the damage patterns of all models are similar. The crack patterns of the simulation results are in good agreement with the measurement results shown in Figure 1, right.

7. Conclusion

The implementation and verification of three energy-based failure criteria have been presented. These criteria only require physically measurable material properties. The criteria have been implemented in the open-source code Peridigm. It is parallelizable and consequently usable for large scale problems. The verification examples indicate that the implemented criteria work as expected. It has been shown that global energy release rate could be represented by local micro energy bond potentials.

The model converges for a resolution $dx = 0.25\,\text{mm}$ with a horizon greater than $3\,dx$. Regardless of the discretization, horizons smaller than $4\,dx$ overestimate the crack initiation load and high noise in the damage progress area.

The results of a complex micro structure model of a FRP illustrates that all implemented criteria are able to describe micro structural damage and the results do not differ substantially from literature results. The example illustrates that the general failure mechanism is captured by all three presented models. Therefore, the criterion of [Foster et al. 2011] is to be preferred. On the contrary to the two other criteria, only one material parameter, the energy release rate, has to be determined. In real applications, the experimental measurement of this parameter is already standardized and therefore easier to determine than for the other two criteria.

The final routine as well as the models are published within [Rädel and Willberg 2018].

List of symbols (continues on next page)

m_V	weighted volume	V	volume
s	stretch	W	strain energy density
s_C	critical stretch	χ	scalar damage function
t	time	δ	horizon
u	displacement	ε	strain
w	bond energy micro potential	ϵ	strain tensor component
E	Young's modulus	ν	Poisson ratio
G	shear modulus	ρ	density
G_0	energy release rate	θ	dilatation
G_{0C}	critical energy release rate	ξ	component of the undeformed vector state
G_{IC}	critical energy release rate mode I	$\boldsymbol{\eta}$	bond vector, deformed
G_{IIC}	critical energy release rate mode II	$\boldsymbol{\xi}$	bond vector, undeformed
$\mathcal{H}$	family	$\boldsymbol{x}$	external body force density
K	bulk modulus	$\boldsymbol{\sigma}$	Cauchy stress
$\mathbb{R}$	Euclidean space	$\boldsymbol{u}$	deformation vector

List of symbols (continued)

$\ddot{\boldsymbol{u}}$	acceleration vector	$\underline{t}$	force density scalar state
$\boldsymbol{x}$	position vector, undeformed	$\underline{x}$	position scalar state, undeformed
$\boldsymbol{y}$	position vector, deformed	$\underline{y}$	position scalar state, deformed
$\boldsymbol{F}$	deformation gradient	$\underline{\boldsymbol{T}}$	force vector state
$\underline{\omega}$	influence scalar state	$\underline{\boldsymbol{X}}$	reference vector state
$\underline{e}$	extension scalar state	$\underline{\boldsymbol{Y}}$	deformation vector state

References

[Aguiar and Fosdick 2014] A. R. Aguiar and R. Fosdick, "A constitutive model for a linearly elastic peridynamic body", *Math. Mech. Solids* **19**:5 (2014), 502–523.

[Anderson 2005] T. L. Anderson, *Fracture mechanics: fundamentals and applications*, 3rd ed., CRC Press, Boca Raton, FL, 2005.

[Belytschko et al. 2009] T. Belytschko, R. Gracie, and G. Ventura, "A review of extended/generalized finite element methods for material modelling", *Model. Simul. Mater. Sci. Eng.* **17**:4 (2009), 043001.

[Boyce et al. 2014] B. L. Boyce, S. L. B. Kramer, H. E. Fang, T. E. Cordova, M. K. Neilsen, K. Dion, A. K. Kaczmarowski, E. Karasz, L. Xue, A. J. Gross, A. Ghahremaninezhad, K. Ravi-Chandar, S.-P. Lin, S.-W. Chi, J. S. Chen, E. Yreux, M. Rüter, D. Qian, Z. Zhou, S. Bhamare, D. T. O'Connor, S. Tang, K. I. Elkhodary, J. Zhao, J. D. Hochhalter, A. R. Cerrone, A. R. Ingraffea, P. A. Wawrzynek, B. J. Carter, J. M. Emery, M. G. Veilleux, P. Yang, Y. Gan, X. Zhang, Z. Chen, E. Madenci, B. Kilic, T. Zhang, E. Fang, P. Liu, J. Lua, K. Nahshon, M. Miraglia, J. Cruce, R. DeFrese, E. T. Moyer, S. Brinckmann, L. Quinkert, K. Pack, M. Luo, and T. Wierzbicki, "The Sandia fracture challenge: blind round robin predictions of ductile material tearing", *Int. J. Fract.* **186**:1 (2014), 5–68.

[Dipasquale et al. 2017] D. Dipasquale, G. Sarego, M. Zaccariotto, and U. Galvanetto, "A discussion on failure criteria for ordinary state-based Peridynamics", *Eng. Fract. Mech.* **186** (2017), 378–398.

[Foster et al. 2009] J. T. Foster, S. A. Silling, and W. W. Chen, "State based peridynamic modeling of dynamic fracture", pp. 1–6 in *Proceedings of the SEM Annual Conference* (Albuquerque, NM), 2009.

[Foster et al. 2011] J. T. Foster, S. A. Silling, and W. Chen, "An energy based failure criterion for use with peridynamic states", *Int. J. Multiscale Comput. Eng.* **9**:6 (2011), 675–688.

[Gamstedt and Sjögren 1999] E. Gamstedt and B. Sjögren, "Micromechanisms in tension-compression fatigue of composite laminates containing transverse plies", *Compos. Sci. Technol.* **59**:2 (1999), 167–178.

[Ghajari et al. 2014] M. Ghajari, L. Iannucci, and P. Curtis, "A peridynamic material model for the analysis of dynamic crack propagation in orthotropic media", *Comput. Methods Appl. Mech. Eng.* **276** (2014), 431–452.

[Krause 2016a] D. Krause, *Micromechanics of the fatigue behaviour of polymers*, PhD thesis, Technical University Braunschweig, 2016. DLR Report 2016-26.

[Krause 2016b] D. Krause, "A physically based micromechanical approach to model damage initiation and evolution of fiber reinforced polymers under fatigue loading conditions", *Compos. B Eng.* **87**:Supplement C (2016), 176–195.

[Lekhnitskii 1968] S. G. Lekhnitskii, *Anisotropic plates*, Gordon and Breach, 1968.

[Madenci and Oterkus 2014] E. Madenci and E. Oterkus, *Peridynamic theory and its applications*, vol. 1, Springer, 2014.

[Melenk and Babuška 1996] J. M. Melenk and I. Babuška, "The partition of unity finite element method: basic theory and applications", *Comput. Methods Appl. Mech. Eng.* **139**:1-4 (1996), 289–314.

[Monteiro et al. 2015] J. Monteiro, R. Campilho, E. Marques, and L. da Silva, "Experimental estimation of the mechanical and fracture properties of a new epoxy adhesive", *App. Adhesion Sci.* **3**:1 (2015), 25.

[Mossaiby et al. 2017] F. Mossaiby, A. Shojaei, M. Zaccariotto, and U. Galvanetto, "OpenCL implementation of a high performance 3D peridynamic model on graphics accelerators", *Comput. Math. Appl.* **74**:8 (2017), 1856–1870.

[Parks et al. 2012] M. L. Parks, D. J. Littlewood, J. A. Mitchell, and S. A. Silling, *Peridigm users' guide v1.0.0*, Albuquerque, New Mexico 87185 and Livermore, California 94550, USA, 2012, http://www.sandia.gov/~djlittl/docs/PeridigmV1.0.0.pdf.

[Rädel and Willberg 2018] M. Rädel and C. Willberg, "PeriDoX", GitHub repository, 03 2018.

[Rädel et al. 2017a] M. Rädel, A.-J. Bednarek, J. Schmidt, and C. Willberg, "Influence of propabilistic material distribution in peridyamics to the crack initiation", in *6th ECCOMAS Thematic Conference on the Mechanical Response of Composites*, 2017.

[Rädel et al. 2017b] M. Rädel, C. Willberg, and J. Schmidt, "Effect of discretization and stochastic material distribution on crack initiation in peridynamics", in *14th U.S. National Congress on Computational Mechanics 2017*, 2017.

[Seleson et al. 2016] P. Seleson, Q. Du, and M. L. Parks, "On the consistency between nearest-neighbor peridynamic discretizations and discretized classical elasticity models", *Comput. Methods Appl. Mech. Eng.* **311** (2016), 698–722.

[Silling 2000] S. A. Silling, "Reformulation of elasticity theory for discontinuities and long-range forces", *J. Mech. Phys. Solids* **48**:1 (2000), 175–209.

[Silling 2009] S. A. Silling, "Linearized theory of peridynamic states", Sandia Report SAND2009-2458, Multiscale Science Department, Sandia National Laboratories, 2009, http://www.sandia.gov/~sasilli/SAND2009-2458.pdf.

[Silling 2017] S. A. Silling, "Introduction to peridynamics", pp. 25–60 in *Handbook of peridynamic modeling*, CRC Press, Boca Raton, FL, 2017.

[Silling and Askari 2005] S. A. Silling and E. Askari, "A meshfree method based on the peridynamic model of solid mechanics", *Comput. Struct.* **83**:17-18 (2005), 1526–1535.

[Silling and Lehoucq 2008] S. A. Silling and R. B. Lehoucq, "Convergence of peridynamics to classical elasticity theory", *J. Elasticity* **93**:1 (2008), 13–37.

[Silling et al. 2007] S. A. Silling, M. Epton, O. Weckner, J. Xu, and E. Askari, "Peridynamic states and constitutive modeling", *J. Elasticity* **88**:2 (2007), 151–184.

[Song 2006] S. H. Song, *Fracture of asphalt concrete: a cohesive zone modeling approach considering viscoelastic effects*, Ph.D. thesis, University of Illinois at Urbana-Champaign, 2006.

[Trilaksono et al. 2013] A. Trilaksono, N. Watanabe, H. Hoshi, A. Kondo, Y. Iwahori, and S. Takeda, "Continuous damage monitoring of a thin composite structural with mismatched stiffener in a combined joint using fiber Bragg grating under tension and three-point loading", *Open J. Compos. Mater.* **3**:3 (2013).

[Willberg and Rädel 2018] C. Willberg and M. Rädel, "An energy based peridynamic state-based failure criterion", *Proc. Appl. Math. Mech.* **18**:1 = *Proc. 89th Annual Meeting of the International Association of Apllied Mathematics and Mechanics* (*GAMM*) (2018).

Received 21 Dec 2017. Revised 25 Oct 2018. Accepted 2 Nov 2018.

CHRISTIAN WILLBERG: christian.willberg@dlr.de
German Aerospace Center, Institute of Composite Structures and Adaptive Systems, 38108 Brunswick, Germany

LASSE WIEDEMANN: lasse@wiedemann-sh.de
German Aerospace Center, Institute of Composite Structures and Adaptive Systems, 38108 Brunswick, Germany

MARTIN RÄDEL: martin.raedel@dlr.de
German Aerospace Center, Institute of Composite Structures and Adaptive Systems, 38108 Brunswick, Germany

JOURNAL OF MECHANICS OF MATERIALS AND STRUCTURES
Vol. 14, No. 2, 2019
dx.doi.org/10.2140/jomms.2019.14.219

msp

ELASTIC WAVE PROPAGATION IN A PERIODIC COMPOSITE PLATE STRUCTURE: BAND GAPS INCORPORATING MICROSTRUCTURE, SURFACE ENERGY AND FOUNDATION EFFECTS

GONGYE ZHANG AND XIN-LIN GAO

A new model for predicting band gaps for flexural elastic wave propagation in a periodic composite plate structure is developed using a non-classical Kirchhoff plate model that is based on a modified couple stress theory, a surface elasticity theory and a two-parameter Winkler–Pasternak elastic foundation model. The formulation is based on the plane wave expansion method and Bloch's theorem. The current non-classical model simultaneously incorporates microstructure, surface energy and foundation effects, unlike existing models. When the microstructure and surface energy effects are both suppressed, the new model reduces to the classical elasticity-based model. The band gaps predicted by the newly developed model vary with the microstructure-dependent length scale parameters, the surface elastic constants, the elastic foundation moduli, the unit cell size, and the volume fraction. The numerical results reveal that the first band gap including the foundation effect is always smaller than that without considering the foundation effect, and the first foundation band gap size increases with the increase of the elastic foundation moduli. Also, the first band gap predicted by the new non-classical model is always larger than that predicted by the classical model, but the difference is diminishing as the plate thickness increases. In addition, it is found that the sizes of the first band gap and the first foundation band gap decrease with the increase of the unit cell length at different length scales. Furthermore, it is seen that the volume fraction has a significant effect on the sizes of the first band gap and the first foundation band gap, and band gaps can be tailored by adjusting the volume fraction as well as the constituent properties.

1. Introduction

Band gaps for elastic wave propagation in periodic composite beam and plate structures have received increasing attention (e.g., Sigalas and Economou 1994; Liu and Hussein 2012; Xiao et al. 2012; Piccolroaz and Movchan 2014; Zhang and Parnell 2017; Piccolroaz et al. 2017; Chen et al. 2017; Zhang et al. 2018a). Such periodic composite structures can generate band gaps and are therefore good candidate materials for filtering waves, isolating vibrations and harvesting energy. Bragg scattering and local resonance, two leading causes for band gaps (e.g., Liu and Hussein 2012; Chen and Wang 2014; Madeo et al. 2016), can both be present in such composite structures.

Thin beams and plates often exhibit size effects at the micron and nanometer scales. Microstructure- and/or surface energy-dependent length scale effects have been computationally demonstrated through atomistic simulations for amorphous silica and polymers [Maranganti and Sharma 2007], FCC metals including Ni, Cu and Al [Shodja et al. 2012] and noncoherent metallic bicrystals [Mi et al. 2008]. Recently,

Keywords: band gaps, wave propagation, Kirchhoff plate, couple stress, surface elasticity, elastic foundation, plane wave expansion method, Bloch theorem, size effect.

it has been shown that such nonlocal effects can also be experimentally measured with high accuracy by using the shifts of resonant frequencies of a micron- or nanometer-sized beam [Zhang and Zhao 2016].

Band gap generation is inherently related to material microstructures, and hence band gaps for elastic wave propagation in micro- or nano-structured composite beams and plates are also size-dependent, which cannot be described by applying wave equations based on classical elasticity. As a result, wave equations derived through using non-classical elasticity theories containing material length scale parameters need to be employed in determining band gaps at the micron and nanometer scales.

Several non-classical/high-order elasticity theories have been applied to derive wave equations and study band gaps. Liu et al. [2012] used wave equations based on the surface elasticity theory [Gurtin and Murdoch 1975; 1978] to investigate surface energy effects on band gaps. Li et al. [2016] studied band gaps by employing the wave equations built upon the simplified strain gradient elasticity theory (e.g., Gao and Park 2007). Madeo et al. [2016] applied the wave equations based on a relaxed micromorphic elasticity theory to explore frequency band gaps in metamaterials. Bacigalupo and Gambarotta [2017] utilized a micropolar continuum theory to study band gaps in periodic materials. Band gaps for flexural elastic wave propagation in periodic composite beam structures were recently studied by Zhang et al. [2018a] and Gao et al. [2018] by using non-classical Bernoulli–Euler and Timoshenko beam models based on a modified couple stress theory [Yang et al. 2002; Park and Gao 2008] and a surface elasticity theory [Gurtin and Murdoch 1975; 1978; Steigmann and Ogden 1997; 1999]. However, wave equations for plates built upon such higher-order elasticity theories have not been utilized to determine band gaps in periodic composite plate structures. This motivated the present study.

In the current paper, band gaps for flexural elastic wave propagation in a periodic composite plate structure are studied by using a non-classical Kirchhoff plate model based on the modified couple stress theory [Yang et al. 2002; Park and Gao 2008], the surface elasticity theory [Gurtin and Murdoch 1975; 1978] and a two-parameter Winkler–Pasternak elastic foundation model. In Section 2, the equations of motion for a Kirchhoff plate incorporating the microstructure, surface energy and foundation effects derived by Gao and Zhang [2016] are applied to the current periodic composite plate structure to study wave propagation. The formulation is enabled by using the plane wave expansion method and Bloch's theorem. In Section 3, numerical results for the band gaps predicted by the current non-classical model are presented and compared to those based on the classical elasticity-based model. A summary is provided in Section 4.

2. Formulation

Based on the modified couple stress theory [Yang et al. 2002; Park and Gao 2008], the surface elasticity theory [Gurtin and Murdoch 1975; 1978; Steigmann and Ogden 1997; 1999] and a two-parameter Winkler–Pasternak elastic foundation model (e.g., Yokoyama 1996), the equations of motion for a Kirchhoff plate were derived by Gao and Zhang [2016], which incorporate the microstructure, surface energy and elastic foundation effects. When only the deflection is considered (i.e., $w = w(x, y, t),\ u = 0,\ v = 0$), the equations of motion reduce to

$$-\left[\tfrac{1}{12}(\lambda+2\mu)h^3+\mu l^2 h+\tfrac{1}{2}(\lambda_0+2\mu_0)h^2\right](w_{,xxxx}+2w_{,xxyy}+w_{,yyyy}) + (2\tau_0+k_p)(w_{,xx}+w_{,yy})-k_w w+f_z-c_{x,y}+c_{y,x}=m_0\ddot{w}-m_2\frac{\partial^2\ddot{w}}{\partial x^2}-m_2\frac{\partial^2\ddot{w}}{\partial y^2}, \quad (1a)$$

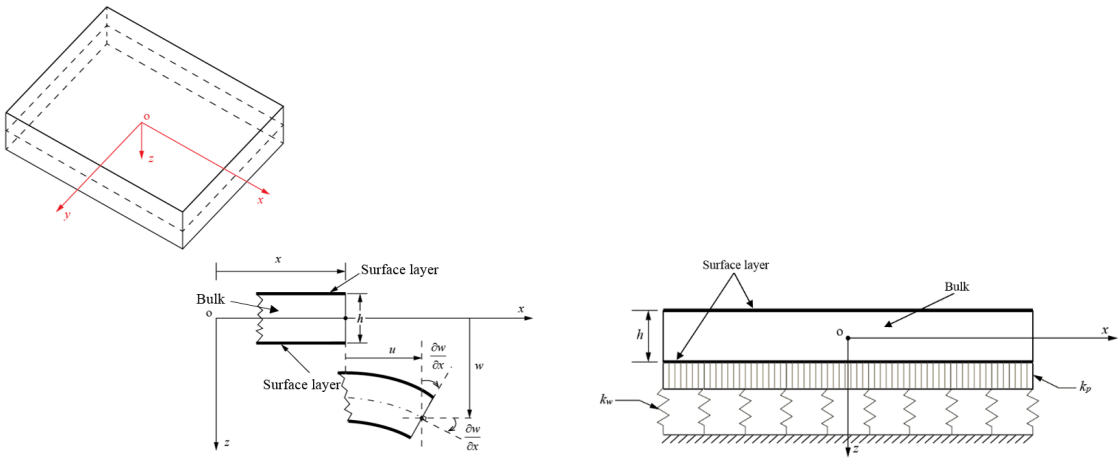

Figure 1. Left: plate configuration and coordinate system. Right: plate on a two-parameter elastic foundation.

which can be rewritten as

$$-\frac{\partial^2}{\partial x^2}\left(D\frac{\partial^2 w}{\partial x^2}+C\frac{\partial^2 w}{\partial y^2}\right)-\frac{\partial^2}{\partial y^2}\left(D\frac{\partial^2 w}{\partial y^2}+C\frac{\partial^2 w}{\partial x^2}\right)-\frac{\partial^2}{\partial x\,\partial y}\left(B\frac{\partial^2 w}{\partial x\,\partial y}\right)+\frac{\partial}{\partial x}\left(S\frac{\partial w}{\partial x}\right)+\frac{\partial}{\partial y}\left(S\frac{\partial w}{\partial y}\right)$$
$$-k_w w+k_p\left(\frac{\partial^2 w}{\partial x^2}+\frac{\partial^2 w}{\partial y^2}\right)+f_z-c_{x,y}+c_{y,x}=\frac{\partial^2}{\partial t^2}(P_1 w)-\frac{\partial^2}{\partial t^2}\left(P_2\frac{\partial^2 w}{\partial x^2}\right)-\frac{\partial^2}{\partial t^2}\left(P_2\frac{\partial^2 w}{\partial y^2}\right), \quad (1b)$$

where $w=w(x,y,t)$ is the displacement in the z-direction (or deflection) of point $(x,y,0)$ on the plate mid-plane at time t (see Figure 1, left), and

$$D=\tfrac{1}{12}(\lambda+2\mu)h^3+\mu l^2 h+\tfrac{1}{2}(\lambda_0+2\mu_0)h^2,\quad C=\tfrac{1}{12}h^3\lambda-\mu l^2 h+\tfrac{1}{2}h^2(\lambda_0+\tau_0),$$
$$B=\tfrac{1}{3}\mu h^3+4\mu l^2 h+h^2(2\mu_0-\tau_0),\quad S=2\tau_0,\quad P_1=\rho h,\quad P_2=\tfrac{1}{12}\rho h^3. \quad (2)$$

In (1a), (1b) and (2), λ and μ are the Lamé constants, l is a couple stress-related material length scale parameter (e.g., Mindlin 1963; Park and Gao 2006), μ_0, λ_0 and τ_0 are the surface elastic constants, ρ is the density of the plate material, h is the uniform plate thickness, f_z is the z-component of the body force resultant (force per unit area) through the plate thickness acting on the plate mid-plane occupying the area R, c_x and c_y are, respectively, the x- and y-components of the body couple resultant (moment per unit area), k_w is the Winkler foundation modulus, and k_p is the Pasternak foundation modulus (e.g., Yokoyama 1996). The plate on the two-parameter elastic foundation is schematically shown in Figure 1 (right).

Note that in deriving the equations of motion leading to (1a), the modified couple stress theory [Yang et al. 2002; Park and Gao 2008] is used for the bulk plate material, and the surface elasticity theory [Gurtin and Murdoch 1975; 1978] is applied to the surface layers (with zero-thickness), which have distinct properties and are perfectly bonded to the bulk plate. When both the microstructure and surface energy effects are suppressed by setting $l=c_x=c_y=0$ and $\lambda_0=\mu_0=\tau_0=0$, equation (1a) reduces to

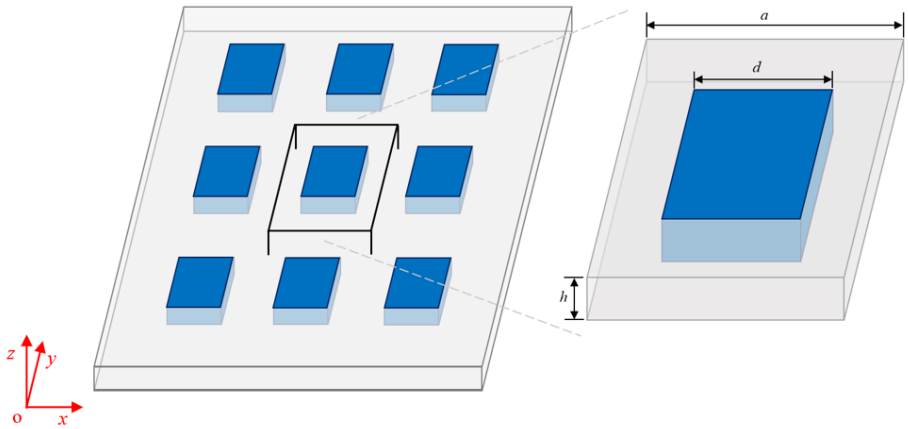

Figure 2. Periodic two-phase composite plate structure with a through-thickness square inclusion phase and a matrix phase: the composite plate structure (left) and the unit cell (right).

the equation of motion for a Kirchhoff plate resting on the Winkler–Pasternak elastic foundation based on classical elasticity.

Consider a periodic two-phase composite plate structure containing through-thickness square inclusions (as Phase I) embedded periodically in a host matrix (as Phase II), as shown in Figure 2. The periodic composite structure is infinitely large in the xy-plane. The unit cell for this periodic composite plate structure with a uniform thickness h is taken to be a square (with edge length a) containing a square inclusion (with edge length d) at its center, as displayed in Figure 3. The corresponding irreducible first Brillouin zone is also shown in Figure 3.

For the current periodic composite plate structure, the plane wave expansion method (e.g., Sigalas 1997) and Bloch's theorem for periodic media (e.g., Kittel 1986) can be applied. Accordingly, the deflection w can be expanded in a Fourier series as (e.g., Zhang et al. 2018b; Zhang and Gao 2018):

$$w(\boldsymbol{r}, t) = e^{i\boldsymbol{k}\cdot\boldsymbol{r}} \left(\sum_{\boldsymbol{G}'_{(m,n)}} w_{\boldsymbol{G}'_{(m,n)}} e^{i\boldsymbol{G}'_{(m,n)}\cdot\boldsymbol{r}} \right) e^{-i\omega t}, \tag{3}$$

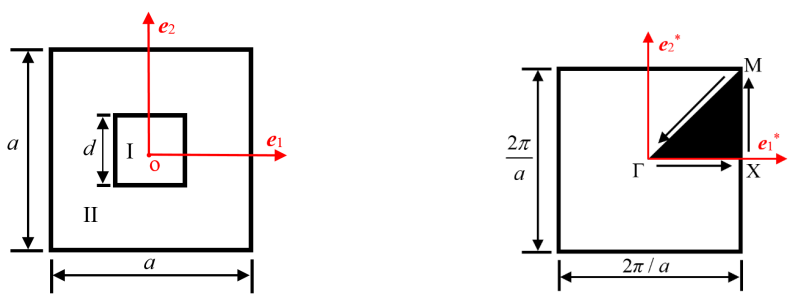

Figure 3. Left: unit cell of the periodic composite plate with a square inclusion (phase I). Right: the irreducible first Brillouin zone in the reciprocal lattice.

where $w_{\boldsymbol{G}'_{(m,n)}}$ is the Fourier coefficient, $\boldsymbol{r} = (x, y)$ is the position vector, $\boldsymbol{k} = (k_x, k_y)$ is the Bloch wave vector, $\boldsymbol{G}'_{(m,n)} = (2\pi m/a, 2\pi n/a) = (G'_x, G'_y)$ is the reciprocal lattice vector for a square lattice, ω is the angular frequency, i is the imaginary unit satisfying $i^2 = -1$, m and n are integers ranging from $-\infty$ to $+\infty$, and a is the lattice constant that is equal to the unit cell edge length (see Figure 3).

In addition, based on the periodicity of the composite plate structure, $D(\boldsymbol{r})$, $C(\boldsymbol{r})$, $B(\boldsymbol{r})$, $S(\boldsymbol{r})$, $P_1(\boldsymbol{r})$, $P_2(\boldsymbol{r})$, $k_w(\boldsymbol{r})$ and $k_p(\boldsymbol{r})$, which are material parameters involved in the wave equation in (1b), can each be written as a Fourier series:

$$\alpha(\boldsymbol{r}) = \sum_{\boldsymbol{G}_{(M,N)}} \alpha_{\boldsymbol{G}_{(M,N)}} e^{i\boldsymbol{G}_{(M,N)}\cdot\boldsymbol{r}}, \tag{4}$$

where α denotes D, C, B, S, P_1, P_2, k_w or k_p, $\boldsymbol{G}_{(M,N)} = (2\pi M/a, 2\pi N/a) = (G_x, G_y)$ is the reciprocal lattice vector in which the integers M and N range from $-\infty$ to $+\infty$, and $\alpha_{\boldsymbol{G}}$ is the Fourier coefficient satisfying

$$\alpha_{\boldsymbol{G}_{(M,N)}} = \frac{1}{A}\iint_{\Omega} \alpha(\boldsymbol{r})\, e^{-i\boldsymbol{G}_{(M,N)}\cdot\boldsymbol{r}} d\boldsymbol{r}, \tag{5}$$

where Ω is the square domain on the plate mid-plane in the unit cell, and A is the area of Ω. It can be readily shown that for a two-phase composite, $\alpha_{\boldsymbol{G}}$ is given by

$$\alpha_{\boldsymbol{G}} = \begin{cases} V_f^{(I)}\alpha_I + (1 - V_f^{(I)})\,\alpha_{II} & \text{when } \boldsymbol{G}_{(M,N)} = \boldsymbol{0}, \\ (\alpha_I - \alpha_{II})F(\boldsymbol{G}_{(M,N)}) & \text{when } \boldsymbol{G}_{(M,N)} \neq \boldsymbol{0}, \end{cases} \tag{6}$$

where α_I and α_{II} are respective property values for materials I and II, $V_f^{(I)}$ is the volume fraction of the inclusion phase (material I) given by $V_f^{(I)} = A^{(I)}/A$ (with $A^{(I)}$ being the mid-plane area of material I in the unit cell), and $F(\boldsymbol{G}_{(M,N)})$ is the shape function defined by

$$F(\boldsymbol{G}_{(M,N)}) = \frac{1}{A}\iint_{\Omega_1} e^{-i\boldsymbol{G}_{(M,N)}\cdot\boldsymbol{r}} d\boldsymbol{r}, \tag{7}$$

where Ω_I is the mid-plane domain occupied by material I in the unit cell.

For a square inclusion occupying the domain Ω_I (see Figure 3, left), $F(\boldsymbol{G}_{(M,N)})$ is given by (e.g., Susa 2002):

$$F(\boldsymbol{G}_{(M,N)}) = \begin{cases} \dfrac{2d}{a^2 G_x}\sin\dfrac{G_x d}{2} & \text{for } G_x \neq 0,\ G_y = 0, \\ \dfrac{2d}{a^2 G_y}\sin\dfrac{G_y d}{2} & \text{for } G_x = 0,\ G_y \neq 0, \\ \dfrac{4}{a^2 G_x G_y}\sin\dfrac{G_x d}{2}\sin\dfrac{G_y d}{2} & \text{for } G_x \neq 0,\ G_y \neq 0, \end{cases} \tag{8}$$

where d and a are, respectively, the edge lengths of the square inclusion Ω_I and unit cell Ω shown in Figure 3 (left).

Using (3) and (4) in (1b) (with $f_z = c_x = c_y = 0$) yields

$$(M)_{\boldsymbol{G}_{(M,N)}-\boldsymbol{G}'_{(m,n)}}\, w_{\boldsymbol{G}'_{(m,n)}} = \omega^2 (R)_{\boldsymbol{G}_{(M,N)}-\boldsymbol{G}'_{(m,n)}}\, w_{\boldsymbol{G}'_{(m,n)}}, \tag{9}$$

where

$$\begin{aligned}(M)_{\boldsymbol{G}_{(M,N)}-\boldsymbol{G}'_{(m,n)}} &= D_{\boldsymbol{G}-\boldsymbol{G}'}(k_x+G_x)^2(k_x+G'_x)^2 + C_{\boldsymbol{G}-\boldsymbol{G}'}(k_x+G_x)^2(k_y+G'_y)^2 \\ &\quad + D_{\boldsymbol{G}-\boldsymbol{G}'}(k_y+G_y)^2(k_y+G'_y)^2 + C_{\boldsymbol{G}-\boldsymbol{G}'}(k_y+G_y)^2(k_x+G'_x)^2 \\ &\quad + B_{\boldsymbol{G}-\boldsymbol{G}'}(k_x+G_x)(k_y+G_y)(k_x+G'_x)(k_y+G'_y) \\ &\quad + S_{\boldsymbol{G}-\boldsymbol{G}'}(k_x+G_x)(k_x+G'_x) + S_{\boldsymbol{G}-\boldsymbol{G}'}(k_y+G_y)(k_y+G'_y) \\ &\quad + (k_w)_{\boldsymbol{G}-\boldsymbol{G}'} + (k_p)_{\boldsymbol{G}-\boldsymbol{G}'}(k_x+G'_x)^2 + (k_p)_{\boldsymbol{G}-\boldsymbol{G}'}(k_y+G'_y)^2, \end{aligned} \tag{10}$$

$$(R)_{\boldsymbol{G}_{(M,N)}-\boldsymbol{G}'_{(m,n)}} = (P_1)_{\boldsymbol{G}-\boldsymbol{G}'} + (P_2)_{\boldsymbol{G}-\boldsymbol{G}'}\,(k_x+G'_x)^2 + (P_2)_{\boldsymbol{G}-\boldsymbol{G}'}\,(k_y+G'_y)^2, \tag{11}$$

$$w_{\boldsymbol{G}'_{(m,n)}} = \frac{1}{A}\iint_{\Omega} w e^{-i(\boldsymbol{G}'_{(m,n)}+\boldsymbol{k})\cdot\boldsymbol{r}}\,d\boldsymbol{r}, \tag{12}$$

in which

$$\alpha_{\boldsymbol{G}-\boldsymbol{G}'} = \frac{1}{A}\iint_{\Omega} \alpha e^{-i(\boldsymbol{G}_{(M,N)}-\boldsymbol{G}'_{(m,n)})\cdot\boldsymbol{r}}\,d\boldsymbol{r}, \tag{13}$$

where $\alpha_{\boldsymbol{G}-\boldsymbol{G}'}$ represents $D_{\boldsymbol{G}-\boldsymbol{G}'}$, $C_{\boldsymbol{G}-\boldsymbol{G}'}$, $B_{\boldsymbol{G}-\boldsymbol{G}'}$, $S_{\boldsymbol{G}-\boldsymbol{G}'}$, $(P_1)_{\boldsymbol{G}-\boldsymbol{G}'}$, $(P_2)_{\boldsymbol{G}-\boldsymbol{G}'}$, $(k_w)_{\boldsymbol{G}-\boldsymbol{G}'}$ or $(k_p)_{\boldsymbol{G}-\boldsymbol{G}'}$. Note that in reaching (9), use has been made of Laurent's rule for finding the Fourier coefficients of a product of two periodic functions (e.g., Li 1996; Cao et al. 2004).

When each of the integers m, n, M, and N in the Fourier series expansions for w and α (representing D, C, B, S, P_1, P_2, k_w or k_p) given in (3) and (4) is set to range from $-L$ to L, equation (9) leads to $(2L+1)^2$ equations, which can be written as

$$[(M)_{\boldsymbol{G}-\boldsymbol{G}'}]\{w_{\boldsymbol{G}'}\} = \omega^2[(R)_{\boldsymbol{G}-\boldsymbol{G}'}]\{w_{\boldsymbol{G}'}\}, \tag{14}$$

where

$$\left[(M)_{\boldsymbol{G}-\boldsymbol{G}'}\right] = \begin{bmatrix} M_{(\boldsymbol{G}_{(-L,-L)}-\boldsymbol{G}'_{(-L,-L)})} & M_{(\boldsymbol{G}_{(-L,-L)}-\boldsymbol{G}'_{(-L,-L+1)})} & \cdots & M_{(\boldsymbol{G}_{(-L,-L)}-\boldsymbol{G}'_{(L,L-1)})} & M_{(\boldsymbol{G}_{(-L,-L)}-\boldsymbol{G}'_{(L,L)})} \\ M_{(\boldsymbol{G}_{(-L,-L+1)}-\boldsymbol{G}'_{(-L,-L)})} & M_{(\boldsymbol{G}_{(-L,-L+1)}-\boldsymbol{G}'_{(-L,-L+1)})} & \cdots & M_{(\boldsymbol{G}_{(-L,-L+1)}-\boldsymbol{G}'_{(L,L-1)})} & M_{(\boldsymbol{G}_{(-L,-L+1)}-\boldsymbol{G}'_{(L,L)})} \\ \vdots & \vdots & & \vdots & \vdots \\ M_{(\boldsymbol{G}_{(L,L-1)}-\boldsymbol{G}'_{(-L,-L)})} & M_{(\boldsymbol{G}_{(L,L-1)}-\boldsymbol{G}'_{(-L,-L+1)})} & \cdots & M_{(\boldsymbol{G}_{(L,L-1)}-\boldsymbol{G}'_{(L,L-1)})} & M_{(\boldsymbol{G}_{(L,L-1)}-\boldsymbol{G}'_{(L,L)})} \\ M_{(\boldsymbol{G}_{(L,L)}-\boldsymbol{G}'_{(-L,-L)})} & M_{(\boldsymbol{G}_{(L,L)}-\boldsymbol{G}'_{(-L,-L+1)})} & \cdots & M_{(\boldsymbol{G}_{(L,L)}-\boldsymbol{G}'_{(L,L-1)})} & M_{(\boldsymbol{G}_{(L,L)}-\boldsymbol{G}'_{(L,L)})} \end{bmatrix}, \tag{15}$$

$$\left[(R)_{\boldsymbol{G}-\boldsymbol{G}'}\right] = \begin{bmatrix} R_{(\boldsymbol{G}_{(-L,-L)}-\boldsymbol{G}'_{(-L,-L)})} & R_{(\boldsymbol{G}_{(-L,-L)}-\boldsymbol{G}'_{(-L,-L+1)})} & \cdots & R_{(\boldsymbol{G}_{(-L,-L)}-\boldsymbol{G}'_{(L,L-1)})} & R_{(\boldsymbol{G}_{(-L,-L)}-\boldsymbol{G}'_{(L,L)})} \\ R_{(\boldsymbol{G}_{(-L,-L+1)}-\boldsymbol{G}'_{(-L,-L)})} & R_{(\boldsymbol{G}_{(-L,-L+1)}-\boldsymbol{G}'_{(-L,-L+1)})} & \cdots & R_{(\boldsymbol{G}_{(-L,-L+1)}-\boldsymbol{G}'_{(L,L-1)})} & R_{(\boldsymbol{G}_{(-L,-L+1)}-\boldsymbol{G}'_{(L,L)})} \\ \vdots & \vdots & & \vdots & \vdots \\ R_{(\boldsymbol{G}_{(L,L-1)}-\boldsymbol{G}'_{(-L,-L)})} & R_{(\boldsymbol{G}_{(L,L-1)}-\boldsymbol{G}'_{(-L,-L+1)})} & \cdots & R_{(\boldsymbol{G}_{(L,L-1)}-\boldsymbol{G}'_{(L,L-1)})} & R_{(\boldsymbol{G}_{(L,L-1)}-\boldsymbol{G}'_{(L,L)})} \\ R_{(\boldsymbol{G}_{(L,L)}-\boldsymbol{G}'_{(-L,-L)})} & R_{(\boldsymbol{G}_{(L,L)}-\boldsymbol{G}'_{(-L,-L+1)})} & \cdots & R_{(\boldsymbol{G}_{(L,L)}-\boldsymbol{G}'_{(L,L-1)})} & R_{(\boldsymbol{G}_{(L,L)}-\boldsymbol{G}'_{(L,L)})} \end{bmatrix} \tag{16}$$

are two $(2L+1)^2 \times (2L+1)^2$ matrices, and

$$\{w_{\boldsymbol{G}'}\} = \begin{Bmatrix} w_{\boldsymbol{G}'_{(-L,-L)}} \\ w_{\boldsymbol{G}'_{(-L,-L+1)}} \\ \vdots \\ w_{\boldsymbol{G}'_{(L,L-1)}} \\ w_{\boldsymbol{G}'_{(L,L)}} \end{Bmatrix} \tag{17}$$

is a $(2L+1)^2 \times 1$ matrix.

For the linear system of equations in (14) to have a nontrivial solution of $w_{\boldsymbol{G}'_{(m,n)}} \neq 0$, the determinant of the coefficient matrix must vanish, which gives

$$|[\boldsymbol{T}] - \omega^2[\boldsymbol{I}]| = 0, \tag{18}$$

as the characteristic equation of the eigenvalue problem defined in (14), where

$$[\boldsymbol{T}] = [(R)_{\boldsymbol{G}-\boldsymbol{G}'}]^{-1}[(M)_{\boldsymbol{G}-\boldsymbol{G}'}], \tag{19}$$

and $\boldsymbol{I}$ is the $(2L+1)^2 \times (2L+1)^2$ identity matrix. Equation (18) is a polynomial equation of degree $(2L+1)^2$ for ω^2. The roots of (18) gives the eigen-frequencies ω for a specified wave vector $\boldsymbol{k} = (k_x, k_y)$ in the first Brillouin zone (see Figure 3). The ranges of ω over which no real-valued wave vector $\boldsymbol{k}$ exists are known as band gaps. It is seen from (19), (18), (16), (15), (13), (11), (10), (8), (6) and (2) that the value of ω depends on the material constants λ, μ, l, λ_0, μ_0, τ_0 and ρ, the foundation moduli k_w and k_p, and the geometrical parameters a, d and h.

The classical elasticity-based band gaps for flexural elastic wave propagation in the periodic composite plate structure resting on the Winkler–Pasternak elastic foundation can be obtained as a special case by setting $l = 0$ and $\lambda_0 = \mu_0 = \tau_0 = 0$ in (19).

3. Numerical results

To demonstrate the new model formulated in Section 2, sample cases are quantitatively studied here. In obtaining the numerical results presented in this section, Material I is chosen to be iron, whose properties are as follows (e.g., Gurtin and Murdoch 1978): for the bulk, Young's modulus $E^{(I)} = 177.33\,\text{GPa}$, Poisson's ratio $\nu^{(I)} = 0.27$, $l^{(I)} = 6.76\,\mu\text{m}$, $\rho = 7\,\text{g/cm}^3$; for the surface layer, $\mu_0^{(I)} = 2.5\,\text{N/m}$, $\lambda_0^{(I)} = -8\,\text{N/m}$, $\tau_0^{(I)} = 1.7\,\text{N/m}$. The value of $l^{(I)}$ above is determined from $l = b_h/\sqrt{3(1-\nu)}$ (e.g., Lam et al. 2003; Park and Gao 2006) with $\nu^{(I)} = 0.27$ and $b_h^{(I)} = 10\,\mu\text{m}$ (e.g., Wang 2010). Material II is taken to be epoxy with the following properties [Chen and Wang 2014]: $E^{(II)} = 3.3\,\text{GPa}$, $\nu^{(II)} = 0.33$, $l^{(II)} = 16.93\,\mu\text{m}$, $\rho^{(II)} = 1.18\,\text{g/cm}^3$ for the bulk, and $\mu_0^{(II)} = 0.12406\,\text{N/m}$, $\lambda_0^{(II)} = 0.16376\,\text{N/m}$, $\tau_0^{(II)} = 0.045\,\text{N/m}$ for the surface layer. The value of $l^{(II)}$ given here is also calculated from $l = b_h/\sqrt{3(1-\nu)}$ but with $\nu^{(II)} = 0.33$ and $b_h^{(II)} = 24\,\mu\text{m}$ (e.g., Lam et al. 2003). The values of the surface elastic constants $\mu_0^{(II)}$ and $\lambda_0^{(II)}$ listed above are estimated using $\mu_0^{(II)} = \mu^{(II)} h^S$ and $\lambda_0^{(II)} = 2\lambda^{(II)}\mu^{(II)} h^S/(\lambda^{(II)} + \mu^{(II)})$ [Sharma and Ganti 2004], where h^S is the thickness of transition zone between the surface and bulk material and is taken to be 1 angstrom (e.g., Miller and Shenoy 2000), and $\lambda^{(II)}$ and $\mu^{(II)}$ are the Lamé

constants of the bulk epoxy given by $\lambda^{(II)} = E^{(II)}\nu^{(II)}/[(1+\nu^{(II)})(1-2\nu^{(II)})]$, $\mu^{(II)} = E^{(II)}/[2(1+\nu^{(II)})]$. In addition, $\tau_0^{(II)}$ is the surface tension for epoxy having a value of 45 mN/m (e.g., George 1993; Lewin et al. 2005). The foundation moduli k_w and k_p are non-dimensionalized to obtain $\overline{K}_w \equiv k_w a^4/D_C^{(I)}$, $\overline{K}_p \equiv k_p a^2/D_C^{(I)}$, with $D_C^{(I)} = E^{(I)}h^3/\{12[1-(\nu^{(I)})^2]\}$ being the plate flexural rigidity of material I. Moreover, the edge length of the square inclusion is taken to be $d = 0.4a$ (i.e., $V_f^I = d^2/a^2 = 0.16$) in all the calculations for simplicity. In Figures 4–7, the blue dot lines represent the wave frequency curves obtained from solving (18). It has been found that a convergent solution is attained in each case with $L = 7$.

In the numerical results provided below, the first band gap in each case is defined to be that between the fourth and fifth frequency curves, which is first observed for the periodic composite plate structure without the elastic foundation (see Figure 4, left). This corresponds to the lowest range of ω that prohibits flexural wave propagation in the periodic composite plate structure without the foundation. In addition, the first band gap for the composite plate structure with the elastic foundation, called the first foundation band gap, is identified and discussed.

3.1. ***Effects of the elastic foundation.*** Figure 4 (left column, top) illustrates the first band gap frequency range for the periodic composite plate structure (with $a = 1$ mm and $h = 15\,\mu$m) predicted by the current non-classical model without including the foundation effect (i.e., $\overline{K}_w = 0$, $\overline{K}_p = 0$), which is 175.42 kHz–190.50 kHz (marked in orange) for the wave frequency $f = \omega/(2\pi)$. Figure 4 (left column, middle and bottom) displays the first band gap and the first foundation band gap frequency ranges predicted by the new non-classical model with the foundation treated as a Winkler one (i.e., setting $k_p = 0$): 177.33 kHz–192.17 kHz and 0 kHz–20.66 kHz for the case with $\overline{K}_w = 10$ and $\overline{K}_p = 0$; and 193.67 kHz–206.85 kHz and 0 kHz–62.97 kHz for the case with $\overline{K}_w = 100$ and $\overline{K}_p = 0$. Figure 4 (right column) shows the first band gap and the first foundation band gap for the composite plate structure predicted by the current non-classical model incorporating the Winkler–Pasternak foundation effect: 186.82 kHz–199.32 kHz and 0 kHz–20.69 kHz for the case with $\overline{K}_w = 10$ and $\overline{K}_p = 1$; 202.33 kHz–213.52 kHz and 0 kHz–63.18 kHz for the case with $\overline{K}_w = 100$ and $\overline{K}_p = 1$. For the case with $\overline{K}_w = 100$ and $\overline{K}_p = 10$, the first foundation band gap frequency range is 0 kHz–64.17 kHz, but no first band gap exists between the fourth and fifth frequency curves. However, a band gap is found between the first and second frequency curves, which is marked in green in Figure 4 (right column, bottom). This is called the second foundation band gap, which also exists in the cases with $\overline{K}_w = 100$ and $\overline{K}_p = 1$ and $\overline{K}_w = 100$ and $\overline{K}_p = 0$, as illustrated in Figure 4. Figure 4 shows the second foundation band gap frequency ranges predicted by the current non-classical model: 71.07 kHz–85.92 kHz for the case with $\overline{K}_w = 100$ and $\overline{K}_p = 0$; 74.68 kHz–89.57 kHz for the case with $\overline{K}_w = 100$ and $\overline{K}_p = 1$; and 100.54 kHz–117.30 kHz for the case with $\overline{K}_w = 100$ and $\overline{K}_p = 10$. From these frequency ranges, the band gaps can be readily determined, which are listed in Table 1.

From Figure 4 and Table 1, it is observed that the first band gap size decreases with the increase of either $\overline{K}_w$ or $\overline{K}_p$. However, the first foundation band gap size increases with these two foundation moduli. Additionally, Figure 4 shows that the presence of either the Winkler–Pasternak foundation or the Winkler foundation reduces the first band gap size, and the effect of the former is more significant than that of the latter.

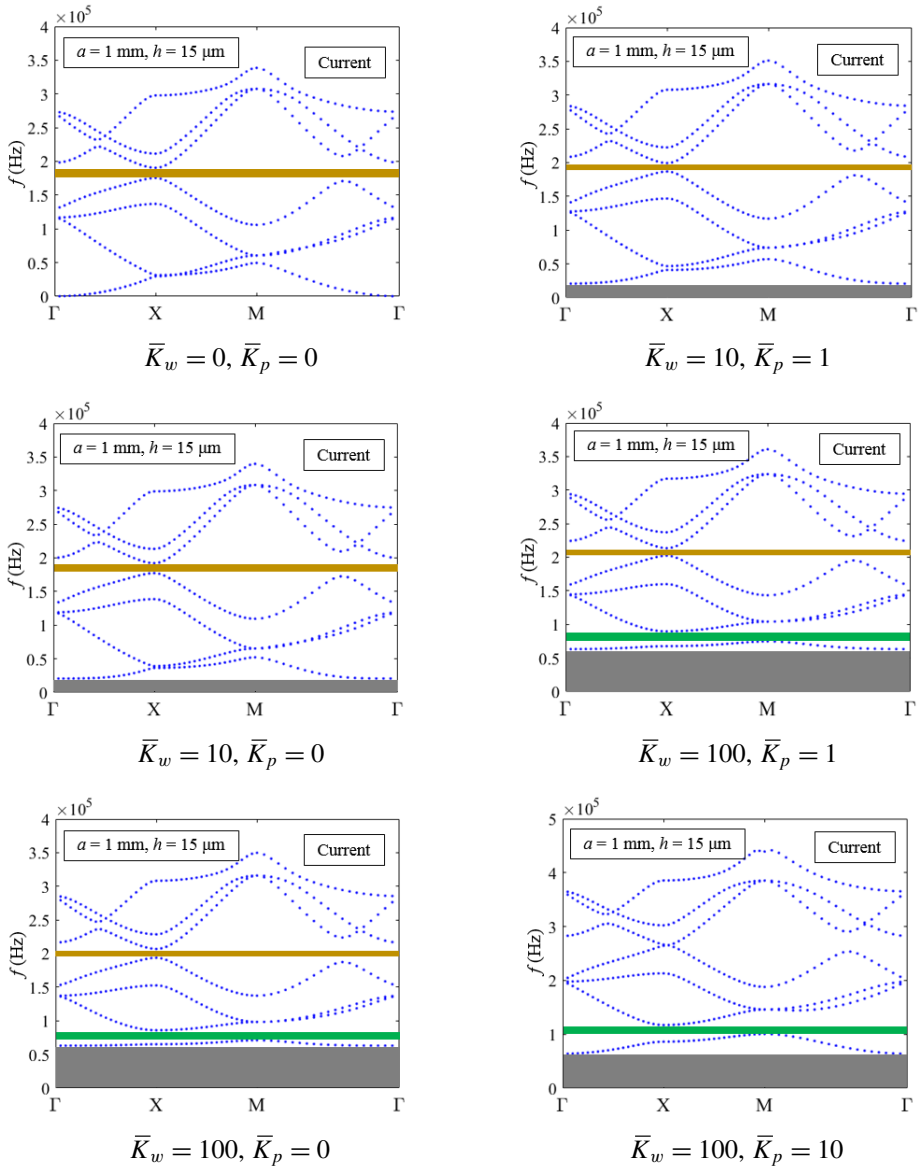

Figure 4. Band gaps for the periodic composite plate structure predicted by the current model. The Bloch wave vector $\boldsymbol{k} = (k_x, k_y)$ at Γ, X and M is, respectively, $(0, 0)$, $(\pi/a, 0)$ and $(\pi/a, \pi/a)$ (see Figure 3, right).

3.2. ***Effects of the microstructure and surface energy.*** Figure 5 displays the band gaps for the periodic composite plate structure predicted by the current model with $a = 1\,\text{mm}$, $\overline{K}_w = 10$, and $\overline{K}_p = 1$. Figure 5 (left column) shows the first band gap frequency ranges (in orange) and the first foundation band gap frequency ranges (in grey) predicted by the current non-classical model for different values of the plate thickness: 186.82 kHz–199.32 kHz and 0 kHz–20.69 kHz for $h = 15\,\mu\text{m}$; 322.81 kHz–355.31 kHz

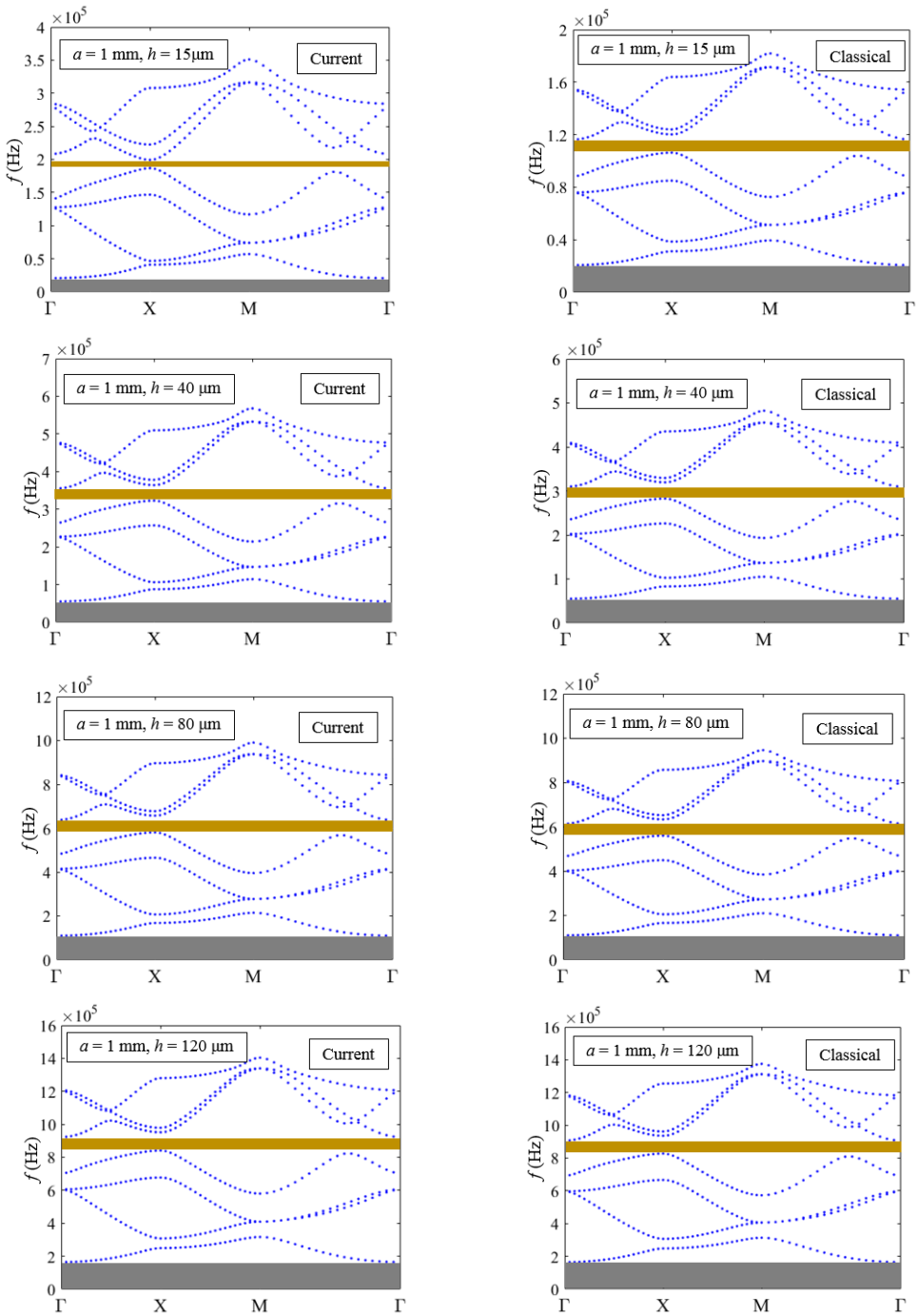

Figure 5. Band gaps for the periodic composite plate structure (with $a = 1$ mm, $\overline{K}_w = 10$ and $\overline{K}_p = 1$) predicted by the current model (left column) and the classical model (right column). The Bloch wave vector $\boldsymbol{k} = (k_x, k_y)$ at Γ, X and M is, respectively, $(0, 0)$, $(\pi/a, 0)$, and $(\pi/a, \pi/a)$ (see Figure 3, right).

Foundation moduli $\overline{K}_w$	$\overline{K}_p$	First band gap (kHz)	First foundation band gap (kHz)	Second foundation band gap (kHz)
0	0	15.08	NA	NA
10	0	14.84	20.66	NA
10	1	12.50	20.69	NA
100	0	13.18	62.97	14.85
100	1	11.19	63.18	14.89
100	10	NA	64.17	16.76

Table 1. Band gaps for the periodic composite plate structure with different values of the foundation moduli $\overline{K}_w$ and $\overline{K}_p$ predicted by the current model (with $a = 1\,\text{mm}$, $h = 15\,\mu\text{m}$).

h (μm)	Band gap (kHz) Current model	Band gap (kHz) Classical model	Relative difference (%)
15	12.50	10.22	22.31
40	32.50	27.22	19.40
80	56.98	54.20	5.13
120	82.58	80.70	2.33

Table 2. First band gaps for the periodic composite plate structure with different values of the plate thickness h.

and 0 kHz–55 kHz for $h = 40\,\mu$m; 581.07 kHz–638.05 kHz and 0 kHz–109.86 kHz for $h = 80\,\mu$m; and 841.20 kHz–923.78 kHz and 0 kHz–164.73 kHz for $h = 120\,\mu$m.

Figure 5 (right column) illustrates the first band gap frequency ranges (in orange) and the first foundation band gap frequency ranges (in grey) predicted by the classical elasticity-based model for different values of the plate thickness: 106.28 kHz–116.50 kHz and 0 kHz–20.59 kHz for $h = 15\,\mu$m; 282.65 kHz–309.87 kHz and 0 kHz–54.9 kHz for $h = 40\,\mu$m; 560.00 kHz–614.20 kHz and 0 kHz–109.8 kHz for $h = 80\,\mu$m; and 827.20 kHz–907.90 kHz and 0 kHz–164.68 kHz for $h = 120\,\mu$m. These frequency ranges give the two types of band gaps shown in Tables 2 and 3, respectively. In each case listed in Tables 2 and 3, the band gap value based on the classical model is used as the base value to compute the relative difference.

It is observed from Figure 5 and Table 2 that the first band gap size predicted by the current non-classical model is always larger than that predicted by the classical model. However, the difference between the two band gap sizes diminishes with the increase of the plate thickness h. When $h = 15\,\mu$m, the band gap predicted by the current model is 1.22 times as large as that predicted by the classical model (with a relative difference of 22.31%). When $h = 120\,\mu$m, the former is only 1.02 times of the latter, giving a relative difference of 2.33%. This shows that the effects of microstructure and surface energy on the first band gap are significant only for very thin plates.

Figure 5 and Table 3 reveal that the first foundation band gap predicted by the current non-classical model is always larger than that predicted by the classical model. However, the relative difference

h (μm)	Band gap (kHz) Current model	Band gap (kHz) Classical model	Relative difference (%)
15	20.69	20.59	0.49
40	55.00	54.90	0.18
80	109.86	109.80	0.05
120	164.73	164.68	0.03

Table 3. First foundation band gaps for the periodic composite plate structure with different values of the plate thickness h.

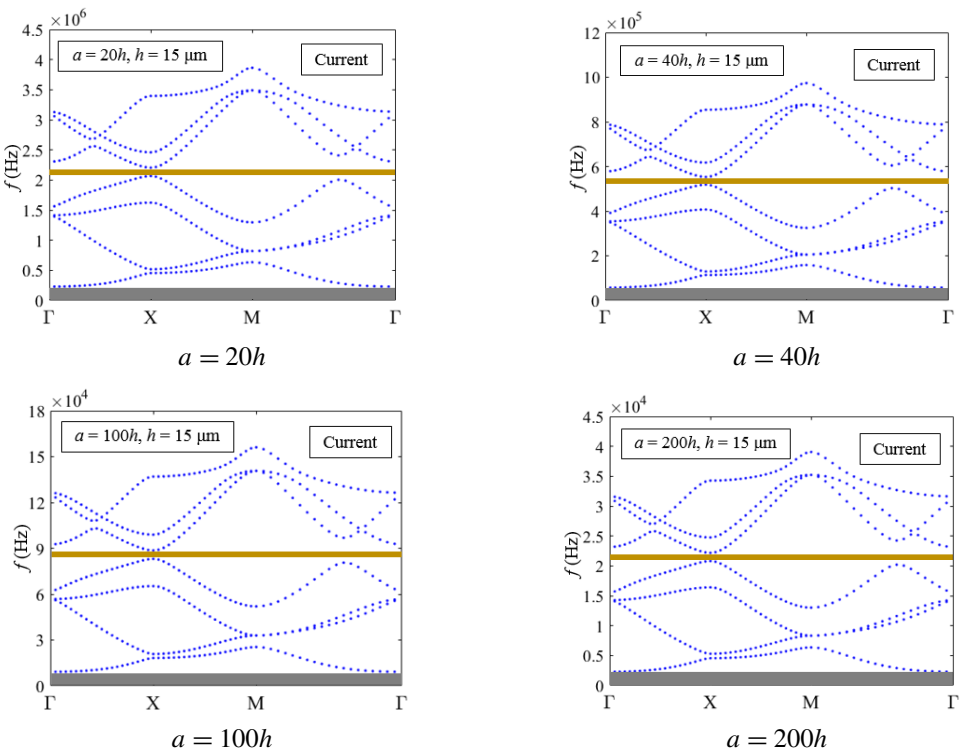

Figure 6. Band gaps for the periodic composite plate structure (with $h = 15\,\mu$m, $\overline{K}_w = 10$ and $\overline{K}_p = 1$) predicted by the current model. The Bloch wave vector $\boldsymbol{k} = (k_x, k_y)$ at Γ, X and M is, respectively, $(0, 0)$, $(\pi/a, 0)$, and $(\pi/a, \pi/a)$ (see Figure 3, right).

decreases with the increase of the plate thickness h. In addition, this difference is negligibly small compared to the difference between the two first band gap values. This indicates that the effects of microstructure and surface energy on the first foundation band gap are insignificant even for very thin plates.

3.3. ***Effect of the unit cell length.*** Figure 6 illustrates the first band gap frequency ranges (in orange) and the first foundation band gap frequency ranges (in grey) for the periodic composite plate structure

a	First band gap (kHz)	First foundation band gap (kHz)
$20h$	138.7	229.89
$40h$	34.74	57.48
$100h$	5.56	9.20
$200h$	1.38	2.30

Table 4. Band gaps for the periodic composite plate structure with different values of the unit cell length a predicted by the current model (with $h = 15\,\mu$m, $\overline{K}_w = 10$, and $\overline{K}_p = 1$).

a	First band gap (Hz)	First foundation band gap (Hz)
$20h$	1700	3431
$40h$	425.8	857.9
$100h$	68.15	137.26
$200h$	17.03	34.32

Table 5. Band gaps for the periodic composite plate structure with different values of the unit cell length a predicted by the current model (with $h = 1$ mm, $\overline{K}_w = 10$, and $\overline{K}_p = 1$).

predicted by the current model for different values of the unit cell length a. The plate thickness is $h = 15\,\mu$m, and the elastic foundation moduli are $\overline{K}_w = 10$ and $\overline{K}_p = 1$ in all cases.

The first band gap frequency range and the first foundation band gap frequency range are, respectively, 2065.9 kHz–2204.6 kHz and 0 kHz–229.89 kHz for the case with $a = 20h$ shown in Figure 6 (left column, top); 518.45 kHz–553.19 kHz and 0 kHz–57.48 kHz for the case with $a = 40h$ displayed in Figure 6 (right column, top); 83.07 kHz–88.63 kHz and 0 kHz–9.20 kHz for the case with $a = 100h$ depicted in Figure 6 (left column, bottom); and 20.80 kHz–22.18 kHz and 0 kHz–2.30 kHz for the case with $a = 200h$ illustrated in Figure 6 (right column, bottom). From these frequency ranges, the band gaps can be readily obtained, which are given in Table 4.

From Figure 6 and Table 4, it is observed that the frequency for producing the first band gap gets lower when the unit cell length a becomes larger and the sizes of the first band gap and the first foundation band gap decrease as a increases. The effect of the unit cell length is further illustrated in Figure 7.

Figure 7 shows the first band gap frequency ranges (in orange) predicted by the current model for the composite plate structure with $h = 1$ mm, $\overline{K}_w = 10$, $\overline{K}_p = 1$ and different values of the unit cell length: 17639 Hz–19339 Hz for $a = 20h$, 4426.1 Hz–4851.9 Hz for $a = 40h$, 708.93 Hz–777.08 Hz for $a = 100h$, and 177.27 Hz–194.30 Hz for $a = 200h$. Also, Figure 7 displays the first foundation band gap frequency ranges for different values of the unit cell length: 0 kHz–3431 MHz, 0 kHz–857.9 MHz, 0 kHz–137.26 MHz and 0 kHz–34.32 MHz for the cases with $a = 20h$, $40h$, $100h$, and $200h$, respectively. From these frequency ranges, the band gaps are computed and given in Table 5.

From Figure 7 and Table 5, it is observed that both the frequency for producing the first band gap and the sizes of the first band gap and the first foundation band gap in the current cases with $h = 1$ mm

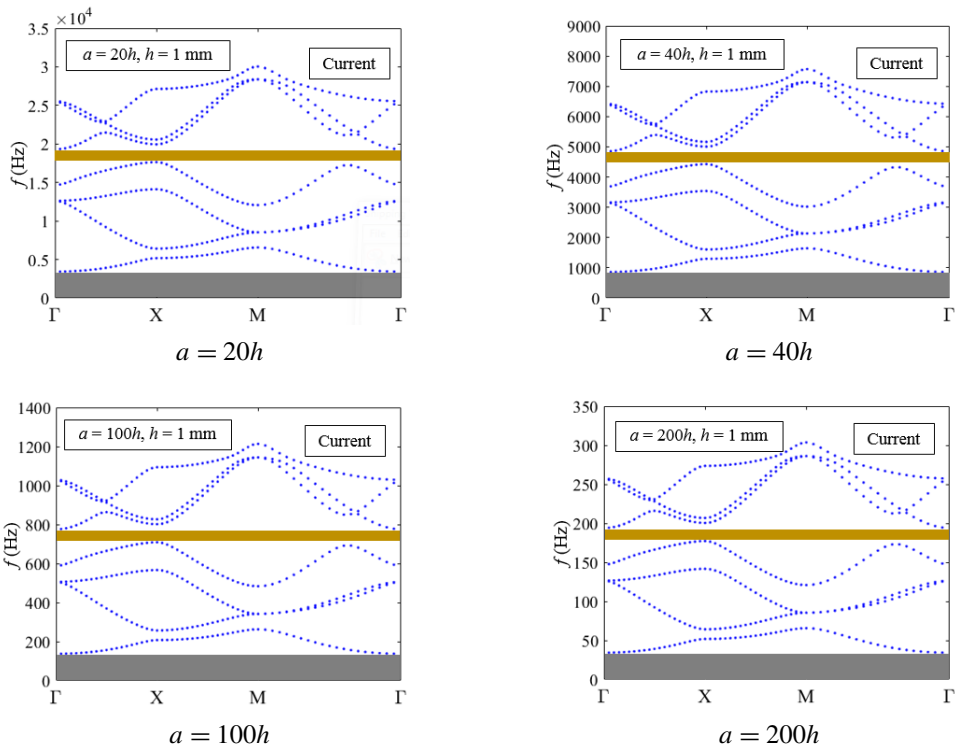

Figure 7. Band gaps for the periodic composite plate structure (with $h = 1$ mm, $\overline{K}_w = 10$ and $\overline{K}_p = 1$) predicted by the current model. The Bloch wave vector $\boldsymbol{k} = (k_x, k_y)$ at Γ, X and M is, respectively, $(0, 0)$, $(\pi/a, 0)$, and $(\pi/a, \pi/a)$ (see Figure 3, right).

decrease as the unit cell length a increases, which is the same trend as that seen from Figure 6 for the cases with $h = 15\,\mu$m, a much smaller plate thickness. This shows that the effect of the unit cell length on band gaps exists at different length scales.

3.4. ***Effects of the volume fraction.*** The variations of the first band gap and the first foundation band gap with the volume fraction of material I (the inclusion phase) predicted by the current non-classical model are displayed in Figures 8 and 9, respectively. For comparison purposes, the variations predicted by the classical model are also shown in Figures 8 and 9. The numerical values for wave frequency plotted in Figures 8 and 9 are obtained from solving (18), with the convergent solution attained when $L = 7$ in each case. The properties adopted here for materials I and II are the same as those used to generate the numerical results displayed in Figures 4–7. In addition, $a = 1$ mm, $h = 15\,\mu$m, $\overline{K}_w = 10$ and $\overline{K}_p = 1$ are employed in the calculations here.

From Figure 8, it is observed that the first band gap predicted by the current model starts at $V_f^{(I)} = 9.5\%$ and increases to its maximum of 13.82 kHz at $V_f^{(I)} = 20\%$, after which it decreases with $V_f^{(I)}$ until its disappearance at $V_f^{(I)} = 30\%$. Also, the first band gap predicted by the classical model increases from zero to its maximum value 13.31 kHz as $V_f^{(I)}$ goes from 9% to 21%, then it decreases with $V_f^{(I)}$ until vanishing at $V_f^{(I)} = 30\%$.

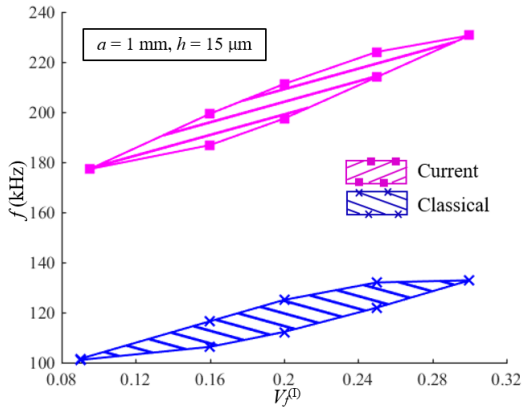

Figure 8. First band gap changing with $V_f^{(I)}$ predicted by the current and classical models for the periodic composite plate structure (with $a = 1$ mm, $h = 15\,\mu$m, $\overline{K}_w = 10$ and $\overline{K}_p = 1$).

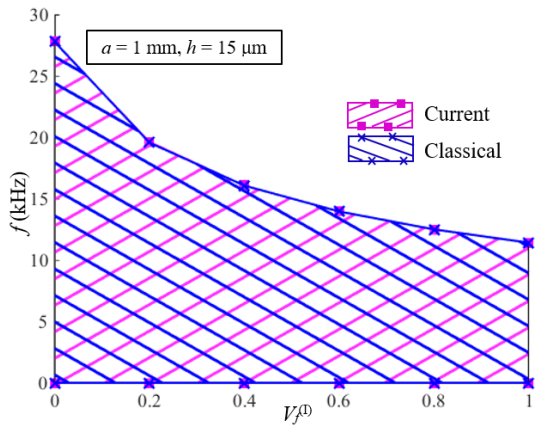

Figure 9. First foundation band gap changing with $V_f^{(I)}$ predicted by the current and classical models for the periodic composite plate structure (with $a = 1$ mm, $h = 15\,\mu$m, $\overline{K}_w = 10$, and $\overline{K}_p = 1$).

From Figure 9, it is seen that the first foundation band gap predicted by the current non-classical model or the classical elasticity-based model gradually decreases with the increase of $V_f^{(I)}$ from 0% to 100%. Also, it is observed that the first foundation band gap values predicted by the current non-classical model and those predicted by the classical model are very close, thereby indicating that the effects of microstructure and surface energy on the first foundation band gap are not significant. This agrees with what is observed from Figure 5 and Table 3.

From Figures 8 and 9, it is clear that the volume fraction does have a significant effect on the first band gap and the first foundation band gap for the periodic composite plate structure according to both the current non-classical and the classical models. This shows that large band gaps can be generated by adjusting the volume fraction of the inclusion phase.

4. Summary

A new model is provided for determining elastic wave band gaps in a periodic composite plate structure. It is based on a non-classical Kirchhoff plate model, the plane wave expansion method and the Bloch theorem. The current non-classical model recovers the classical model as a special case after neglecting the microstructure and surface energy effects. The new model simultaneously incorporates the microstructure, surface energy and elastic foundation effects for the first time. In addition, the band gaps predicted by the current model vary with the unit cell size and volume fraction of the inclusion phase.

Numerical results show that the first band gap predicted by the current model including the foundation effect is smaller than that without considering this effect, and the first foundation band gap increases with the elastic foundation moduli. In addition, the first band gap predicted by the new non-classical model is seen to be always larger than that based on the classical model, with the difference being significant for very thin plates. It is also observed that the first band gap frequency and the sizes of the first band gap and the first foundation band gap decrease with the increase of the unit cell length. Finally, it is found that the volume fraction has a significant effect on the band gap size, indicating that large band gaps can be achieved by tailoring the volume fraction.

References

[Bacigalupo and Gambarotta 2017] A. Bacigalupo and L. Gambarotta, "Dispersive wave propagation in two-dimensional rigid periodic blocky materials with elastic interfaces", *J. Mech. Phys. Solids* **102** (2017), 165–186.

[Cao et al. 2004] Y. Cao, Z. Hou, and Y. Liu, "Convergence problem of plane-wave expansion method for phononic crystals", *Phys. Lett. A* **327** (2004), 247–253.

[Chen and Wang 2014] Y. Chen and L. Wang, "Periodic co-continuous acoustic metamaterials with overlapping locally resonant and Bragg band gaps", *Appl. Phys. Lett.* **105**:19 (2014), article id 191907 (5 pages).

[Chen et al. 2017] Y. Chen, T. Li, F. Scarpa, and L. Wang, "Lattice metamaterials with mechanically tunable Poisson's ratio for vibration control", *Phys. Rev. Appl.* **7**:2 (2017), article id 024012 (11 pages).

[Gao and Park 2007] X.-L. Gao and S. K. Park, "Variational formulation of a simplified strain gradient elasticity theory and its application to a pressurized thick-walled cylinder problem", *Int. J. Solids Struct.* **44**:22-23 (2007), 7486–7499.

[Gao and Zhang 2016] X.-L. Gao and G. Y. Zhang, "A non-classical Kirchhoff plate model incorporating microstructure, surface energy and foundation effects", *Contin. Mech. Therm.* **28**:1-2 (2016), 195–213.

[Gao et al. 2018] R. Z. Gao, G. Y. Zhang, T. Ioppolo, and X.-L. Gao, "Elastic wave propagation in a periodic composite beam structure: a new model for band gaps incorporating surface energy, transverse shear and rotational inertia effects", *J. Micromech. Molecular Phys.* **3** (2018), article id 1840005 (22 pages).

[George 1993] G. A. George, "Surface modification and analysis of ultra-high-modulus polyethylene fibres for composites", pp. 161–201, in *Polymer surfaces and interfaces*, vol. II, edited by W. J. Feast et al., Wiley, Chichester, England, 1993.

[Gurtin and Murdoch 1975] M. E. Gurtin and A. I. Murdoch, "A continuum theory of elastic material surfaces", *Arch. Ration. Mech. Anal.* **57**:4 (1975), 291–323.

[Gurtin and Murdoch 1978] M. E. Gurtin and A. I. Murdoch, "Surface stress in solids", *Int. J. Solids Struct.* **14**:6 (1978), 431–440.

[Kittel 1986] C. Kittel, *Introduction to solid state physics*, Wiley, New York, 1986.

[Lam et al. 2003] D. C. C. Lam, F. Yang, A. C. M. Chong, J. Wang, and P. Tong, "Experiments and theory in strain gradient elasticity", *J. Mech. Phys. Solids* **51**:8 (2003), 1477–1508.

[Lewin et al. 2005] M. Lewin, A. Mey-Marom, and R. Frank, "Surface free energies of polymeric materials, additives and minerals", *Polym. Adv. Technol.* **16** (2005), 429–441.

[Li 1996] L. Li, "Use of Fourier series in the analysis of discontinuous periodic structures", *J. Opt. Soc. Am. A* **13** (1996), 1870–1876.

[Li et al. 2016] Y. Li, P. Wei, and Y. Zhou, "Band gaps of elastic waves in 1-D phononic crystal with dipolar gradient elasticity", *Acta Mech.* **227**:4 (2016), 1005–1023.

[Liu and Hussein 2012] L. Liu and M. I. Hussein, "Wave motion in periodic flexural beams and characterization of the transition between Bragg scattering and local resonance", *J. Appl. Mech.* (*ASME*) **79**:1 (2012), article id 011003 (17 pages).

[Liu et al. 2012] W. Liu, J. Chen, Y. Liu, and X. Su, "Effect of interface/surface stress on the elastic wave band structure of two-dimensional phononic crystals", *Phys. Lett. A* **376**:4 (2012), 605–609.

[Madeo et al. 2016] A. Madeo, G. Barbagallo, M. V. d'Agostino, L. Placidi, and P. Neff, "First evidence of non-locality in real band-gap metamaterials: determining parameters in the relaxed micromorphic model", *Proc. Royal Soc. Lond. A* **472** (2016), article id 20160169 (21 pages).

[Maranganti and Sharma 2007] R. Maranganti and P. Sharma, "A novel atomistic approach to determine strain-gradient elasticity constants: Tabulation and comparison for various metals, semiconductors, silica, polymers and the (ir) relevance for nanotechnologies", *J. Mech. Phys. Solids* **55**:9 (2007), 1823–1852.

[Mi et al. 2008] C. Mi, S. Jun, D. A. Kouris, and S. Y. Kim, "Atomistic calculations of interface elastic properties in noncoherent metallic bilayers", *Phys. Rev. B* **77**:7 (2008), article id 075425 (12 pages).

[Miller and Shenoy 2000] R. E. Miller and V. B. Shenoy, "Size-dependent elastic properties of nanosized structural elements", *Nanotechnology* **11**:3 (2000), 139–147.

[Mindlin 1963] R. D. Mindlin, "Influence of couple-stresses on stress concentrations", *Exp. Mech.* **3**:1 (1963), 1–7.

[Park and Gao 2006] S. K. Park and X.-L. Gao, "Bernoulli–Euler beam model based on a modified couple stress theory", *J. Micromech. Microeng.* **16**:11 (2006), 2355–2359.

[Park and Gao 2008] S. K. Park and X.-L. Gao, "Variational formulation of a modified couple stress theory and its application to a simple shear problem", *Z. Angew. Math. Phys.* **59**:5 (2008), 904–917.

[Piccolroaz and Movchan 2014] A. Piccolroaz and A. B. Movchan, "Dispersion and localisation in structured Rayleigh beams", *Int. J. Solids Struct.* **51**:25-26 (2014), 4452–4461.

[Piccolroaz et al. 2017] A. Piccolroaz, A. B. Movchan, and L. Cabras, "Rotational inertia interface in a dynamic lattice of flexural beams", *Int. J. Solids Struct.* **112** (2017), 43–53.

[Sharma and Ganti 2004] P. Sharma and S. Ganti, "Size-dependent Eshelby's tensor for embedded nano-inclusions incorporating surface/interface energies", *J. Appl. Mech.* (*ASME*) **71**:5 (2004), 663–671.

[Shodja et al. 2012] H. M. Shodja, F. Ahmadpoor, and A. Tehranchi, "Calculation of the additional constants for fcc materials in second strain gradient elasticity: behavior of a nano-size Bernoulli–Euler beam with surface effects", *J. Appl. Mech.* (*ASME*) **79**:2 (2012), article id 021008 (8 pages).

[Sigalas 1997] M. M. Sigalas, "Elastic wave band gaps and defect states in two-dimensional composites", *J. Acoust. Soc. Am.* **101**:3 (1997), 1256–1261.

[Sigalas and Economou 1994] M. M. Sigalas and E. N. Economou, "Elastic waves in plates with periodically placed inclusions", *J. Appl. Phys.* **75**:6 (1994), 2845–2850.

[Steigmann and Ogden 1997] D. J. Steigmann and R. W. Ogden, "Plane deformations of elastic solids with intrinsic boundary elasticity", *Proc. Royal Soc. Lond. A* **453**:1959 (1997), 853–877.

[Steigmann and Ogden 1999] D. J. Steigmann and R. W. Ogden, "Elastic surface-substrate interactions", *Proc. Royal Soc. Lond. A* **455**:1982 (1999), 437–474.

[Susa 2002] N. Susa, "Large absolute and polarization-independent photonic band gaps for various lattice structures and rod shapes", *J. Appl. Phys.* **91**:6 (2002), 3501–3510.

[Wang 2010] L. Wang, "Size-dependent vibration characteristics of fluid-conveying microtubes", *J. Fluid. Struct.* **26**:4 (2010), 675–684.

[Xiao et al. 2012] Y. Xiao, J. Wen, and X. Wen, "Flexural wave band gaps in locally resonant thin plates with periodically attached spring-mass resonators", *J. Phys. D Appl. Phys.* **45**:19 (2012), article id 195401 (12 pages).

[Yang et al. 2002] F. Yang, A. C. M. Chong, D. C. C. Lam, and P. Tong, "Couple stress based strain gradient theory for elasticity", *Int. J. Solids Struct.* **39**:10 (2002), 2731–2743.

[Yokoyama 1996] T. Yokoyama, "Vibration analysis of Timoshenko beam-columns on two-parameter elastic foundations", *Comput. Struct.* **61**:6 (1996), 995–1007.

[Zhang and Gao 2018] G. Y. Zhang and X.-L. Gao, "Elastic wave propagation in 3-D periodic composites: band gaps incorporating microstructure effects", *Compos. Struct.* **204** (2018), 920–932.

[Zhang and Parnell 2017] P. Zhang and W. J. Parnell, "Band gap formation and tunability in stretchable serpentine interconnects", *J. Appl. Mech.* (*ASME*) **84**:9 (2017), article id 091007 (7 pages).

[Zhang and Zhao 2016] Y. Zhang and Y.-P. Zhao, "Measuring the nonlocal effects of a micro/nanobeam by the shifts of resonant frequencies", *Int. J. Solids Struct.* **102-103** (2016), 259–266.

[Zhang et al. 2018a] G. Y. Zhang, X.-L. Gao, J. E. Bishop, and H. E. Fang, "Band gaps for elastic wave propagation in a periodic composite beam structure incorporating microstructure and surface energy effects", *Compos. Struct.* **189** (2018), 263–272.

[Zhang et al. 2018b] G. Y. Zhang, X.-L. Gao, and S. R. Ding, "Band gaps for wave propagation in 2-D periodic composite structures incorporating microstructure effects", *Acta Mech.* **229**:10 (2018), 4199–4214.

Received 20 Oct 2018. Accepted 25 Dec 2018.

GONGYE ZHANG: gyzhang@seu.edu.cn
Jiangsu Key Laboratory of Engineering Mechanics, School of Civil Engineering, Southeast University, Nanjing, Jiangsu, China

XIN-LIN GAO: xlgao@smu.edu
Department of Mechanical Engineering, Southern Methodist University, Dallas, TX, United States

JOURNAL OF MECHANICS OF MATERIALS AND STRUCTURES
Vol. 14, No. 2, 2019
dx.doi.org/10.2140/jomms.2019.14.237

DYNAMIC ANALYSIS OF A MASS TRAVELING ON A SIMPLY SUPPORTED NONHOMOGENEOUS BEAM COMPOSED OF TRANSVERSELY EMBEDDED PERIODIC ARRAYS

YI-MING WANG AND HUNG-CHIEH LIU

Periodically embedded specified materials and laminas into the beam of a beam-mass system to form a stiffness-driven nonhomogeneous beam having the potential to shift its specific stiffness to avoid the happening of large amplitude vibration and resonance is worthy of note. However, if the arrangement of composed materials and layers of the beam is changed, the developed model generally has to be reestablished. To propose a model that can be used to analyze beams consisting of different assemblies of materials and laminas is of great importance. Another point is using specified materials and laminas, which are periodically embedded into a beam to form transversely periodic arrays, to make the beam have the capability to change its specific stiffness to satisfy designing requirement. The Fourier-series based approach is employed to take into account the periodicity of material properties and matching conditions across laminas' interfaces. The influence produced by the arrays to the dynamics of the system is examined.

Result shows that the axial Young's modulus and density of the proposed beam are biaxial periodic functions. Different arrangements of embedded arrays bring different stiffness shifting potential of the beam to reduce the vibration of the system. With proper choice of the stiffness and thickness ratios between the arrays and basic layers, the growth of small amplitude vibration into large motion regime can be attenuated. Meanwhile, by changing the thickness ratios in the width and height directions, there exist seven possible compositions of the beam. It discloses that despite without considering the material damping, the proposed beam still has good ability to diminish the beam vibration even after the mass left the beam.

1. Introduction

Stiffness-driven beam-like members have been widely found in civil and mechanical engineering. Due to high demand of operational safety of structures and mechanical systems, flexible members having the capability to shift their stiffness-to-weight-ratio to avoid the happening of large amplitude vibration are of great importance. For a beam-mass system, if the beam has the potential to vary its transverse frequency, the dynamic response of the system is able to be improved. In other words, short useful life and failure of structures caused by the occurrence of large amplitude vibration can be attenuated.

Mohebpour et al. [2016] studied the dynamics of a mass riding on an inclined symmetric cross-ply laminated beam. Based on classical laminated theory and finite element approach, the equations of motion were derived and solved. Their results indicated that a laminated composite beam had better bending stiffness than a homogeneous beam. Meanwhile, the orientation of the layer had influential effect to the bending stiffness of the composite beam.

Keywords: transversely periodic arrays, stiffness-driven beam, Fourier series, thickness ratio.

Misiurek and Śniady [2013] investigated the dynamics of a force moving at constant speed on a simply supported sandwich beam. A closed-form solution was obtained by the method of superimposed deflections. They pointed out that when the speed of a point force was less and larger than the shear wave velocity of the beam, different forms of the closed-form solutions were presented. Song et al. [2018] made a parametric study to the dynamics of a sandwich plate subjected to a mass moving with constant speed. The composite plate was composed of two isotropic face plates and a viscoelastic inner layer. The effects produced by different boundary constraints were determined. They showed that using nonhomogeneous structural members improved the dynamic behaviors of structures.

Tao et al. [2016] analyzed the dynamics of a fiber metal laminated beam induced by the motion of a riding load and the change of environmental temperature. The beam consisted of three symmetric cross-ply fiber reinforced layers and two metal layers. Their results disclosed that the geometric properties and environmental temperature played key roles to the mid-span response of the beam. Meanwhile, the increase of temperature decreased the bending stiffness of the beam.

Wang [2009] considered the dynamics induced by a mass traveling on a beam having periodic arrays in axial direction. The inhomogeneous beam was assumed to be composed of two different laminas. The Fourier-series based approach was introduced to take over the axial periodicity of the beam. This is also one of the bases of this study.

Sayyad and Ghugal [2017] made an excellent review of existing studies on bending, buckling and free vibration of laminated composite and sandwich beams. They discussed many popular methods that have been applied on the analysis, e.g., finite element approaches based on classical and refined theories, displacement fields of various equivalent single layer, layerwise, and zig-zag theories, and etc. Many other authors used these approaches to study the vibration of laminated composite beams. For example, Rao et al. [2001] investigated the natural frequencies of a laminated simply supported beam. Friswell and Lees [2001] discussed the modes of vibration for nonhomogeneous damped beams composed of two materials with different stiffness, damping and mass properties. Li et al. [2008] studied the free vibration and buckling activities of laminated composite beams having lay-up in lateral direction subjected by axially loading. In general, the problems were solved by assuming that the variation of material properties was piecewise constants and continuity constraints were applied at the interface of two neighboring segments. As the number of segments increased, a large number of unknowns were generated and great computational efforts were needed.

Sheng and Wang [2018] investigated the nonlinear phenomena and resonant conditions of functionally graded (FG) beams when the beams were subjected to parametric and external excitations. They pointed out that, depending on the values of parameters, e.g., excitation frequency, excitation amplitude, damping, volume fraction exponent, etc., chaotic response could occur when the magnitude of excitation was greater than the Euler's buckling load. Kahya and Turan [2018] analyzed the free vibration and stability of FG sandwich beams without/with axial forces. Based on shear deformation theory, a finite element model was obtained to derive the natural frequency and buckling loads of FG sandwich beams. The effects of slenderness ratio and layer thickness to the fundamental frequency and buckling loads were examined. Lee and Lee [2017] studied the free vibration of FG beams by using transfer matrix method. They showed that when the slenderness ratio was not large, the effect produced by the coupling between the axial and bending displacements to the natural frequency of a beam shouldn't be ignored. Nevertheless, the coupling effect becomes tiny when the slenderness ratio is large.

Şimşek [2010], Şimşek and Kocatürk [2009], and Şimşek et al. [2012] employed Euler–Bernoulli beam theory combined with numerical integration to study the dynamics of a FG and an axially FG (AFG) beams with simply supported boundary condition, respectively. For the first two, they assumed that the variation of material properties of the beam was continuous in thickness direction and could be expressed by power-law functions. For the latter, the material properties were assumed to vary continuously in the axial direction. Their results showed that using FG/AFG beams had influential benefits to the dynamics of a beam-mass system.

Although stiffness-driven beam-like members with or without riding masses had been studied by many authors, generally, the mathematic model developed was able to be used for the scheme proposed in that study only. In other words, if the structure of the composite beam is changed, e.g., rearranging the assembly of composed materials/laminas, the mathematic model may have to be remodeled. Unlike other papers, in this study, the proposed model can be diversely applied on a composite beam having different arrangements and compositions of materials and layers. Meanwhile, by transversely applying specified arrays to form a periodic-array beam, the beam has the capability to shift its specific stiffness and frequency. This means that the embedded arrays can be treated as tuning parameters to the bending frequency of the beam. By assuming that all the layers of the periodic arrays are bonded, the periodicity and matching conditions across the interfaces arrays are taken into account by the Fourier series expansion. The dynamic characteristics induced by the inhomogeneity of materials/laminas of the proposed beam and the motion of the riding mass are examined.

2. Basic formulas

As shown in Figure 1 (top), a mass traveling on a finite simply supported periodic-array beam with rectangular cross-section having length ℓ, width W, and thickness H is considered. Here, the occurrence of delamination due to the interaction between laminas is prevented by the adjacent layers; hence, in the modeling, the arrays with bonded strips and layers are assumed. The Cartesian coordinate system xyz is on the inextensible centroidal axis of the beam ($y = 0$). Prior to the mass being set on motion, the beam is in straight and in the state of equilibrium. The composite beam is composed of a number of bonded periodic layers, basic and embedded laminas. The basic layer is a homogeneous lamina with the material c having the Young's modulus E_c and density ρ_c. The embedded lamina consists of periodic strips which are formed by two different rectangular strips of a and b of length ℓ; the Young's moduli and densities of the former and latter are E_a, E_b, ρ_a, and ρ_b, respectively. For the embedded lamina, the periodic arrangement is two strips of b separated by one strip of a; these strips are stacked in a row in the width (z) direction. For the beam, the periodic pattern is two basic layers separated by one embedded lamina and they are piled symmetrically in the thickness (y) direction. Hence, unless otherwise specified, the central ply of the embedded lamina is the strip a and the middle layer of the beam is the embedded lamina. By assuming that the beam is an inhomogeneous continuum, the two different strips of the embedded lamina and the two different layers of the beam are accounted for by spatial variation of the moduli of their phases. Therefore, the Young's modulus and density of the beam are biaxial periodic functions. It is known that the Fourier analysis can be applied in a limited range and will converge to that function in the interval. As a result, the variation of the moduli of the embedded lamina and the beam is expressed by the Fourier series expansion.

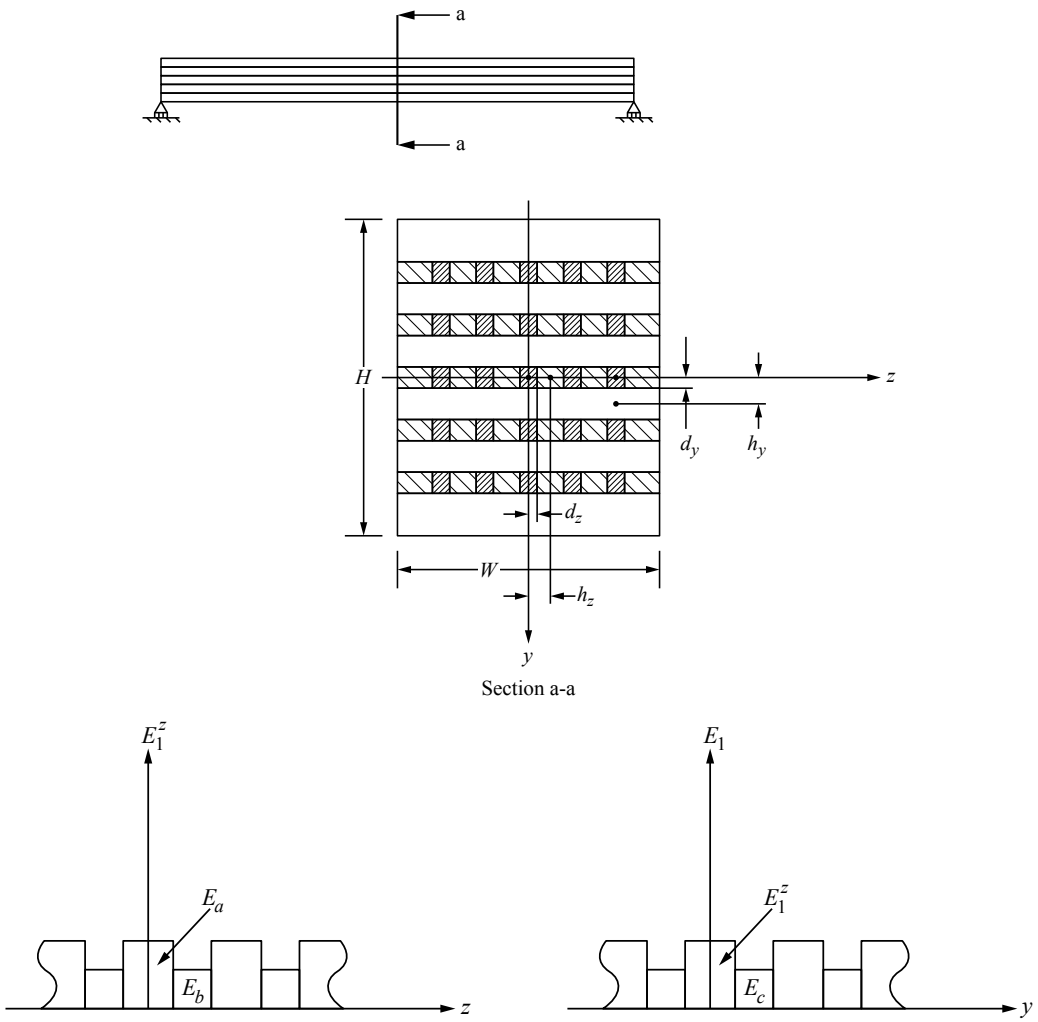

Figure 1. The schematic diagram of the cross-section of the periodic-array beam (top) and the Fourier series representation (bottom).

Due to symmetry, the variation of the moduli is assumed to be an even periodic function and is stated as a series of cosine terms; therefore, the number of strips and layers is odd. Referring to Figure 1 (bottom), let E_1^z, which is a periodic function in the z direction, be the axial Young's modulus of an embedded layer and be given by

$$E_1^z(z) = E_a \frac{d_z}{h_z} + E_b\left(1 - \frac{d_z}{h_z}\right) + (E_a - E_b)\sum_{j=1}^{\infty} \frac{2}{j\pi} \sin\left(\frac{j\pi d_z}{h_z}\right) \cos\left(\frac{j\pi z}{h_z}\right)$$
$$\equiv E_{10}^z + \sum_{j=1}^{\infty} E_{1j}^z \cos\left(\frac{j\pi z}{h_z}\right), \tag{1a}$$

where

$$E_{1j}^z = \frac{2}{h_z}\int_0^{h_z} E_1^z(z)\cos\frac{j\pi z}{h_z}dz = (E_a - E_b)\frac{2}{j\pi}\sin\frac{j\pi d_z}{h_z}.$$

Here, d_z is one-half of the thickness of the strip a; h_z is one-half of the distance between the midpoint of two strips of b separated by one ply of a. Therefore, d_z/h_z presents the thickness ratio of the strip a that is present in one period $2h_z$ in the z (width) direction. Similarly, the axial Young's modulus of the beam $E_1(y, z)$ is also periodic in the y direction. Hence, one has

$$\begin{aligned} E_1(y,z) &= E_1^z\left(\frac{d_y}{h_y}\right) + E_c\left(1-\frac{d_y}{h_y}\right) + (E_1^z - E_c)\sum_{k=1}^{\infty}\frac{2}{k\pi}\sin\left(\frac{k\pi d_y}{h_y}\right)\cos\frac{k\pi y}{h_y} \\ &\equiv E_{10} + \sum_{k=1}^{\infty} E_{1k}\cos\frac{k\pi y}{h_y}, \end{aligned} \tag{1b}$$

where

$$E_{1k} = \frac{2}{h_y}\int_0^{h_y} E_1(y,z)\cos\frac{k\pi y}{h_y}dy = (E_1^z - E_c)\frac{2}{k\pi}\sin\frac{k\pi d_y}{h_y}.$$

Here, d_y is one-half of the thickness of an embedded lamina; h_y is one-half of the distance between the midpoint of two basic layers separated by one embedded lamina; d_y/h_y denotes the thickness ratio of an embedded lamina that is present in one period $2h_y$ in the y direction. Hence, there exist seven possible compositions of the composite beam:

(1) $0 < d_z < h_z$ and $0 < d_y < h_y$. The beam consists of embedded and basic laminas. The Young's moduli of the embedded lamina and the beam are given by (1a) and (1b).

(2) $d_z = 0$ and $0 < d_y < h_y$. The embedded layer reduces to a homogeneous lamina with the strip b. The axial Young's moduli of the embedded layer and the beam become, respectively,

$$E_1^z = E_b \quad \text{and} \quad E_1 = E_1(y) = E_{10} + \sum_{k=1}^{\infty} E_{1k}\cos\frac{k\pi y}{h_y}, \tag{1c}$$

where

$$E_{10} = E_b\left(\frac{d_y}{h_y}\right) + E_c\left(1-\frac{d_y}{h_y}\right) \quad \text{and} \quad E_{1k} = (E_b - E_c)\frac{2}{k\pi}\sin\left(\frac{k\pi d_y}{h_y}\right).$$

(3) $d_z = h_z$ and $0 < d_y < h_y$. For this condition, one has

$$E_1^z = E_a \quad \text{and} \quad E_1 = E_1(y) = E_{10} + \sum_{k=1}^{\infty} E_{1k}\cos\frac{k\pi y}{h_y}, \tag{1d}$$

where

$$E_{10} = E_a\left(\frac{d_y}{h_y}\right) + E_c\left(1-\frac{d_y}{h_y}\right) \quad \text{and} \quad E_{1k} = (E_a - E_c)\frac{2}{k\pi}\sin\left(\frac{k\pi d_y}{h_y}\right).$$

(4) $d_y = 0$. This means the vanish of embedded layers; the beam is homogeneous with the material c, i.e., $E_1 = E_c$.

(5) $0 < d_z < h_z$ and $d_y = h_y$. The basic layer disappears; the beam is composed of two different kinds of vertical plies of the materials of a and b. The axial Young's modulus of the beam then turns into $E_1 = E_1(z) = E_1^z$ (1a).

(6) $d_z = 0$ and $d_y = h_y$. The beam becomes a homogeneous beam with the material b, i.e., $E_1 = E_b$.

(7) $d_z = h_z$ and $d_y = h_y$. The axial Young's modulus of the beam reduces to $E_1 = E_a$.

It is seen that the proposed model can be diversely used to simulate the composite beams having different arrangements of laminas and compositions of materials. Similar to the periodic distribution of Young's modulus, the density of the beam has the form

$$\rho(y,z) = \rho^z\left(\frac{d_y}{h_y}\right) + \rho_c\left(1-\frac{d_y}{h_y}\right) + (\rho^z - \rho_c)\sum_{q=1}^{\infty}\frac{2}{q\pi}\sin\left(\frac{q\pi d_y}{h_y}\right)\cos\frac{q\pi y}{h_y} \equiv \rho_0 + \sum_{q=1}^{\infty}\rho_q\cos\frac{q\pi y}{h_y}, \quad (2)$$

where ρ^z is the density of an embedded lamina and is given by

$$\rho^z = \rho^z(z) = \rho_0^z + \sum_{p=1}^{\infty}\rho_p^z\cos\left(\frac{p\pi z}{h_z}\right),$$

with

$$\rho_0^z = \rho_a\frac{d_z}{h_z} + \rho_b\left(1-\frac{d_z}{h_z}\right) \qquad \text{and} \qquad \rho_p^z = \frac{2}{h_z}\int_0^{h_z}\rho^z(z)\cos\frac{r\pi z}{h_z}dz = (\rho_a - \rho_b)\frac{2}{p\pi}\sin\frac{p\pi d_z}{h_z}.$$

Therefore, the mass per unit length of the beam can be obtained by

$$m = \int_{-W/2}^{W/2}\int_{-H/2}^{H/2}\rho(y,z)\,dy\,dz = m_0 + \sum_{p=1}^{\infty}m_p + \sum_{q=1}^{\infty}m_q + \sum_{p=1}^{\infty}\sum_{q=1}^{\infty}m_{pq} \equiv m_r(\hat{m}_0 + \hat{m}_{pq}), \quad (3)$$

where $m_r = \rho_r WH$, $r = c, b, a$. The selection of the subscript r depends on $\hat{d}_z$ and $\hat{d}_y$. For example, $r = c$ if cases (1)–(4) are considered; $r = b$ if cases (5) and (6) are taken into account; $r = a$ if case (7) is examined. Other parameters in (3) are given by

$$\hat{m}_0 = \left(\hat{\rho}_a\hat{d}_z + \hat{\rho}_b(1-\hat{d}_z)\right)\hat{d}_y + \hat{\rho}_c(1-\hat{d}_y),$$

with

$$\hat{\rho}_a = \frac{\rho_a}{\rho_r}, \quad \hat{\rho}_b = \frac{\rho_b}{\rho_r}(1-\delta_{ra}), \quad \hat{\rho}_c = \frac{\rho_{cb}}{\rho_r}\delta_{rc}, \quad \hat{d}_z = \frac{d_z}{h_z}, \quad \hat{d}_y = \frac{d_y}{h_y},$$

$$\hat{m}_{pq} = \sum_{p=1}^{\infty} \hat{m}_p + \sum_{q=1}^{\infty} \hat{m}_q + \sum_{p=1}^{\infty}\sum_{q=1}^{\infty} \hat{m}_{pq},$$

$$\hat{m}_p = \frac{1}{2}\hat{d}_y \hat{h}_z \left[(\hat{\rho}_a - \hat{\rho}_b) \left(\frac{2}{p\pi} \right)^2 \sin(p\pi \hat{d}_z) \sin \frac{p\pi}{\hat{h}_z} \right], \quad \text{with } \hat{h}_z = \frac{2h_z}{W},$$

$$\hat{m}_q = \frac{1}{2}\hat{h}_y \left[\left(\hat{\rho}_a \hat{d}_z + \hat{\rho}_b (1 - \hat{d}_z) \right) - \hat{\rho}_c \right] \left(\frac{2}{q\pi} \right)^2 \sin(q\pi \hat{d}_y) \sin \frac{q\pi}{\hat{h}_y}, \quad \text{with } \hat{h}_y = \frac{2h_y}{H},$$

$$\hat{m}_{pq} = \frac{1}{4}\hat{h}_z \hat{h}_y \left[(\hat{\rho}_a - \hat{\rho}_b) \left(\frac{2}{p\pi} \right)^2 \left(\frac{2}{q\pi} \right)^2 \sin \frac{p\pi}{\hat{h}_z} \sin(q\pi \hat{d}_y) \sin \frac{q\pi}{\hat{h}_y} \right],$$

where $\hat{h}_z = 2h_z/W =$ the ratio of the distance of the period $2h_z$ to the width of the beam, $\hat{h}_y = 2h_y/H =$ the ratio of the length of the period $2h_y$ to the height of the beam, $\delta_{rp} =$ the Dirac delta symbol with $p = a, c$.

Since the axial Young's modulus of the beam is also spatial dependence, $E_1 = E_1(y, z)$, prior to deriving the equations of motion of the system, the resultant bending moment about the neutral axis of the cross section of the beam at time t has to be determined and is given by

$$\widetilde{M} = \kappa \int_{-H/2}^{H/2} \int_{-W/2}^{W/2} E_1(y, z)\, y^2 dz\, dy, \tag{4a}$$

where κ is the beam curvature; y is the perpendicular distance from the neutral axis to the centroid of the differential area dA, $dA = dy\, dz$. After some manipulations, it yields

$$\widetilde{M} = \kappa I \left[E_{10} + \sum_{j=1}^{\infty} E_{1j} - \hat{I}_y \left(\sum_{k=1}^{\infty} E_{1k} + \sum_{j=1}^{\infty}\sum_{k=1}^{\infty} E_{1jk} \right) \right] \equiv \kappa E_r I \left(\hat{E}_{10} + \hat{E}^t_{1jk} \right), \tag{4b}$$

where $I = \frac{1}{12} W H^3$, $\hat{I}_y = I_y/I = \frac{1}{8}(\hat{h}_y)^3$ with $I_y = \frac{1}{12} W h_y^3$,

$$\hat{E}_{10} = [\hat{E}_a \hat{d}_z + \hat{E}_b (1 - \hat{d}_z)]\, \hat{d}_y + \hat{E}_c (1 - \hat{d}_y), \qquad \text{with } \hat{E}_a = \frac{E_a}{E_r}, \quad \hat{E}_b = \frac{E_b}{E_r}(1 - \delta_{ra}), \quad \hat{E}_c = \frac{E_c}{E_r}\delta_{rc},$$

$$\hat{E}^t_{1jk} = \sum_{j=1}^{\infty} \hat{E}_{1j} - \hat{I}_y \left(\sum_{k=1}^{\infty} \hat{E}_{1k} + \sum_{j=1}^{\infty}\sum_{k=1}^{\infty} \hat{E}_{1jk} \right),$$

$$\hat{E}_{1j} = \frac{1}{2}\hat{d}_y \hat{h}_z \left[(\hat{E}_a - \hat{E}_b) \left(\frac{2}{j\pi} \right)^2 \sin(j\pi \hat{d}_z) \sin \frac{j\pi}{\hat{h}_z} \right],$$

$$\hat{E}_{1k} = 6[\hat{E}_a \hat{d}_z + \hat{E}_b (1 - \hat{d}_z) - \hat{E}_c] \left(\frac{2}{k\pi} \right)^4 \sin(k\pi \hat{d}_y) \sin \frac{k\pi}{\hat{h}_y},$$

$$\hat{E}_{1jk} = 3\hat{h}_z \left[(\hat{E}_a - \hat{E}_b) \left(\frac{2}{j\pi} \right)^2 \left(\frac{2}{k\pi} \right)^4 \sin(j\pi \hat{d}_z) \sin \frac{j\pi}{\hat{h}_z} \sin(k\pi \hat{d}_y) \sin \frac{k\pi}{\hat{h}_y} \right].$$

From (3) and (4b), one finds that increasing the number of layers decreases the distance of the period h_y. Therefore, when the beam has a many of layers, the length of h_y becomes a tiny value and the terms $\hat{h}_y$ and

$\hat{I}_y$ approach to zero such that $\hat{m}_{pq} \to \sum_{p=1}^{\infty} \hat{m}_p$ and $\hat{E}^t_{1jk} \to \sum_{j=1}^{\infty} \hat{E}_{1j}$. This means that as h_y decreases, the Young's modulus and mass of the composite beam converge to $E_{10} + \sum_{j=1}^{\infty} E_{1j}$ and $m_0 + \sum_{p=1}^{\infty} m_p$, respectively. Similar phenomenon is also observed when h_z and $\hat{h}_z$ are taken into account.

As mentioned previously, the number of strips and layers is always odd. The distance of the periods h_z and h_y along the width and height can be calculated and yields

$$h_z = \frac{W}{2i \pm 2\hat{d}_z}, \quad 0 < \hat{d}_z < 1, \quad i = 2, 3, 4, \ldots, \tag{5a}$$

$$h_y = \frac{H}{2j \pm 2\hat{d}_y}, \quad 0 < \hat{d}_y < 1, \quad j = 2, 3, 4, \ldots, \tag{5b}$$

where i and j are the number of the strips b and the total of basic layers, respectively. The plus and minus signs used in (5a) are when the number of the strips b is less than and greater than the total of the strips a, respectively. Therefore, for the plus and minus signs, the number of strips of an embedded lamina is equal to $5 + 4(i-1)$ and $3 + 4(i-1)$, $i = 1, 2, 3, \ldots$, respectively. The selection of the plus and minus signs in (5b) can be done similarly. For example, a sandwich (three horizontal layers) beam is composed of one embedded lamina (core) and two basic layers. The embedded lamina consists of three strips of a of equal lateral thickness $2d_z$ and four strips of b of equal lateral thickness $2(h_z - d_z)$. The lengths of h_z and h_y are given by $h_z = W/(8 - 2\hat{d}_z)$, $0 < \hat{d}_z < 1$, and $h_z = H/(4 - 2\hat{d}_y)$, $0 < \hat{d}_y < 1$, respectively. Another example is that a composite beam consists of five horizontal layers, three embedded and two basic laminas. The period h_y then is $h_y = H/(4 + 2\hat{d}_y)$. Note that (5a) and (5b) are not applied to the cases when $\hat{d}_z = 0, 1$ and $\hat{d}_y = 0, 1$, respectively. For $\hat{d}_z = 0$ and 1, the embedded lamina reduces to a homogeneous layer having the materials b and a, respectively. For $\hat{d}_y = 0$ and 1, the beam is homogeneous having the material c and the beam consists of two different vertical layers of a and b, respectively.

As the structure of the composite beam is established, in the following, the dynamics of a beam-mass system is considered. From Figure 2, the mechanics of the interface between the mass and beam is determined by modeling the mass as a rigid body that is rolling on the beam. The equations governing the motion of the system can be derived from the dynamic equilibrium of forces and momenta and are given by

$$\boldsymbol{F}_{,s} + \boldsymbol{f} = m_r(\hat{m}_0 + \hat{m}_{pq})\,\boldsymbol{r}_{,tt}, \quad 0 < s < l, \ t > 0, \tag{6a}$$

$$\boldsymbol{F} = T\hat{\boldsymbol{\tau}} + V\boldsymbol{n} = (T\cos\theta - V\sin\theta)\,\boldsymbol{i} + (T\sin\theta + V\cos\theta)\,\boldsymbol{j}, \tag{6b}$$

$$E_r(\hat{E}_{10} + \hat{E}^t_{1jk})\,I v_{,sss} + V = 0, \tag{6c}$$

with the inextensibility constraint $\boldsymbol{r}_{,s} \cdot \boldsymbol{r}_{,s} = 1$. The corresponding boundary conditions for the simply supported beam are

$$u(0,t) = v(0,t) = v(\ell,t) = \frac{\partial^2 v(0,t)}{\partial s^2} = \frac{\partial^2 v(\ell,t)}{\partial s^2} = 0, \tag{7a}$$

$$T(\ell,t)(1 + u_{,s}) + E_r(\hat{E}_{10} + \hat{E}^t_{1jk})\,I v_{,sss}\, v_{,s} = 0, \quad \text{at } s = \ell, \tag{7b}$$

where (7b) is obtained when the resultant force in the $\boldsymbol{i}$ direction vanishes at $s = \ell$. In above equations, $\boldsymbol{i}$, $\boldsymbol{j}$ = the unit vectors in the horizontal and gravitational (transverse) directions, respectively, $\boldsymbol{r}(s,t) =$

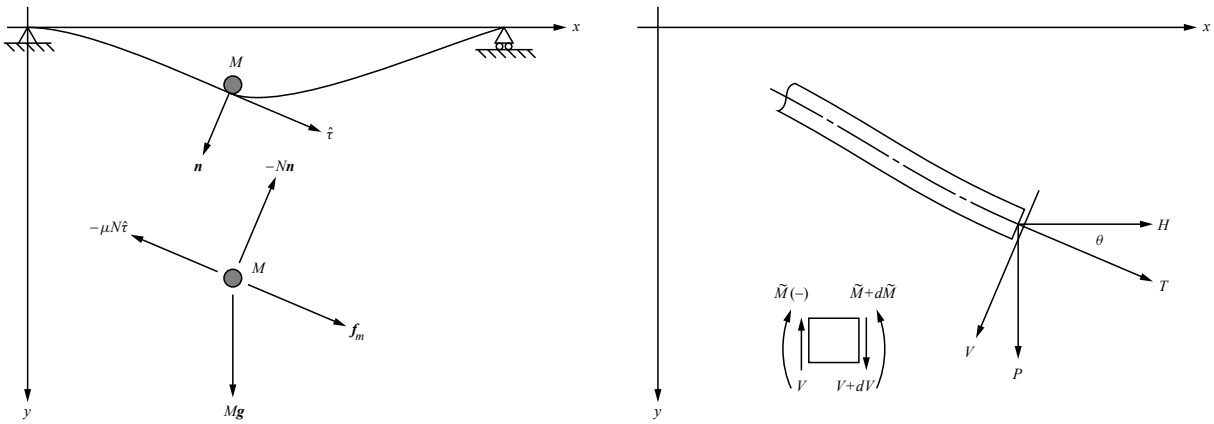

Figure 2. System configuration (left) and force equilibrium diagram (right).

$[x(s)+u(s,t)]\boldsymbol{i}+v(s,t)\boldsymbol{j}$ with $u(s,t)$ and $v(s,t)$ being the axial and transverse displacements of the beam measured from the undeformed state, respectively, $\boldsymbol{n}$, $\hat{\boldsymbol{\tau}}=$ the unit normal and tangent vectors to the beam configuration, respectively, T, V, $\theta=$ the axial and transverse forces in the beam and the angle between the neutral axis of the beam and the x-axis, respectively. The subscripts s and t mean the s and t differentiation. In this study, the slenderness ratio of the beam $s=\ell(\sqrt{I/A})^{-1}$ [Han et al. 1999] selected is a large value such that the Euler–Bernoulli beam theory is applicable to be applied, where A is the cross-sectional area of the beam. By considering the small deformation theory and applying the inextensibility constraint $\boldsymbol{r}_{,s}\cdot\boldsymbol{r}_{,s}=1$, the axial displacement of the beam is in the second order nonlinearity and can be neglected. Therefore, $\boldsymbol{r}(s,t)=x(s)\boldsymbol{i}+v(s,t)\boldsymbol{j}$ and $\hat{\tau}=\boldsymbol{i}+v_{,s}\boldsymbol{j}$. The force $\boldsymbol{f}$ represents the external forces including the weight and the reactions of the moving mass upon the composite beam and can be expressed as

$$\boldsymbol{f}=(N\boldsymbol{n}+\mu N\hat{\boldsymbol{\tau}})\,\bar{\delta}\big(s-\bar{s}(t)\big), \tag{8}$$

where N, μ, $\bar{\delta}[s-\bar{s}(t)]$, and $\bar{s}(t)$ represent the dynamic interaction force between the mass and beam, coefficient of friction, Dirac delta function, and the position of mass along the arc of the beam at time t, respectively. The equation of motion of the moving mass is given by (Figure 2)

$$M\boldsymbol{a}_M=M\frac{d^2}{dt^2}\big[\boldsymbol{r}\big(\bar{s}(t),t\big)\big]=M[\boldsymbol{r}_{,ss}(\bar{s}_{,t})^2+2\boldsymbol{r}_{,st}\,\bar{s}_{,t}+\boldsymbol{r}_{,s}\,\bar{s}_{,tt}+\boldsymbol{r}_{,tt}]=M\boldsymbol{g}+\boldsymbol{f}_{\hat{\tau}}-\mu N\hat{\boldsymbol{\tau}}-N\boldsymbol{n}, \tag{9}$$

where $\boldsymbol{a}_M=$ the acceleration of the mass, $M=$ total mass of the moving mass, $\boldsymbol{g}=g\boldsymbol{j}$, $\boldsymbol{f}_{\hat{\tau}}=Mf\hat{\boldsymbol{\tau}}=Mf(\boldsymbol{i}+v_{,s}\boldsymbol{j})=$ tangential propelling thrust with f being a prescribed function of time. Hence, loss of contact occurs if the interaction force becomes zero. The force N can be obtained by taking the inner product of (9) with $\boldsymbol{n}$ and is given by

$$N=[M\boldsymbol{g}-M\boldsymbol{a}_M]\cdot\boldsymbol{n}|_{s=\bar{s}(t)}. \tag{10}$$

To determine the axial force T, one substitutes (6b), (6c), and (8)–(10) into (6a) and assumes that the variation of axial force remains continuous at the mass. The axial force T can be obtained by taking the inner product of (6a) by the unit vector $\boldsymbol{i}$ and integrating it from 0 to $s=\bar{s}(t)$ and $s=\bar{s}(t)$ to ℓ and

using (7b). Inserting this result into (6a) in the $\boldsymbol{j}$ direction and neglecting nonlinear terms when compare these terms to the linear term of $v(s,t)$ and unity, the equation of motion of the nonhomogeneous beam with a riding mass is given by

$$m_r(\hat{m}_0+\hat{m}_{pq})\,v_{,tt}+E_rI\,(\hat{E}_{10}+\hat{E}^t_{1jk})\,v_{,ssss}+\boldsymbol{f}\cdot\boldsymbol{j}=0,\quad 0<s<\ell,\ t>0. \tag{11}$$

The differential equation is linear in the displacement field. Let the variable $v(s,t)$ be of the form

$$v(s,t)=\sum_{j=1}^{n}\tilde{q}_j(s)\,\tilde{h}_j(t)\equiv\tilde{\boldsymbol{q}}(s)^T\,\tilde{\boldsymbol{h}}(t), \tag{12}$$

where $\tilde{\boldsymbol{h}}(t)$ is the time dependent vector to be determined; n is a suitably large number to assure convergence. In order that the variable $v(s,t)$ satisfies the boundary condition given by (7a), one represents $\tilde{\boldsymbol{q}}(s)$ as a vector of a continuous function:

$$\tilde{\boldsymbol{q}}(s)=\left(\sin\frac{\pi s}{\ell},\sin\frac{2\pi s}{\ell},\ldots,\sin\frac{i\pi s}{\ell},\ldots,\sin\frac{n\pi s}{\ell}\right)^T,\quad 0<s<\ell, \tag{13}$$

which satisfies the spatial boundary constraints $\tilde{\boldsymbol{q}}|_{s=0,\ell}=\frac{\mathrm{d}^2\tilde{\boldsymbol{q}}}{\mathrm{d}s^2}|_{s=0,\ell}=\boldsymbol{0}$.

To obtain the normalized equations of motion of the combined system, one substitutes (8)–(10), (12), and (13) into (11) and introduces the following nondimensional quantities:

$$\tau=\sqrt{\frac{E_rI}{m_r\ell^4}}\,t,\quad \hat{M}=\frac{M}{m_r\ell},\quad \hat{N}=\frac{m_r\ell^3}{ME_rI}N,\quad \hat{f}=\frac{m_r\ell^3}{E_rI}f,\quad \hat{g}=\frac{m_r\ell^3}{E_rI}g,\quad \eta=\frac{s}{\ell},\quad \xi=\frac{\bar{s}}{\ell}. \tag{14}$$

To eliminate spatial dependence of (11), the Galerkin's procedure is employed and is done by multiplying (11) by the weighting vector $\boldsymbol{q}(\eta)$ and integrating (11) w.r.t. to η from 0 to 1. The result yields

$$\left(\boldsymbol{I}+\frac{2\hat{M}}{\hat{m}_0+\hat{m}_{pq}}\boldsymbol{G}_1\right)\ddot{\boldsymbol{h}}+\frac{4\hat{M}}{\hat{m}_0+\hat{m}_{pq}}\dot{\xi}\boldsymbol{G}_2\dot{\boldsymbol{h}}+\left[\frac{\hat{E}_{10}+\hat{E}^t_{1jk}}{\hat{m}_0+\hat{m}_{pq}}\boldsymbol{\Omega}_h^2+\frac{2\hat{M}}{\hat{m}_0+\hat{m}_{pq}}(-\hat{f}\boldsymbol{G}_2-\dot{\xi}^2\boldsymbol{G}_3)\right]\boldsymbol{h}$$
$$+\frac{2\hat{M}}{\hat{m}_0+\hat{m}_{pq}}\ddot{\xi}\boldsymbol{G}_2\boldsymbol{h}=\frac{2\hat{M}\hat{g}}{\hat{m}_0+\hat{m}_{pq}}\boldsymbol{s}_\xi,\quad 0<\xi<1,\ \tau>0, \tag{15a}$$

where the superposed prime and dot denoting the η and τ differentiation, $\boldsymbol{I}=n\times n$ unit matrix, $\boldsymbol{q}=\boldsymbol{q}(\eta)$, $\boldsymbol{h}=\boldsymbol{h}(\tau)$, $\boldsymbol{s}_\xi=s_{\xi j}$ with $s_{\xi j}=\sin j\pi\xi$ when $j=1,2,\ldots,n$; $\boldsymbol{G}_1=\int_0^1\delta(\eta-\xi)\boldsymbol{q}\boldsymbol{q}^Td\eta$, $\boldsymbol{G}_2=\int_0^1\delta(\eta-\xi)\boldsymbol{q}\boldsymbol{q}'^Td\eta$, $\boldsymbol{G}_3=\int_0^1\delta(\eta-\xi)\boldsymbol{q}\boldsymbol{q}''^Td\eta$, $\boldsymbol{\Omega}_h^2=2\int_0^1\boldsymbol{q}\boldsymbol{q}''''^Td\eta=\mathrm{diag}[(\omega_j^h)^2]$ with $\omega_j^h=(j\pi)^2$ being the normalized frequency of the j-th mode vibration of the homogeneous beam. Equations (9) and (10) become

$$\ddot{\xi}-\mu\boldsymbol{q}''^T\boldsymbol{h}(\dot{\xi})^2-2\mu\boldsymbol{q}'^T\dot{\boldsymbol{h}}\dot{\xi}-\mu\boldsymbol{q}^T\ddot{\boldsymbol{h}}-\hat{g}\boldsymbol{q}'^T\boldsymbol{h}=\hat{f}-\mu\hat{g},\quad \eta=\xi,\ \tau>0, \tag{15b}$$

$$\hat{N}=\hat{g}-[\boldsymbol{q}^T\ddot{\boldsymbol{h}}_1-2\boldsymbol{q}'^T\dot{\boldsymbol{h}}_1\dot{\xi}-\boldsymbol{q}''^T\boldsymbol{h}_1\dot{\xi}^2],\quad \eta=\xi,\ \tau>0. \tag{15c}$$

The initial conditions are

$$\dot{\xi}(0)=\dot{\xi}_0,\quad \xi(0)=\xi_0,\quad \boldsymbol{h}(0)=\dot{\boldsymbol{h}}(0)=\boldsymbol{0}, \tag{16}$$

where $\mathbf{0}$ is $n \times 1$ zero vector; $\dot{\xi}_0$ and ξ_0 are the initial speed and the initial position of mass on the beam, respectively. As shown in (15a), by properly arranging the material and geometric properties of periodic arrays, the beam frequency is able to be varied. In other words, the proposed beam has the potential to change its natural frequency to avoid the growth of small amplitude vibration and the occurrence of resonance. It is mentioned here that (15b) was obtained by eliminating the normal reaction force N of the beam on the mass between the two equations in directions $\boldsymbol{i}$ and $\boldsymbol{j}$ of (9).

After the mass left the beam, the dynamics of the system becomes the free vibration of the nonhomogeneous beam with nonzero initial conditions. In this situation, (15b) and (15c) vanish and (15a) reduces to

$$\ddot{\boldsymbol{h}} + \frac{\hat{E}_{10} + \hat{E}^t_{1jk}}{\hat{m}_0 + \hat{m}_{pq}} \boldsymbol{\Omega}_h^2 \boldsymbol{h} = \mathbf{0}, \quad \tau > \tau|_{\xi=1}, \tag{17a}$$

with the initial conditions

$$\boldsymbol{h}(0) = \boldsymbol{h}(\tau|_{\xi=1}) \quad \text{and} \quad \dot{\boldsymbol{h}}(0) = \dot{\boldsymbol{h}}(\tau|_{\xi=1}), \tag{17b}$$

where $\boldsymbol{h}(\tau|_{\xi=1})$ and $\dot{\boldsymbol{h}}(\tau|_{\xi=1})$ denote the amplitude and velocity of response of the beam when the mass is at the right end.

To verify the existence of solution of the system, a new state vector $\boldsymbol{z}$ is introduced into (15a) and (15b) to form the integrational scheme. Let $\boldsymbol{z} = (\dot{\boldsymbol{h}}^T, \dot{\xi}, \boldsymbol{h}^T, \xi)^T$ be a $2n+2$ vector with the associated initial condition $\boldsymbol{z}(0) = (\mathbf{0}^T, \dot{\xi}_0, \mathbf{0}^T, 0)^T$. The two equations can be written as

$$\boldsymbol{A}\dot{\boldsymbol{z}} + \boldsymbol{B}\boldsymbol{z} + \boldsymbol{p} = \mathbf{0}. \tag{18}$$

In (18), $\boldsymbol{A}$ and $\boldsymbol{B}$ are $(2n+2) \times (2n+2)$ matrices and $\boldsymbol{p}$ is the $(2n+2)$ vector defined by

$$\boldsymbol{A} = \begin{bmatrix} [\boldsymbol{I} + \frac{2\hat{M}}{\hat{m}_0+\hat{m}_{pq}} \boldsymbol{G}_1] & \frac{2\hat{M}}{\hat{m}_0+\hat{m}_{pq}} (\boldsymbol{G}_2 \boldsymbol{h}) & [\mathbf{0}] & \mathbf{0} \\ -\mu \boldsymbol{q}^T & 1 & \mathbf{0}^T & 0 \\ [\mathbf{0}] & \mathbf{0} & \boldsymbol{I} & \mathbf{0} \\ \mathbf{0}^T & 0 & \mathbf{0}^T & 1 \end{bmatrix},$$

$$\boldsymbol{B} = \begin{bmatrix} [\frac{4\hat{M}}{\hat{m}_0+\hat{m}_{pq}} \dot{\xi} \boldsymbol{G}_2] & \mathbf{0} & [\frac{\hat{E}_{10}+\hat{E}^t_{1jk}}{\hat{m}_0+\hat{m}_{pq}} \boldsymbol{\Omega}_h^2 + \frac{2\hat{M}}{\hat{m}_0+\hat{m}_{pq}} (-\bar{f}\boldsymbol{G}_2 + \dot{\xi}^2 \boldsymbol{G}_3)] & \mathbf{0} \\ \mathbf{0}^T & -\mu(\dot{\xi}\boldsymbol{q}''^T \boldsymbol{h} + 2\boldsymbol{q}'^T \dot{\boldsymbol{h}}) & -\hat{g}\boldsymbol{q}'^T & 0 \\ -\boldsymbol{I} & \mathbf{0} & [\mathbf{0}] & \mathbf{0} \\ \mathbf{0}^T & -1 & \mathbf{0}^T & 0 \end{bmatrix},$$

$$\boldsymbol{p} = \left(-\frac{2\hat{M}\hat{g}}{\hat{m}_0+\hat{m}_{pq}} \boldsymbol{s}_{\xi,}^T - (\hat{f} - \mu\hat{g}), \mathbf{0}^T, 0 \right)^T,$$

where $\boldsymbol{A}$ is a nonsingular matrix and $[\mathbf{0}]$ is a $n \times n$ zero matrix.

3. Numerical results and discussions

Numerical results refer to an assumed model wherein a mass travels with variable speed on a finite simply supported beam having transversely periodic arrays. To study the influence produced by the variation of various parameters to the dynamics of the system, the Runge–Kutta method with sixth order accuracy

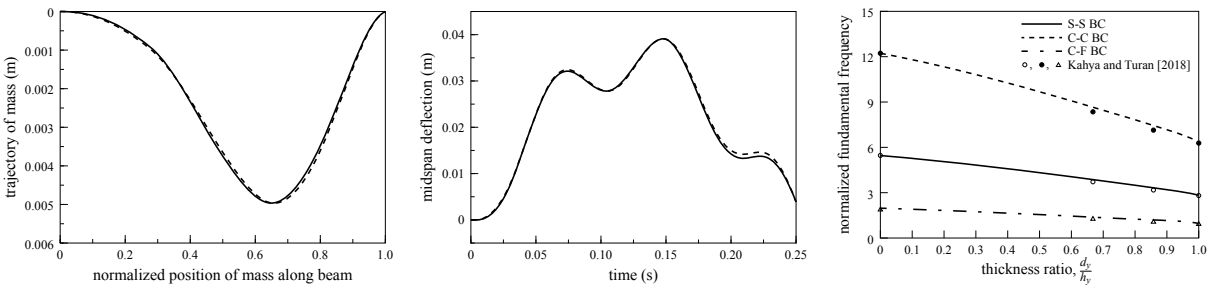

Figure 3. Comparison of the results with those reported in [Mohebpour et al. 2016] (dashed line, left), [Tao et al. 2016] (dashed line, middle), and [Kahya and Turan 2018] (symbolized by point symbols ◯, •, and Δ, right).

is employed to numerically integrate (18). The number of terms of the Fourier series in (1) and (2) is set to be 30 to assure convergence. The convergence of the model is tested by increasing the terms of approximation. It shows that for $n \geq 10$, the difference among the results is negligible. Hence, the dimension n of $\boldsymbol{z}$ is set to be 15 to retain for sufficient accuracy.

To validate the accuracy of the model, in agreement with previous works is considered. As shown in Figure 3, the accuracy of the model is verified by numerically integrating (18) and then the solutions (solid lines) of this study are compared with the results (dashed lines) reported in Figure 3 by Mohebpour et al. [2016] and in the Figure 2 by Tao et al. [2016]. The parameters selected are the same as those used in the two papers, respectively, and are given in Table 1. Note that in [Tao et al. 2016], the massless point force was used; under such condition, (18) reduces to $\dot{\boldsymbol{z}} + \boldsymbol{B}\boldsymbol{z} + \boldsymbol{p} = \boldsymbol{0}$, where

$$\boldsymbol{z} = (\dot{\boldsymbol{h}}^T, \boldsymbol{h}^T)^T, \quad \boldsymbol{B} = \begin{bmatrix} [\boldsymbol{0}] & [\frac{\hat{E}_{10}+\hat{E}^t_{1jk}}{\hat{m}_0+\hat{m}_{pq}}\,\boldsymbol{\Omega}_h^2] \\ -\boldsymbol{I} & [\boldsymbol{0}] \end{bmatrix}, \quad \boldsymbol{p} = \left(-\frac{2\hat{P}}{\hat{m}_0+\hat{m}_{pq}}\,\boldsymbol{s}_\xi^T, \boldsymbol{0}^T \right)^T, \quad \text{and} \quad \hat{P} = \frac{\ell^2}{E_r I}\,P,$$

with P being the massless point force. As shown in Figure 3 (left and middle), the solutions derived from the proposed model nearly coincide with the results obtained by Mohebpour et al. [2016] and Tao et al. [2016].

In addition to the verification mentioned above, the normalized fundamental frequency ($\equiv \omega_1$) of the proposed beam under simply-supported boundary condition is checked and compares it with the first nondimensional frequency ($\equiv \varpi_1$) reported in the Table 3 by [Kahya and Turan 2018]. The relation

[Mohebpour et al. 2016]	Stiffness $E = 2020.797216 \cdot 10^8$ Pa, density $\rho = 15267.2\,\mathrm{kg/m^3}$, length $\ell = 4.352$ m, thickness $H = 0.072322$ m, width $W = 0.018113$ m Mass of the traveling mass $m = 21.8$ kg, mass speed $v = 27.49$ m/s
[Tao et al. 2016]	Stiffness $E = 72.4$ GPa, density $\rho = 2770\,\mathrm{kg/m^3}$, length $\ell = 10$ m, thickness $H = 0.5$ m, width $W = 0.4$ m Magnitude of the point force $P = 500$ kN, force speed $v = 40$ m/s

Table 1. The properties of the beams and moving masses used in [Mohebpour et al. 2016] and [Tao et al. 2016].

$k=0$	$\hat{d}_y = 0$ (a homogeneous ceramic beam)
$k=1$	$\hat{d}_y = 0.67$ ($d_y = 0.5t_m$ and $h_y = 0.75t_m = 1.5t_c$), t_c, t_m = the thickness of one ceramic lamina and metal core, respectively
$k=2$	$\hat{d}_y = 0.857$ ($d_y = 0.5t_m$ and $h_y = 0.583t_m = 3.5t_c$)
$k=10$	$\hat{d}_y \approx 1$ (a beam with almost all metal material)

Table 2. The relations between k and the parameters used in Figure 3 (right).

Set 1	The Young's moduli (GPa) of the strips of a, b, and the material c of the basic layer $E_a = 205$ ($\hat{E}_a = 2.05$), $E_b = 142$ ($\hat{E}_b = 1.42$), $E_c = 100$ ($\hat{E}_c = 1$)
	The densities (10^3 kg/m^3) of the strips of a, b, and the material c of the basic layer $\rho_a = 7.7$ ($\hat{\rho}_a = 1.1$), $\rho_b = 1.6$ ($\hat{\rho}_b = 0.229$), $\rho_c = 7$ ($\hat{\rho}_c = 1$)
Set 2	$E_a = 250$ ($\hat{E}_a = 2.5$), $E_b = 175$ ($\hat{E}_b = 1.75$), $E_c = 100$ ($\hat{E}_c = 1$) $\rho_a = 3.5$ ($\hat{\rho}_a = 0.5$), $\rho_b = 5.25$ ($\hat{\rho}_b = 0.75$), $\rho_c = 7$ ($\hat{\rho}_c = 1$)

Table 3. The material properties of the proposed beam for set 1 and set 2.

between these two frequencies ϖ_1 and ω_1 is $\varpi = (\ell/Hs)\omega_1$, where s denotes the slenderness ratio s. For a beam having rectangular cross-section area with height H, the slenderness ratio s equals $\sqrt{12}\,\ell/H$ and hence

$$\varpi_1 = \frac{\omega_1^h}{\sqrt{12}}\sqrt{\frac{\hat{E}_{10} + \hat{E}^t_{1jk}}{\hat{m}_0 + \hat{m}_{pq}}}.$$

Therefore, with the same materials as those used in [Kahya and Turan 2018], the frequency ω_1 varies from 2.849 ($\varpi_1 = 2.8057$), where $\omega_1 = \omega_1^h/\sqrt{12} = 2.849$ ($\omega_1^h = \pi^2$, [Han et al. 1999]), to 5.483 ($\varpi_1 = 5.4658$). The frequency of the proposed beam under other kinds of boundary conditions can be obtained by similar ways. For example, the frequency ω_1 for clamped-clamped BC is from 6.458 ($\varpi_1 = 6.302$), where $6.458 = \omega_1 = \omega_1^h/\sqrt{12}$ ($\omega_1^h = (4.73)^2$, [Han et al. 1999]), to 12.42 ($\varpi_1 = 12.235$). Figure 3 (right) shows the frequency ω_1 of the proposed beam versus the thickness ratio $\hat{d}_y$ under different boundary conditions and the results reported in the Table 3 by [Kahya and Turan 2018] (symbolized by point symbols ◯, •, and Δ) where the face-core-face thickness ratio 1-0-1 is chosen and the power-law exponent k selected are $k = 0$, 1, 2, and 10. In this figure, the FG beam is modeled as a sandwich beam composed of one metal core and two ceramic face layers. The solid, dashed, and central lines shown denote the results of this study under the simply-supported, clamped-clamped, and clamped-free boundary conditions, respectively. The relation between the power-law exponent k and the parameters used in Figure 3 (right) is given in Table 2. It clearly indicates that the solutions derived from the proposed model are in agreement with the results obtained by Kahya and Turan [2018].

To parametric study the dynamics of a mass traveling on the periodic-array beam, two sets of parameters are chosen and given in Table 3. The difference between the two sets is different arrangements of material properties. The numerical order of the Young's moduli and densities of materials selected in set 1 and set 2 is $E_a > E_b > E_c$, $\rho_a > \rho_c > \rho_b$ and $E_a > E_b > E_c$, $\rho_c > \rho_b > \rho_a$, respectively.

The geometric properties of the beam are: $\ell = 10\,\text{m}$ and $W = H = 0.15\,\text{m}$, where the slenderness ratio $s = \ell(\sqrt{I/A})^{-1} = \sqrt{12}\,\ell/H = 231$. The traveling mass has the mass $M = 200\,\text{kg}$. Note that in the following figures, unless otherwise specified, the dashed line without symbol denotes the beam is a homogeneous beam having the material c. Meanwhile, in Figures 4–8, the mass moves at constant speed $\dot{\bar{s}}(t) = 20\,\text{m/s}$. With the view to illustrating the diversity of the proposed model, firstly the dynamics of a sandwich beam (having three horizontal layers) with a riding mass is considered and presented in Figures 4 and 5; the parameter set 1 is chosen. The beam consists of one embedded and two basic laminas; the core layer consists of three and two strips of a and b, respectively. The h_z and h_y are given by $h_z = 0.15/(4 + 2\hat{d}_z)$, $0 < \hat{d}_z < 1$, and $h_y = 0.15/(4 - 2\hat{d}_y)$, $0 < \hat{d}_y < 1$.

Figure 4 presents the trajectory of mass (mm) versus the position of mass along the beam (m) and the time history (s) of the midpoint deflection (mm) of the beam, respectively. The thickness ratios $\hat{d}_y$ and $\hat{d}_z$ are $\hat{d}_y = 0.25$ and $\hat{d}_z = 0.1$ (symbolized by $+$), 0.5 (symbolized by $\square$), and 0.9 (symbolized by Δ). Figure 5 presents similar information to that shown in Figure 4, except $\hat{d}_z = 0.25$ and three different values of $\hat{d}_y$ being selected, $\hat{d}_y = 0.1$ (symbolized by $+$), 0.5 (symbolized by $\square$), and 0.9 (symbolized by Δ). These two figures clearly indicate that different arrangements of the geometric and material properties of the arrays bring different capabilities of the beam to reduce the amplitude of vibration, even after the mass left the terminal point. Figure 4 also indicates that the strip a having the largest density, increasing $\hat{d}_z$ increases not only the stiffness but also the mass of the embedded lamina; this causes that changing $\hat{d}_z$ makes a little difference to reduce the amplitude of beam vibration. For the thickness ratio $\hat{d}_y$, since the embedded layer has greater specific stiffness than the basic layer, as shown in Figure 5, increasing $\hat{d}_y$ has significant potentials to diminish the vibration of the system.

To study the impact arising from different arrangements of the moduli of the arrays, in Figure 6, the midpoint deflection of the beam (mm) is plotted as a function of the variation of $\hat{d}_z$ (Figure 6, left) and $\hat{d}_y$ (Figure 6, right) when the mass reaches the midpoint ($\xi = 0.5$). The parameter set 1 and the beam having horizontally three embedded and four basic laminas are chosen. The embedded layer consists of three and four strips of a and b, respectively. The periods h_z and h_y are $h_z = 0.15/(8 - 2\hat{d}_z)$ $(0 < \hat{d}_z < 1)$ and $h_y = 0.15/(8 - 2\hat{d}_y)$ $(0 < \hat{d}_y < 1)$. In Figure 6 (left), $\hat{d}_y$ selected are: 0 (dashed line, case (4)), 0.1 (symbolized by $+$), 0.25 (symbolized by $\square$), 0.5 (symbolized by Δ), 0.75 (symbolized by $\bigcirc$), and 1 (symbolized by $\oplus$, cases (5, 6, 7)). In Figure 6 (right), $\hat{d}_z$ used are: 0 (without symbol), 0.1 (symbolized by $+$, cases (2, 6)), 0.25 (symbolized by $\square$), 0.5 (symbolized by Δ), 0.75 (symbolized by $\bigcirc$), and 1.0 (symbolized by $\oplus$, cases (3, 7)). This figure clearly shows that if the embedded lamina has higher specific stiffness than the basic layer, the integration of embedded laminas into the beam increases the capability of the beam to diminish the vibration caused by the motion of riding mass. However, in set 1, the strips of a and b have the largest and lowest densities, respectively. Hence, when $\hat{d}_z$ increases from 0 to 1, the Young's modulus ratio is from $\hat{E}_b = 1.42$ to $\hat{E}_a = 2.05$ and the density ratio is from $\hat{\rho}_b = 0.229$ to $\hat{\rho}_a = 1.1$. In other words, the increase of $\hat{d}_y$ and $\hat{d}_z$ increases not only the stiffness but also the mass of the beam. This implies when $\hat{d}_y$ becomes large, the increase of density becomes greater than that of the Young's modulus such that greater $\hat{d}_z$ has lower potential to reduce the vibration than smaller $\hat{d}_z$.

In order to fully understand the influence produced by the change of the beam properties, the set 2 ($E_a > E_b > E_c$ and $\rho_c > \rho_b > \rho_a$) is chosen. The speed and mass of the moving mass are the same as before. Figure 7 presents similar information to that shown in Figure 6. This figure indicates that when

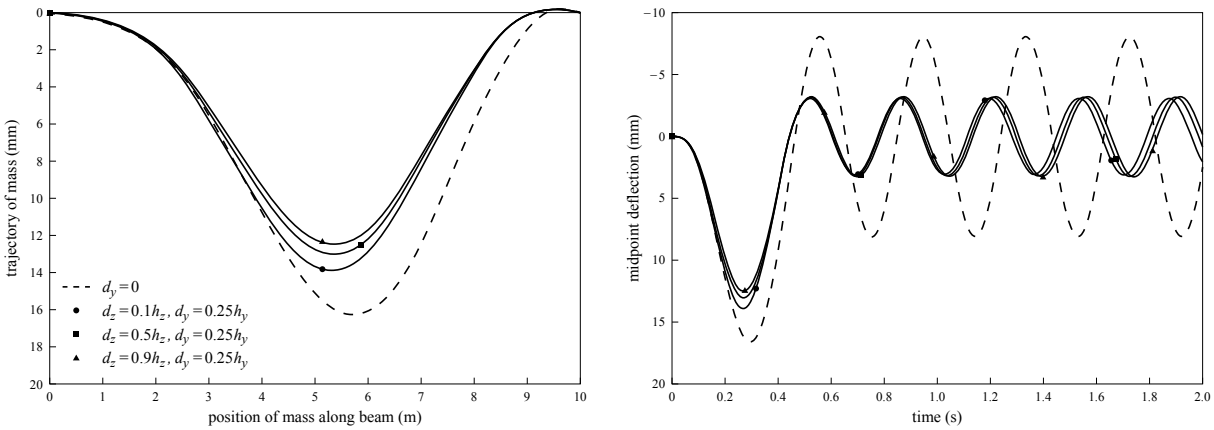

Figure 4. Trajectory of mass (mm) versus the position of mass along the beam (m) (left) and the time history (s) of the midpoint deflection (mm) of the beam (right).

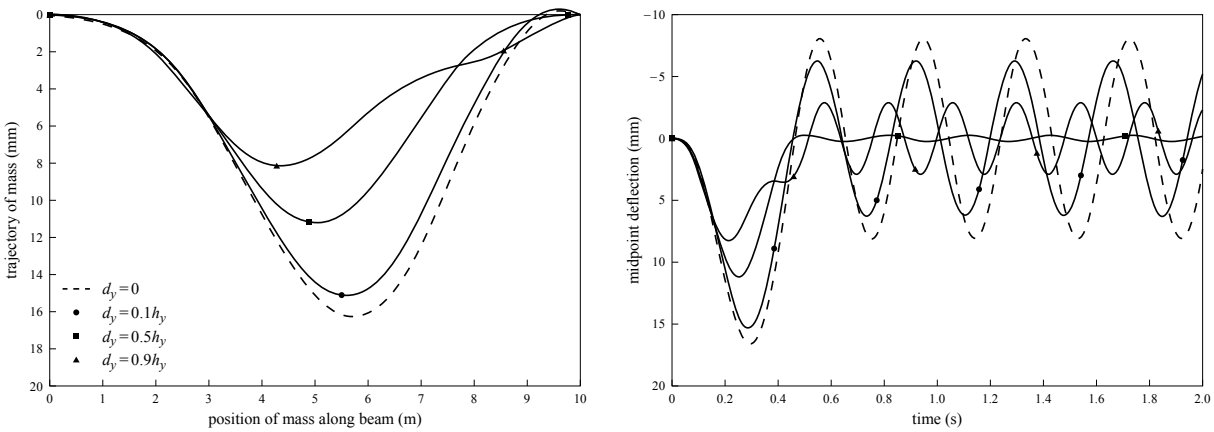

Figure 5. This figure presents similar information to that shown in Figure 4, except that the thickness ratios used are different with those shown in Figure 4.

the basic layer has lowest Young's modulus and largest density, increasing the thickness ratios $\hat{d}_y$ and $\hat{d}_z$ amplifies the capability of the beam to reduce the vibration of the system. However, if this is not the case, e.g., as those shown in Figure 6, large $\hat{d}_z$ may not have higher potential to diminish the amplitude of vibration than small $\hat{d}_z$. From Figures 6 and 7, one may conclude that the capability of the beam to diminish the vibration of the system increases with the stiffness ratio, but decreases with the density ratio, between the embedded and the basic layers.

Figure 8 presents the effects produced by the change of the number of strips and layers of the beam for set 1 (shown in dashed lines) and set 2 (shown in solid lines). In this figure, the beam deflection at mid-span when the mass reaches $\xi = 0.5$ is plotted as a function of the total of strips (Figure 8, left) and layers (Figure 8, right). In Figure 8 (left), two different beams are considered, a sandwich (symbolized by $+$) and a five-layer (symbolized by Δ) beams. The sandwich beam consists of one

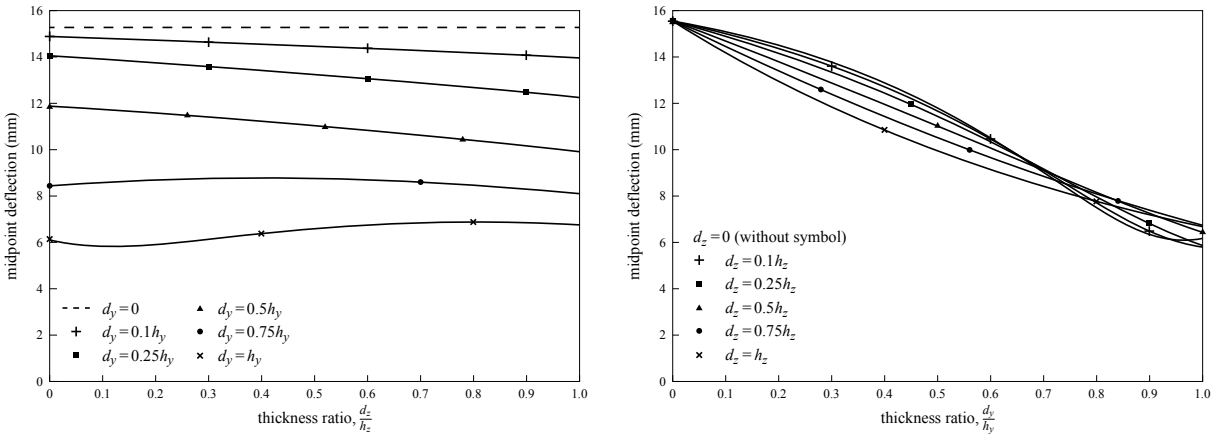

Figure 6. The midpoint deflection of the beam (mm) when the mass reaches the midpoint ($\xi = 0.5$) versus the variation of the thickness ratios $\hat{d}_z$ (left) and $\hat{d}_y$ (right).

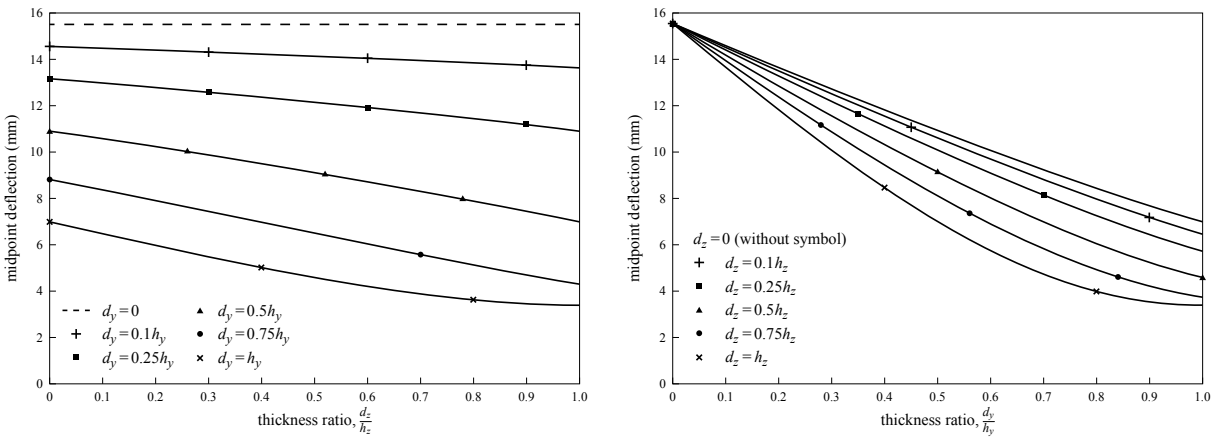

Figure 7. This figure presents similar information to that shown in Figure 6, except the set 2 being selected.

embedded and two basic layers; the five-layer beam is composed of three embedded and two basic layers. Both of the thickness ratios $\hat{d}_y$ and $\hat{d}_z$ are set to be 0.5. In Figure 8 (right), the number of strips of an embedded lamina chosen are 3 (symbolized by $+$) and 9 (symbolized by Δ). The two plots indicate that the difference due to different numbers of strips and layers converges quickly. Recalling that the increase of the number of strips and layers decreases the distance of the periods h_z and h_y, respectively. Therefore, for example, when the beam has a many of layers, the length of h_y becomes a tiny value and the terms $\hat{h}_y$ and $\hat{I}_y$ approach to zero such that $\hat{m}_{pq} \to \sum_{p=1}^{\infty} \hat{m}_p$ and $\hat{E}^t_{1jk} \to \sum_{j=1}^{\infty} \hat{E}_{1j}$ ((3) and (4b)). Similar phenomenon is also observed when $h_z(\hat{h}_z)$ is examined. This means that the midpoint deflection converges to a specific value as the number of strips and layers increases. From Figures 6–8, one concludes that with proper choice of the stiffness ratio, density ratio, and thickness ratio between the embedded and basic laminas of the beam, the growth of small amplitude vibration into large motion

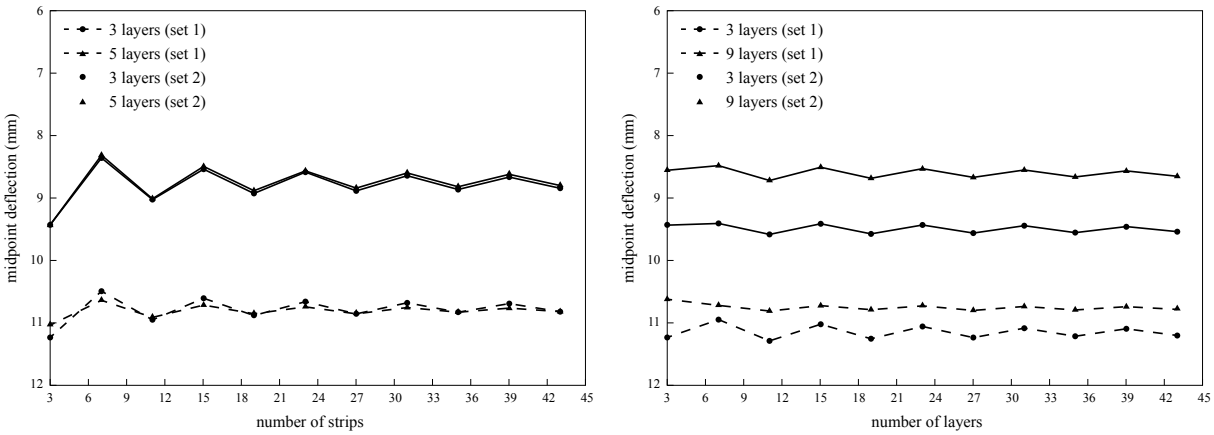

Figure 8. This figure shows the beam deflection at mid-span when the mass reaches $\xi = 0.5$ versus the number of strips of the embedded lamina (left) and the total of layers of the beam (right).

regime can be attenuated. In other words, because of inhomogeneity of materials, when structures are subjected to external excitations, structures have the ability to prolong their useful life by adjusting the arrangement of material and geometric properties between the embedded periodic-array and basic layers.

In the following, the mass slows down during operation being taken into account. Figure 9 illustrates the trajectory of mass (mm) versus the position of mass along a sandwich beam for different arrangements of periodic arrays and sets of parameters. The embedded lamina consists of three and two strips of a and b, respectively. The dashed and solid lines denote the set 1 and set 2, respectively. The thickness ratios $\hat{d}_y$ and $\hat{d}_z$ selected are: $\hat{d}_y = \hat{d}_z = 0$ (dashed line, without symbol), $\hat{d}_y = \hat{d}_z = 0.5$ (symbolized by $+$), $\hat{d}_y = 1$ and $\hat{d}_z = 0.5$ (symbolized by $\square$). In Figure 9 (left), the mass travels at constant speed, $v = 20\,\mathrm{m/s}$. In Figure 9 (right), the mass is under deceleration for $v_0 = 20\,\mathrm{m/s}$ (initial speed), $\mu = 0$ (zero friction), and $f = -20\,\mathrm{m/s}^2$ (the retard force applied on the mass). Figure 10 presents similar information to that shown in Figure 9 (right), except that the mass stops before the end support being considered. The initial speed and retard force applied on the mass are, respectively, $v_0 = 20\,\mathrm{m/s}$ and $f = -22\,\mathrm{m/s}^2$. The frictions used in Figure 10 (left) and Figure 10 (right) are $\mu = 0$ and $\mu = 0.5$, respectively. Note that the friction is served as another braking system and therefore it may not be a small value. These two figures clearly disclose that the periodic-array composite beam noticeably diminishes the amplitude of the trajectory of mass. Meanwhile, Figure 10 shows that as the mass is slowing down and stops prior to the terminal point, acute oscillation of the trace of mass occurs. In addition, when the mass is subjected to large reverse forces and friction force, the mass may stop away from the end support; under such situation, as the mass moves along a homogeneous beam (showing as dashed line without symbol) and is near the halt point, the oscillating amplitude of the trajectory of mass may become large. This condition can be avoided if the proposed beam is employed.

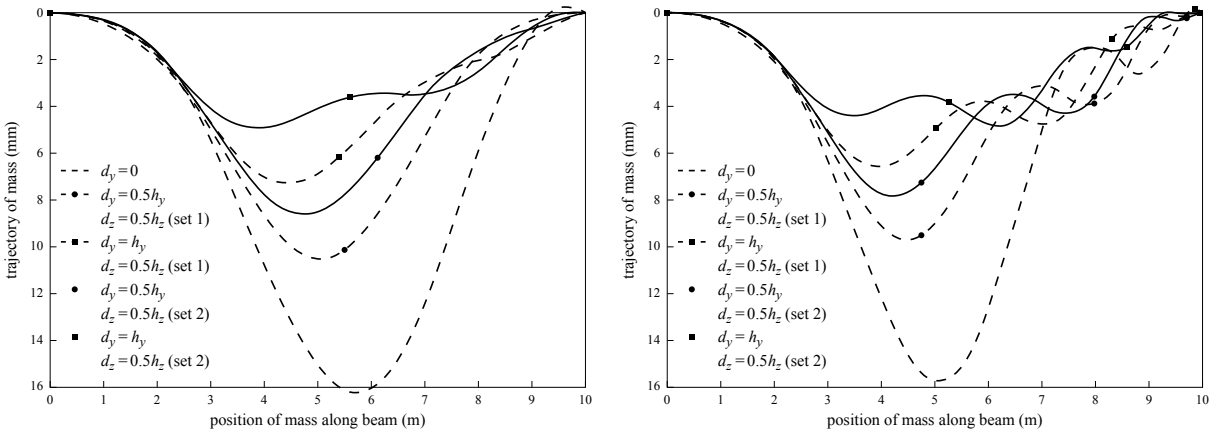

Figure 9. This figure illustrates the trajectory of mass (mm) versus the position of mass along the sandwich beam for different arrangements of periodic arrays. Left: the mass travels at constant speed. Right: the mass is under deceleration.

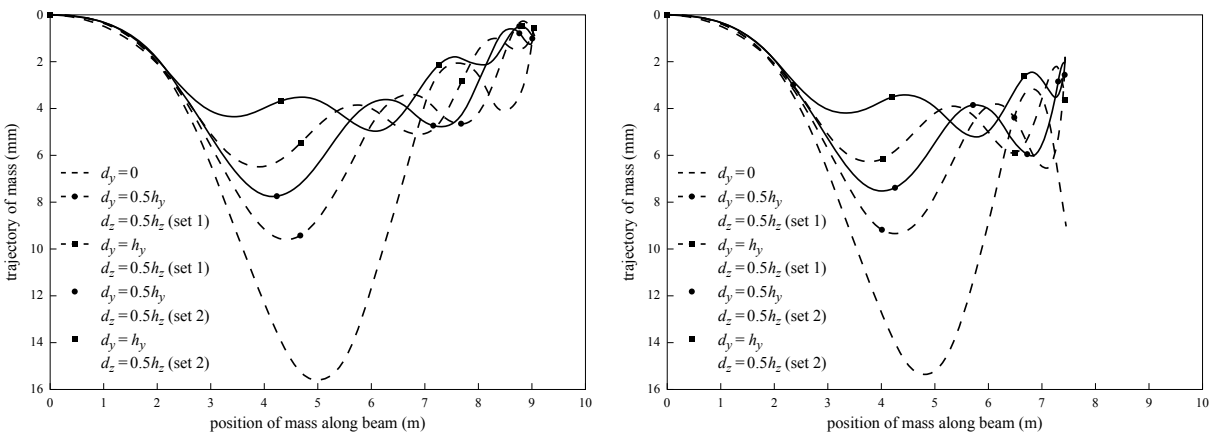

Figure 10. This figure presents similar information to that shown in Figure 9 except that the mass stops before the end terminal being considered with frictions $\mu = 0$ (left) and $\mu = 0.5$ (right).

4. Conclusions

In this study, nonhomogeneous beams having transversely periodic arrays and different arrangements of materials and laminas are considered. The Fourier series with a wavelength equal to the average space between two different strips and a wavelength equivalent to the average space between embedded and basic layers are used to take into account the periodicity of the embedded lamina and beam, respectively. The Young's modulus and density of the composite beam are biaxial periodic functions. The proposed passive nonhomogeneous beam is introduced to a beam-mass system to attenuate the likelihood of large-amplitude vibrations.

Results show that even if the material damping is not considered, the proposed beam has excellent capability to reduce the vibration of a beam-mass system after the mass left the beam. Different arrangements of material and geometric properties of the periodic arrays result in different bending stiffness and mass distribution of the beam. The vibration of the system can be effectively attenuated by properly choosing the stiffness and density ratios between the embedded strips/laminas and basic layers. It indicates that the bending frequency of the nonhomogeneous beam varies with the change of mass ratio, Young's modulus ratio, and thickness ratio of the periodic arrays; this is not observed when a homogeneous beam is taken into account. In addition, the proposed model may be applied to many applications if proper materials are selected. For example, if the shape-memory-alloy (SMA) is used to replace the strip a, the beam is capable of having the ability to overcome the influence produced by the change of temperature.

Acknowledgements

The authors wish to express their sincere appreciation to the reviewers for their valuable comments.

Table of notations

H: height of the beam (gravitational (y) direction)

W: width of the beam (horizontal (z) direction)

I: the area moment of inertia of the beam

$\widetilde{M}$: the resultant bending moment about the neutral axis of the cross-section of the beam at time t

M, $\widehat{M}$: the mass and the dimensionless mass of the moving mass

N, $\widehat{N}$: the dimensional and nondimensional normal reaction force between the beam and the riding mass

T: the axial force in the beam

V: the transverse force in the beam

a, b, c: material symbols of the two different strips used in an embedded lamina and the basic layers, respectively

f: the thrust applied on the riding mass

m: mass per unit length of the beam

ℓ: length of the beam

E_a, E_b, E_c: the Young's moduli of the strips a, b, and the basic layer, respectively

E_1^z: the axial Young's modulus of an embedded lamina, a periodic function in z direction

$E_1(y, z)$: the axial Young's modulus of the nonhomogeneous beam, a biaxial periodic function in y and z directions

d_y, $\hat{d}_y$: one-half of the thickness of an embedded lamina and the thickness ratio of an embedded lamina being present in one period ($2h_y$) in the height direction, $\hat{d}_y = d_y/h_y$, respectively

d_z, $\hat{d}_z$: one-half of the thickness of the strip a and the thickness ratio of the strip a being present in one period ($2h_z$) in the width direction, $\hat{d}_z = d_z/h_z$, respectively

h_y, $\hat{h}_y$: one-half of the distance between the midpoint of two basic layers separated by one embedded lamina and the ratio of $2h_y$ to the height of the beam, $\hat{h}_y = 2h_y/H$, respectively

h_z, $\hat{h}_z$: one-half of the distance between the midpoint of two strips of b separated by one ply of a and the ratio of $2h_z$ to the width of the beam ($\hat{h}_z = 2h_z/W$), respectively

s, $\bar{s}$: the arc length and the position of the moving mass along the beam, respectively

u: the axial displacement of the beam measured from the undeformed state

v: the transverse displacement of the beam measured from the undeformed state

ρ_a, ρ_b, ρ_c: densities of the strips a, b, and the basic layer, respectively

ρ^z: density of an embedded lamina, which is a periodic function in z direction, $\rho^z = \rho^z(z)$

ρ: density of the nonhomogeneous beam, which is a biaxial periodic function in y and z directions, $\rho = \rho(y, z)$

$\boldsymbol{a}_M$: acceleration of the moving mass

$\boldsymbol{f}$: the external forces including the weight and the reactions of the moving mass upon the composite beam

$\boldsymbol{g}$: acceleration due to gravity ($= g\boldsymbol{j}$)

$\boldsymbol{I}$: the $n \times n$ unit matrix

$\boldsymbol{i}$: the unit vector in the horizontal direction

$\boldsymbol{j}$: the unit vector in the gravitational (transverse) direction

$\boldsymbol{n}$: the unit normal vector to the beam configuration

$\boldsymbol{r}$: the Cartesian position vector of point s along the beam at time t

$\hat{\boldsymbol{\tau}}$: the unit tangent vector to the beam configuration

μ: coefficient of friction

ξ: dimensionless position of the moving mass along the beam

ω_j^h: the normalized frequency of the j-th mode vibration of the homogeneous beam

$\bar{\delta}(s - \bar{s})$: Dirac delta function

δ_{rp}: Dirac delta symbol

References

[Şimşek 2010] M. Şimşek, "Vibration analysis of a functionally graded beam under a moving mass by using different beam theories", *Compos. Struct.* **92** (2010), 904–917.

[Şimşek and Kocatürk 2009] M. Şimşek and T. Kocatürk, "Free and forced vibration of a functionally graded beam subjected to a concentrated moving harmonic load", *Compos. Struct.* **90**:4 (2009), 465–473.

[Şimşek et al. 2012] M. Şimşek, T. Kocatürk, and Ş. D. Akbaş, "Dynamic behavior of an axially functionally graded beam under action of a moving harmonic load", *Compos. Struct.* **94**:8 (2012), 2358–2364.

[Friswell and Lees 2001] M. I. Friswell and A. W. Lees, "The modes of non-homogeneous damped beams", *J. Sound Vib.* **242**:2 (2001), 355–361.

[Han et al. 1999] S. M. Han, H. Benaroya, and T. Wei, "Dynamics of transversely vibrating beams using four engineering theories", *J. Sound Vib.* **225**:5 (1999), 935–988.

[Kahya and Turan 2018] V. Kahya and M. Turan, "Vibration and stability analysis of functionally graded sandwich beams by a multi-layer finite element", *Compos. B Eng.* **146** (2018), 198–212.

[Lee and Lee 2017] J. W. Lee and J. Y. Lee, "Free vibration analysis of functionally graded Bernoulli-Euler beams using an exact transfer matrix expression", *Int. J. Mech. Sci.* **122** (2017), 1–17.

[Li et al. 2008] J. Li, H. Hua, and R. Shen, "Dynamic stiffness analysis for free vibrations of axially loaded laminated composite beams", *Compos. Struct.* **84**:1 (2008), 87–98.

[Misiurek and Śniady 2013] K. Misiurek and P. Śniady, "Vibrations of sandwich beam due to a moving force", *Compos. Struct.* **104** (2013), 85–93.

[Mohebpour et al. 2016] S. R. Mohebpour, M. Vaghefi, and M. Ezzati, "Numerical analysis of an inclined cross-ply laminated composite beam subjected to moving mass with consideration the Coriolis and centrifugal forces", *Eur. J. Mech. A Solids* **59** (2016), 67–75.

[Rao et al. 2001] M. K. Rao, Y. M. Desai, and M. R. Chitnis, "Free vibrations of laminated beams using mixed theory", *Compos. Struct.* **52**:2 (2001), 149–160.

[Sayyad and Ghugal 2017] A. S. Sayyad and Y. M. Ghugal, "Bending, buckling and free vibration of laminated composite and sandwich beams: a critical review of literature", *Compos. Struct.* **171** (2017), 486–504.

[Sheng and Wang 2018] G. G. Sheng and X. Wang, "Nonlinear vibration of FG beams subjected to parametric and external excitations", *Eur. J. Mech. A Solids* **71** (2018), 224–234.

[Song et al. 2018] Q. Song, Z. Liu, J. Shi, and Y. Wan, "Parametric study of dynamic response of sandwich plate under moving loads", *Thin-Walled Struct.* **123** (2018), 82–99.

[Tao et al. 2016] C. Tao, Y.-M. Fu, and H.-L. Dai, "Nonlinear dynamic analysis of fiber metal laminated beams subjected to moving loads in thermal environment", *Compos. Struct.* **140** (2016), 410–416.

[Wang 2009] Y.-M. Wang, "The transient dynamics of a moving accelerating/decelerating mass traveling on a periodic-array non-homogeneous composite beam", *Eur. J. Mech. A Solids* **28** (2009), 827–840.

Received 23 Jun 2018. Revised 28 Jan 2019. Accepted 18 Apr 2019.

YI-MING WANG: wangym@cc.ncue.edu.tw
Department of Mechatronics Engineering, National Changhua University of Education, 2 Shih-Ta Road, Changhua 500, Taiwan

HUNG-CHIEH LIU: d0351005@mail.ncue.edu.tw
Department of Mechatronics Engineering, National Changhua University of Education, 2 Shih-Ta Road, Changhua 500, Taiwan

JOURNAL OF MECHANICS OF MATERIALS AND STRUCTURES
Vol. 14, No. 2, 2019
dx.doi.org/10.2140/jomms.2019.14.259

STRESS CONCENTRATION AROUND AN ARBITRARILY-SHAPED HOLE IN NONLINEAR FULLY COUPLED THERMOELECTRIC MATERIALS

CHUAN-BIN YU, HAI-BING YANG, KUN SONG AND CUN-FA GAO

Using the complex variable method, we study the plane problem of an infinite thermoelectric material containing an arbitrarily-shaped hole under a uniform remote electric current and a uniform energy flux. The nonlinear fully coupled thermoelectric constitutive equations are used to account for the large current or temperature gradient imposed on thermoelectric materials during their engineering service. The hole surface is assumed to be electrically and thermally insulated and mechanically free. The shape of the hole is defined by a polynomial conformal mapping. Fourier expansion technique is used to solve the corresponding boundary value problems. A triangular hole is considered for the purpose of illustration. The bluntness, hole orientation and the load angle as important parameters are considered. Numerical results show that the effects of these parameters on stress distribution around the hole are very significant. By the correct selection of these parameters, the lowest thermal stress concentration can be achieved.

1. Introduction

Thermoelectric materials are widely used in energy conversion: the Seebeck effect allows electricity generation from a temperature gradient, while the Peltier effect can convert electricity into cooling [Tritt and Subramanian 2006; Bell 2008; He et al. 2015; He and Tritt 2017]. Thermoelectric solids are typically brittle semiconductors with low mechanical strength and always subjected to defects and damages, for example, holes, voids and cracks, during their fabrication and operation [Schmidt et al. 2015; Li et al. 2015]. When the heat flux at a thermoelectric solid is disturbed by the geometric discontinuities brought by holes/imperfections, thermal stresses are induced. Excessive thermal stresses will cause the premature failure and thus reduce the useful life of thermoelectric structures and devices. Determining the amount and location of these stresses is essential to achieve accurate predict and evaluate the reliability of thermoelectric devices. Consequently, the research on the hole problem of thermoelectric materials is of great practical importance.

Thermal stress concentration around holes is one of the classical topics in solid mechanics. Ever since Florence and Goodier [1960] developed the basic theory of thermoelasticity in which complex variable method for stress analysis of perforated plate was used, the research on thermal stress concentration problem around holes is ongoing. For instance, using the complex variable theory, Chao and Wang [1993] predicted the failure initiation and crack trajectory for a plate weakened by an elliptic hole under thermal or mechanical load based on the strain energy density criterion. The Green's function for an infinite isotropic plate with an arbitrary-shaped hole under adiabatic and isothermal boundary conditions with a heat source was obtained by Yoshikawa and Hasebe [1999]. Based on Green's function method and the technique of conformal mapping, a unified solution for a thermopiezoelectric plate with holes

Keywords: thermoelectric materials, conformal mapping, series expansion, arbitrarily-shaped holes, thermal stress.

of various shapes was obtained analytically by Qin [1999; 2000]. Based on the extended version of Eshelby–Stroh's formulation, Gao et al. [2002] studied the generalized plane problem of an elliptical hole in a thermopiezoelectric medium subjected to uniform heat flow and mechanical-electrical loads at infinity according to exact boundary conditions at the rim of the hole. The two-dimensional thermoelastic problems for the perforated plates for different mechanical and thermal boundary conditions were fully investigated by Hasebe and Wang [2005]. The general solutions for the external force, displacement, and mixed boundary value problems under both the uniform heat flux and a point heat source were separately described. Thermoelastic solution to a coated elliptic hole embedded in an infinite plate under uniform heat flux was investigated by Chen and Chao [2008]. Hasebe and his coworkers analyzed the Joule heat, temperature and thermal stress induced by an electric current for a thin infinite conductor containing an elliptical hole, and the similar stress analysis was extended for magnetoelastic materials [Hasebe et al. 2009; Hasebe 2009]. With using the method of piece-wise homogeneous layers, the non-axisymmetric two-dimensional problem of thermal stresses in a functionally graded plate having radial arbitrary elastic properties with a circular hole under remote uniform heat flux is derived by Yang and Gao [2010]. Lekhnitskii's complex variable method was developed by Rasouli and Jafari to investigate the effect of uniform heat flux on a perforated anisotropic plate with an elliptical hole [Rasouli and Jafari 2016]. Additionally, Jafari et al. [2016] studied the effect of rotation angle and bluntness of hole on stress distribution around an arbitrary-shaped hole in an infinite isotropic plate based on the complex variable method and conformal mapping technique.

Many of the work done by the various researchers highlight the importance of thermal stress analysis around holes in thermoelasticity governing by linear equations. However, coupling among different physical phenomena makes the analysis in nonlinear media considerably more complicated. One such example is thermoelectricity, wherein the electric and heat transports are nonlinearly coupled. Up to present, the investigations on the hole problem in thermoelectric materials are restricted to holes with regular shape (circular and elliptical hole) due to the complicated nonlinear governing equations. For examples, Zhang and Wang investigated the elliptical hole problem in an infinite thermoelectric medium when electric current and energy flux loads are perpendicular to the major axis of the elliptical hole [Zhang and Wang 2016]. The plane problem of an inclined elliptic hole in an infinite thermoelectric material was studied by Wang and Wang [2017]. Pang et al. [2018] analyzed the temperature, heat flux and thermal stress induced by an electric current for a thin infinite thermoelectric medium containing a circular hole with an edge crack. To the best of our knowledge, no study has been completely conducted to evaluate the thermal stresses in a thermoelectric material containing a hole with irregular shapes. In fact, holes/imperfections of different shapes are made up due to practical reasons. Stresses concentration will occur at the contour of the hole and its analysis involves lot of complexity. In the present study, by using the complex variable method and conformal mapping technique [Muskhelishvili 1975], an attempt has been made to show the influence of key parameters such as rotation angle and bluntness on the thermal stress distribution around practical holes with various shapes.

2. Basic equations for thermoelectric materials

2.1. ***Governing quations.*** We consider a homogeneous and isotropic thermoelectric medium characterized by the electric conductivity δ, thermal conductivity κ and Seebeck coefficient ε. The constitutive

euqations governing the coupled transports of heat and electricity in such a material can be given by [Zhang and Wang 2016; Yang et al. 2013]

$$\boldsymbol{J} = -\delta\nabla\phi - \delta\varepsilon\nabla T = -\delta\nabla(\phi + \varepsilon T), \tag{1}$$

$$\boldsymbol{J}_q = -T\varepsilon\delta\nabla\phi - (T\varepsilon^2\delta + \kappa)\nabla T = \varepsilon T\boldsymbol{J} - \kappa\nabla T, \tag{2}$$

where ∇ is the Nabla operator, ϕ is the electric potential, T is the temperature, $\boldsymbol{J}$ and $\boldsymbol{J}_q$ are the electric current density vector and the thermal flux vector, respectively. Additionally, the thermoelectric equilibrium equations are expressed by

$$\nabla\cdot\boldsymbol{J} = 0, \qquad \nabla\cdot\boldsymbol{J}_u = 0, \tag{3}$$

where $\boldsymbol{J}_u$ is the energy flux vector defined as

$$\boldsymbol{J}_u = \boldsymbol{J}_q + \phi\boldsymbol{J}, \tag{4}$$

which indicates that the energy in the medium is transported by both electricity and heat. It is worth pointing out that the physical meaning of (3) is that both electric charges and energy are conserved in the considered material.

Obviously, the thermoelectric equations are nonlinear with fully coupled electric current and temperature. From (1), one can see that the Seebeck effect, which generates electric potential difference from temperature difference, will also produces electric current in the material. On the other hand, the electric current can cause extra heat flow in thermoelectric material in addition to the temperature gradient. The ratio of the generated extra heat flux to electric current is related to an intrinsic material property called Peltier coefficient $\Pi = \varepsilon T$. The uncoupled heat transfer and electric conduction problem, which renders the Fourier's law and Ohm's law, respectively, can be revealed by letting $\varepsilon = 0$. Introduce the thermoelectric potential function according to $H = \phi + \varepsilon T$ into (1)–(4), the thermoelectric constitutive and equilibrium equations can be rewritten as

$$\boldsymbol{J} = -\delta\nabla H, \qquad \boldsymbol{J}_u = H\boldsymbol{J} - \kappa\nabla T, \tag{5}$$

$$\nabla^2 H = 0, \qquad \kappa\nabla^2 T + \delta(\nabla H)^2 = 0. \tag{6}$$

The nonlinearity of the second in (6) makes the analysis in thermoelectric materials much more difficult. This will be illustrated below.

2.2. ***General solutions of thermoelectric field.*** Consider the generalized plane problem, in which all the physical quantities are assumed to be dependent on the in-plane coordinates (x, y). Note that the first in (6) is a Laplace's equation, the general solution then can be given by [Muskhelishvili 1975]

$$H = \mathrm{Re}\, f'(z), \tag{7}$$

where $f'(z)$ stands for an unknown potential function of complex variable $z = x + iy$ with i representing the imaginary unit and "Re" denoting the real part of a complex number. Combining (7) with the first in (5) gives

$$J_x - i\,J_y = -\delta f''(z). \tag{8}$$

On the other hand, inserting (7) into the second of (6) gives rise to

$$\nabla^2 T = -\frac{\delta}{T}\{\nabla \operatorname{Re} f'(z)\}^2 = -\frac{\delta}{\kappa} f''(z)\,\overline{f''(z)}, \tag{9}$$

where the superimposed bar denotes the complex conjugate. Solution of (9) then can be expressed by the superposition of a particular solution and the homogenous solution as

$$T = -\frac{\delta}{4\kappa} f'(z)\,\overline{f'(z)} + \operatorname{Re} g'(z), \tag{10}$$

where $g'(z)$ is an analytic complex function. Making use of (7), (8) and (10), the energy flux can be obtained from the second in (5) as

$$J_{ux} - i\,J_{uy} = -\frac{\delta}{2} f''(z)\, f'(z) - \kappa g''(z). \tag{11}$$

The thermal flux components and electric potential can be obtained, respectively, from (2) and the identity $\phi = H - \varepsilon T$ together with (7), (8), (10) and (11). Since they will not be used directly in the analysis, they are not given in detail. The resultant electric current density and energy flux from any point P_1 to P_2 on a directed curve denoted by s can be derived from (8) and (11) as

$$\int_{P_1}^{P_2} J_n(s)\,ds = -\operatorname{Im} \delta f'(z)\Big|_{P_1}^{P_2}, \tag{12}$$

$$\int_{P_1}^{P_2} J_{un}(s)\,ds = -\operatorname{Im}\Big[\frac{\delta}{4} f'^2(z) + \kappa g'(z)\Big]\Big|_{P_1}^{P_2}, \tag{13}$$

where the subscript "n" represents the normal component and "Im" stands for the imaginary part of a complex number.

In this section, the mathematical formulation of the coupled electric and heat conduction problem is thus completed. Once the two analytic complex functions $f'(z)$ and $g'(z)$ are obtained from exact electric and thermal boundary conditions, then all the quantities associated with the electric and temperature field can be determined.

2.3. ***General solutions of stress field.*** In case the temperature on the thermoelectric plane (x, y) is obtained, the thermal stresses caused by the uneven temperature distribution can be determined according to the Hooke's law of thermoelasticity. By combining the equilibrium equations, compatibility equations, thermoelastic stress-strain relationship, one can easily obtain the governing equations in terms of Airy stress function U as [Hasebe et al. 2009; Wang and Wang 2017]

$$\nabla^4 U + E\lambda\nabla^2 T = 0, \tag{14}$$

where

$$E = \begin{cases} E_0, \\ E_0/(1-\nu_0^2), \end{cases} \qquad \lambda = \begin{cases} \lambda_0, & \text{plane stress}, \\ (1+\nu_0)\lambda_0, & \text{plane strain}, \end{cases}$$

where E_0, ν_0 and λ_0 are the Young's modulus, Poisson's ratio and thermal expansion coefficient.

Inserting (9) into (14) yields

$$\nabla^4 U = \frac{k\delta}{\kappa} f''(z)\,\overline{f''(z)}\,,$$

where $k = E_0\lambda_0$ for plane stress and $k = E_0\lambda_0/(1-\nu_0)$ for plane strain. The complete solution of U includes a particular solution and a homogeneous solution. Using superposition principle, stresses and displacement can be expressed in terms of $f(z)$ and $g(z)$ together with other two complex potentials $\varphi(z)$ and $\psi(z)$. Omitting details, the components of stresses and displacement can be given as [Wang and Wang 2017; Yu et al. 2017]

$$\begin{aligned} \sigma_{yy}+\sigma_{xx} &= \frac{k\delta}{4\kappa}\, f'(z)\,\overline{f'(z)} + 2[\varphi'(z)+\overline{\varphi'(z)}], \\ \sigma_{yy}-\sigma_{xx}+2i\sigma_{xy} &= \frac{k\delta}{4\kappa}\, f''(z)\,\overline{f(z)} + 2[\bar{z}\varphi''(z)+\psi'(z)], \end{aligned} \tag{15}$$

$$2\mu(u_x+iu_y) = \beta\varphi(z) - z\,\overline{\varphi'(z)} - \overline{\psi(z)} - \frac{k\delta}{8\kappa}\,\overline{f'(z)}\, f(z) + 2\mu\lambda\, g(z), \tag{16}$$

where μ is the shear modulus and

$$\beta = \begin{cases} \dfrac{3-\nu_0}{1+\nu_0} & \text{(plane stress)}, \\ 3-4\nu_0 & \text{(plane strain)}. \end{cases}$$

Additionally, the resultant forces (F_x, F_y) on a certain directed curve s from any point P_1 to P_2 can be expressed by [Wang and Wang 2017; Yu et al. 2017]

$$i\int_{P_1}^{P_2} (F_x + iF_y)\, ds = \left[\varphi(z) + z\,\overline{\varphi'(z)} + \overline{\psi(z)} + \frac{k\delta}{8\kappa}\,\overline{f'(z)}\, f(z)\right]\Big|_{P_1}^{P_2}. \tag{17}$$

The mathematical formulation of the plane thermoelastic problem in a thermoelectric material is presented next. Once the thermoelectric fields are obtained, the associated thermal stress field can be solved by determining the two complex potentials $\varphi(z)$ and $\psi(z)$ with the aid of elastic boundary conditions given in (16) and (17).

3. Thermoelectric plane with an arbitrarily-shaped hole

3.1. ***Problem description and boundary condition.*** As shown in Figure 1, we consider an infinite thermoelectric material containing a hole of practically arbitrary shape subjected to a uniform electric current density J^∞ and a uniform energy flux J_u^∞ at infinity, in an arbitrary direction γ with respect to the x-axis. It is assumed that no far-field mechanical loads are imposed and the medium can expand freely at infinity. Furthermore, the hole can take arbitrary orientation such that the major axis of the hole is directed at angle η with respect to horizontal axis. The hole surface is assumed to be electrically impermeable, thermally insulated and mechanically free. These conditions can be expressed by

$$\left.\begin{aligned} J_n &= 0 \\ J_{qn} = J_{un} &= 0 \\ \sigma_{nn} + i\sigma_{nt} &= 0 \end{aligned}\right\} \quad \text{on } L. \tag{18}$$

It should be mentioned that the thermally insulated boundary condition $J_{qn} = 0$ is equivalent to $J_{un} = 0$ according to (4) and the first of (18). In what follows, we solve the complex functions $f(z)$ and $g(z)$ to determine the electric field and temperature field using the first and second conditions given in (18). Then,

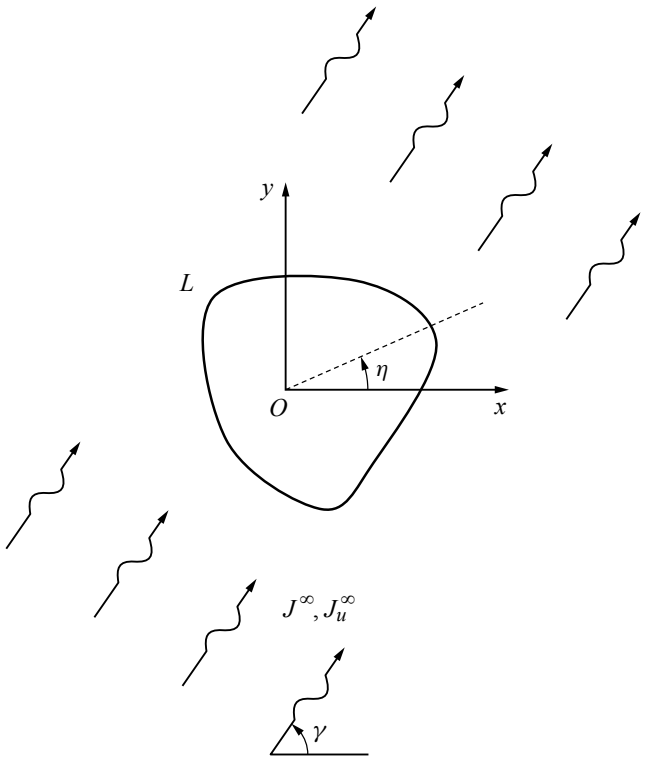

Figure 1. An infinite thermoelectric medium containing an arbitrarily-shaped hole.

the associated thermal stress field is obtainable from determining the complex functions $\varphi(z)$ and $\psi(z)$ based on the known temperature field and the stress boundary conditions described as the last in (18).

3.2. ***Series representations.*** Before embarking on the problem, we first introduce a conformal mapping of a truncated form, which associates the infinite region outside the hole in the z-plane with the exterior of the unit circle in the imaginary ξ-plane (see Figure 2), as [Dai et al. 2014]

$$z = \omega(\xi) = R\left(\xi + \sum_{j=1}^{M} m_j \xi^{-j}\right) e^{i\eta}, \quad |\xi| \geq 1, \tag{19}$$

where M is a positive integer, the parameter R, m_j $(j = 1, 2, \ldots, M)$ and η controls the overall size, shape and rotation of the hole. It should be mentioned that although (19) does not accomplish the mapping of an arbitrarily shaped hole, it can be made to approximate as closely as desired the shape of a wide variety of boundaries by the simple expedient of increasing the degree of the polynomial [Muskhelishvili 1975; Dai et al. 2014].

According to the single-value conditions of the thermoelectric potential (see (7)) and the equilibrium of the normal electric current density on the entire boundary (see the first in (12)), it is concluded that the derivative of the potential function $f'(z)$ must be single-valued, but $f(z)$ itself may be multi-valued. In the context of the mapping (19), one can give the expression of the thermoelectric potential function $f(z)$

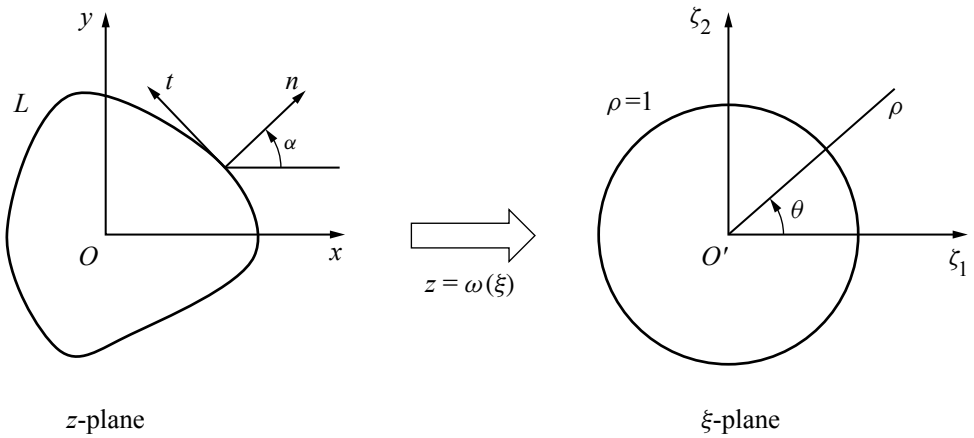

Figure 2. Conformal mapping.

via a truncated form as

$$f(z) = \frac{\Gamma_1}{2} z^2 + A \ln \xi + \sum_{j=1}^{N-1} a_j \xi^{-1}, \tag{20}$$

where Γ_1 is a complex constant to be determined from the remote electric current density. Inserting (20) into (8) and taking the limit $z \to \infty$ leads to

$$\Gamma_1 = -\frac{J^\infty e^{-i\gamma}}{\delta}. \tag{21}$$

A and a_j $(j = 1, 2, \ldots, N-1)$ are unknown complex coefficients to be determined. The chain rule gives

$$\frac{d}{dz} = \frac{d}{d\xi} \cdot \frac{d\xi}{dz} = \frac{1}{\omega'(\xi)} \cdot \frac{d}{d\xi}, \tag{22}$$

so the first and second spatial derivatives of $f(z)$ are

$$f'(z) = \Gamma_1 z + \frac{1}{\omega'(\xi)} \left(A\xi^{-1} - \sum_{j=1}^{N-1} j a_j \xi^{-j-1} \right), \tag{23}$$

$$f''(z) = \Gamma_1 + \frac{\left(-A\xi^{-2} + \sum_{j=1}^{N-1} j(j+1) a_j \xi^{-j-2}\right) \omega'(\xi) - \left(A\xi^{-1} - \sum_{j=1}^{N-1} j a_j \xi^{-j-1}\right) \omega''(\xi)}{\omega'(\xi)^3}. \tag{24}$$

The electrically insulated boundary condition on L can be expressed, according to (12), as

$$f'(z) = \overline{f'(z)}, \quad z \in L. \tag{25}$$

By using (23), boundary condition (25) can be rewritten as

$$\Gamma_1 \omega(\sigma) + \frac{1}{\omega'(\sigma)} \left(A\sigma^{-1} - \sum_{j=1}^{N-1} j a_j \sigma^{-j-1} \right) = \overline{\Gamma}_1 \overline{\omega(\sigma)} + \frac{1}{\overline{\omega'(\sigma)}} \left(\bar{A}\sigma - \sum_{j=1}^{n-1} j \overline{a_j} \sigma^{j+1} \right). \tag{26}$$

Then we expand every part of (26) into truncated Fourier series along boundary L:

$$\begin{aligned}
\frac{\sigma^{-1}}{\omega'(\sigma)} &= \sum_{k=-N}^{N} b_k^{(1)}\sigma^k, \qquad b_k^{(1)} = \frac{1}{2\pi}\int_0^{2\pi} \frac{\sigma^{-1}}{\omega'(\sigma)}\cdot\sigma^{-k}\,d\theta,\\
\frac{\sigma}{\overline{\omega'(\sigma)}} &= \sum_{k=-N}^{N} b_k^{(2)}\sigma^k, \qquad b_k^{(2)} = \frac{1}{2\pi}\int_0^{2\pi} \frac{\sigma}{\overline{\omega'(\sigma)}}\cdot\sigma^{-k}\,d\theta,\\
\frac{-j\sigma^{-j-1}}{\omega'(\sigma)} &= \sum_{k=-N}^{N} b_{j,k}^{(3)}\sigma^k, \qquad b_{j,k}^{(3)} = \frac{1}{2\pi}\int_0^{2\pi} \frac{-j\sigma^{-j-1}}{\omega'(\sigma)}\cdot\sigma^{-k}\,d\theta,\\
\frac{-j\sigma^{j+1}}{\omega'(\sigma)} &= \sum_{k=-N}^{N} b_{j,k}^{(4)}\sigma^k, \qquad b_{j,k}^{(4)} = \frac{1}{2\pi}\int_0^{2\pi} \frac{-j\sigma^{j+1}}{\overline{\omega'(\sigma)}}\cdot\sigma^{-k}\,d\theta,
\end{aligned} \tag{27}$$

where $b_k^{(1)}$ and $b_k^{(2)}$ are coefficients independent of j, while $b_{j,k}^{(3)}$ and $b_{j,k}^{(4)}$ are those related to j. These coefficients can be calculated numerically by Gaussian quadrature. Hence, (26) can be rewritten as

$$\Gamma_1\omega(\sigma) + A\sum_{k=-N}^{N} b_k^{(1)}\sigma^k + \sum_{k=-N}^{N}\sum_{j=1}^{n-1} a_j b_{j,k}^{(3)}\sigma^k = \overline{\Gamma_1}\,\overline{\omega(\sigma)} + \bar{A}\sum_{k=-N}^{N} b_k^{(2)}\sigma^k + \sum_{k=-N}^{N}\sum_{j=1}^{N-1}\overline{a_j}\, b_{j,k}^{(4)}\sigma^k. \tag{28}$$

Equating the coefficients of σ^j, $j = 1, 2, \ldots, N$, yields N complex equations which are equivalent to $2N$ real equations. Clearly, these real equations are linear with respect to the real and imaginary parts of all the complex coefficients A and a_j $(j = 1, 2, \ldots, N-1)$. Once all the complex coefficients are determined by solving these linear equations, the thermoelectric potential $f(z)$ can be easily obtained through (20).

In the same manner, the potential functions $g(z)$ and its derivative should take the following forms:

$$g(z) = \frac{\Gamma_3}{3}z^3 + \frac{\Gamma_2}{2}z^2 + C\ln\xi + \sum_{j=1}^{2N-1} c_j\xi^{-1}, \tag{29}$$

$$g'(z) = \Gamma_3 z^2 + \Gamma_2 z + \frac{1}{\omega'(\xi)}\left(C\xi^{-1} - \sum_{j=1}^{2N-1} j c_j \xi^{-j-1}\right), \tag{30}$$

where Γ_2 and Γ_3 are two complex constants to be determined from the remote energy flux condition. Inserting (20) and (30) into (11) and taking the limit $z \to \infty$ gives

$$\Gamma_2 = -\frac{J_u^{\infty} e^{-i\gamma}}{\kappa}, \qquad \Gamma_3 = -\frac{\delta}{4\kappa}\Gamma_1^2 = -\frac{J^{\infty 2} e^{-2i\gamma}}{4\kappa\delta}. \tag{31}$$

The remaining constant coefficients C and c_j, $(j = 1, 2, \ldots, 2N-1)$ may be determined from the thermal boundary condition on the hole rim. According to (13) and the second of (18), the thermally insulated boundary condition on the hole rim L is expressed by

$$g'(z) + \frac{\delta}{4\kappa} f'(z)^2 = \overline{g'(z)} + \frac{\delta}{4\kappa}\,\overline{f'(z)}^2, \quad z \in L. \tag{32}$$

From (30), one has

$$\Gamma_3\omega(\sigma)^2+\Gamma_2\omega(\sigma)+\frac{1}{\omega'(\sigma)}\left(C\sigma^{-1}-\sum_{j=1}^{2N-1}jc_j\sigma^{-j-1}\right)+\frac{\delta}{4\kappa}f'^2(\sigma)$$
$$=\overline{\Gamma_3}\,\overline{\omega(\sigma)}^2+\overline{\Gamma_2}\,\overline{\omega(\sigma)}+\frac{1}{\overline{\omega'(\sigma)}}\left(\bar{C}\sigma-\sum_{j=1}^{2N-1}j\,\overline{c_j}\,\sigma^{j+1}\right)+\frac{\delta}{4\kappa}\,\overline{f'^2(\sigma)}, \quad (33)$$

where $f'(\sigma)$ represents the boundary value of function $f'(z)$ on the boundary $z=\omega(\sigma)\in L$. Note that the thermoelectric potential $f'(z)$ is determined in the above section as

$$\begin{aligned} f'(\sigma)&=f'[\omega(\sigma)]=\Gamma_1\omega(\sigma)+A\sum_{k=-N}^{N}b_k^{(1)}\sigma^k+\sum_{k=-N}^{N}\sum_{j=1}^{N-1}a_j\,b_{j,k}^{(3)}\sigma^k,\\ \overline{f'(\sigma)}&=\overline{f'[\omega(\sigma)]}=\overline{\Gamma_1}\,\overline{\omega(\sigma)}+\bar{A}\sum_{k=-N}^{N}b_k^{(2)}\sigma^k+\sum_{k=-N}^{N}\sum_{j=1}^{N-1}\overline{a_j}\,b_{j,k}^{(4)}\sigma^k. \end{aligned} \quad (34)$$

In what follows, the Fourier series method is also taken to deal with the boundary condition (33) as what we did on (26). Here we expand both sides of (33) into the Fourier series of σ by numerical quadrature, respectively, and then equate the coefficients of σ^j $(j=1,2,\ldots,2N)$ on the two sides of (33), leading to $2N$ complex equations (equivalent to $4N$ real equations) which are linear with respect to the real and imaginary parts of all the complex coefficients C and c_j $(j=1,2,\ldots,2N-1)$. Finally, all the unknowns are obtained through solving the linear system of equations.

Since no far-field mechanical loads are imposed on the medium and only the electrically and thermally induced stresses are considered here, the two elastic potentials $\varphi(z)$ and $\psi(z)$ can be expressed in terms of truncated series as

$$\varphi(z)=P(\xi)\ln\xi+\sum_{j=1}^{2N}p_j\xi^{-1},\qquad \psi(z)=Q(\xi)\ln\xi+\sum_{j=1}^{2N}q_j\xi^{-1}, \quad (35)$$

where p_j and q_j are complex coefficients to be determined, and the coefficients $P(\xi)$ and $Q(\xi)$ identifying the multi-valued terms can be specified, according to the single-value condition of displacement (see (16)) and the vanishing resultant force vector over the entire boundary L (see (17)), as

$$P(\xi)=P_0=-\frac{2\mu\lambda C}{\beta+1},\qquad Q(\xi)=\overline{P_0}+\frac{k\delta\bar{A}}{8\kappa}f'(\xi), \quad (36)$$

where $f'(\xi)=f'[\omega(\xi)]$. According to (17), the traction-free condition on the hole surface (the last in (18)) can be expressed by

$$P_0\ln\sigma+\sum_{j=1}^{2N}p_j\sigma^{-1}+\frac{\omega(\sigma)}{\overline{\omega'(\sigma)}}\left(\overline{P_0}\sigma-\sum_{j=1}^{2N}\overline{P_j}\,j\sigma^{j+1}\right)$$
$$-\left[P_0+\frac{k\delta A}{8\kappa}\,\overline{f'(\sigma)}\right]\ln\sigma+\sum_{j=1}^{2N}\overline{q_j}\,\sigma^j+\frac{k\delta}{8\kappa}\,\overline{f'(\sigma)}\,f(\sigma)=0, \quad (37)$$

where

$$f(\sigma) = f[\omega(\sigma)] = \frac{\Gamma_1}{2}\omega(\sigma)^2 + A\ln\sigma + \sum_{j=1}^{N} a_j \sigma^{-j}. \tag{38}$$

In the same manner, the Fourier series method is also taken to deal with the boundary condition (37). As what we did on (26), here we expand both sides of (37) into the Fourier series of σ by numerical quadrature, respectively, and then equate the coefficients of σ^j $(-2N, -2N+1, \ldots, -1, 1, 2, \ldots, 2N)$ on the two sides of (37), leading to $4N$ complex equations which can be used to determine all the complex coefficients p_j and q_j $(j = 1, 2, \ldots, 2N)$. Once all the complex coefficients are obtained, the complex potentials $\varphi(z)$ and $\psi(z)$ can be determined by noting (35) and (36), and therefore the stress fields in the material are obtained. Using the stress transformation formula, stress components in the material in polar coordinates can be determined by

$$\sigma_{nm} + \sigma_{tt} = \sigma_{yy} + \sigma_{xx}, \qquad \sigma_{tt} - \sigma_{nm} + 2i\sigma_{nt} = e^{2i\alpha}(\sigma_{yy} - \sigma_{xx} + 2i\sigma_{xy}), \tag{39}$$

where σ_{nn}, σ_{tt} and σ_{nt} are the normal stress, hoop stress and shear stress, respectively, and α is the angle between the outer normal on L and the positive x-axis in the z-plane, which is determined by

$$e^{2i\alpha} = \frac{\xi^2 \omega'(\xi)}{\rho^2 \overline{\omega'(\xi)}}. \tag{40}$$

4. Numerical examples

So far, the analytical solutions for the problem of an arbitrarily-shaped hole have been obtained in the form of a finite series. To verify the compatibility and the feasibility of our proposed solutions, we present some examples and compare the results obtained from the presented method with those of the previous work. Firstly, an electrically and thermally insulated elliptical hole in a thermoelectric medium under different loading conditions is considered. The mapping function for the elliptical hole is given by

$$z = \omega(\xi) = R\left(\xi + \frac{m}{\xi}\right), \tag{41}$$

where $R = (a+b)/2$ and $m = (a-b)/(a+b)$ with a and b being the semi-major and the semi-minor axes of the elliptical hole. In the case of $a/b = 5$, the hoop stress distributions around the elliptical hole when only the remote electric current load is imposed and only the remote energy flux load is applied along the positive y-axis are plotted in Figure 3 (top left) and Figure 3 (top right), respectively. It should be mentioned that the stresses produced by the applied electric current and energy flux loads in thermoelectric materials are found to be uncoupled according to [Wang and Wang 2017], which enables us to analyze the effects of the electric current and energy flux loads separately. Furthermore, $\sigma_{e0} = kJ^{\infty 2}R^2/8\delta\kappa$ and $\sigma_{u0} = 2\mu\lambda J_u^{\infty} R/\kappa(\beta+1)$, which have the same unit as stresses, are used to normalize the hoop stresses caused by the far-field electric current and energy flux loads, respectively. It is clearly seen that the results obtained by our solution agree very well with those given by Wang and Wang [2017] for an insulated elliptical hole.

To further verify the compatibility of the presented solutions, we consider the generalized thermoelastic problems of a thermally insulated quasi-square hole and a thermally insulated ovaloid hole in

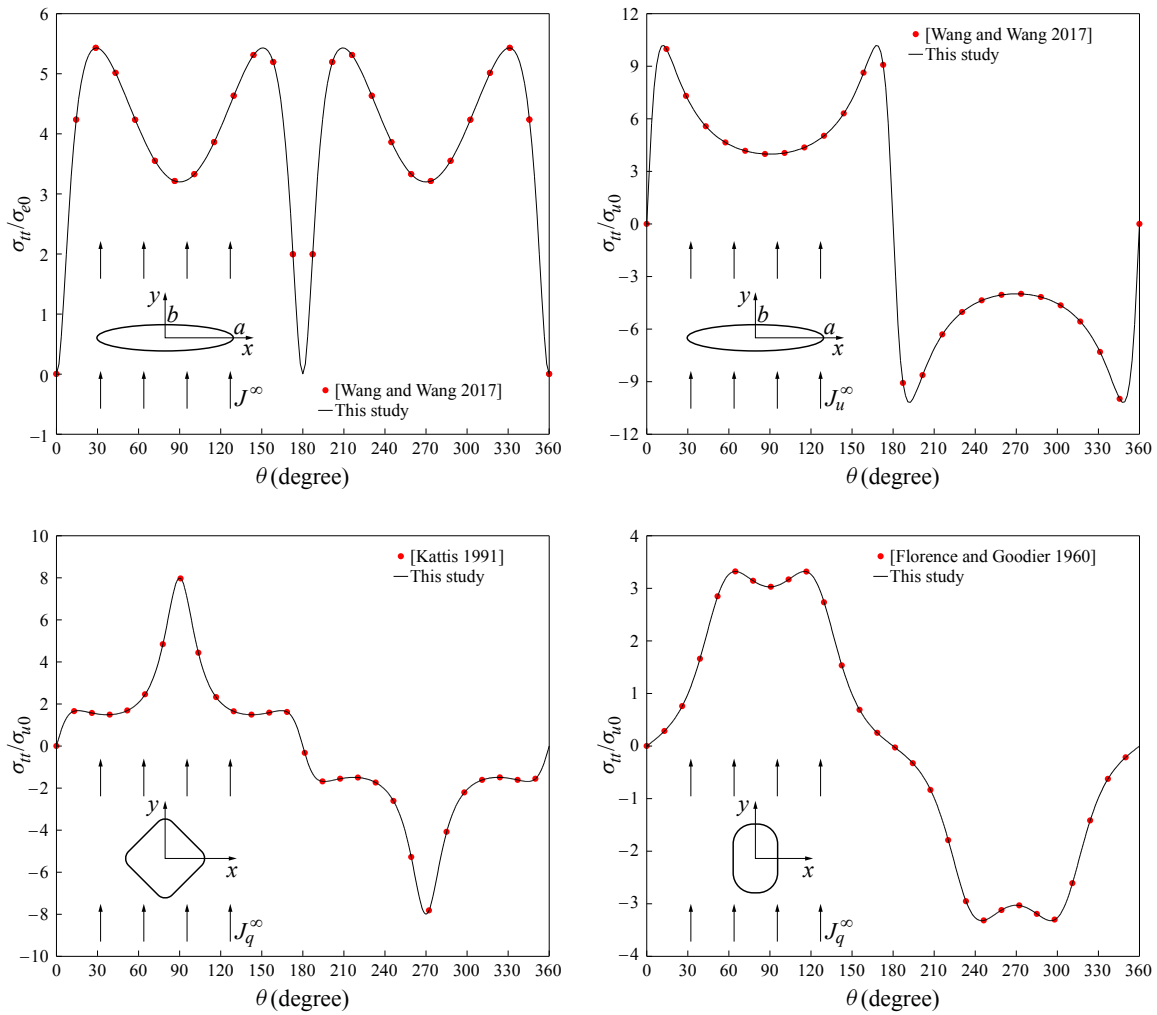

Figure 3. Comparisons of the present work to the previous work for some special cases.

an infinite elastic matrix subjected to a uniform thermal flux. To this end, the medium in this case is considered to be electrically insulated, that is, $\delta = 0$. Thus, no electric current exists in the material and the energy flux is completely equivalent to the heat flux, as seen from (1) and (4). The mapping functions (19) for the quasi-square hole and the oval hole considered here are given by

$$\begin{aligned} z = \omega(\xi) &= R\left(\xi + \frac{1}{8}\xi^{-3}\right), && \text{(Square hole)},\\ z = \omega(\xi) &= R\left(\xi - \frac{1}{5}\xi^{-1} - \frac{1}{20}\xi^{-3}\right), && \text{(Ovaloid hole)}. \end{aligned} \tag{42}$$

A comparison between the results of the present study and the results obtained by Kattis [1991] for a square hole is plotted in Figure 3 (bottom left). Here, $\sigma_{q0} = 2\mu\lambda J_q^\infty R/\kappa(\beta+1)$ is used to normalize

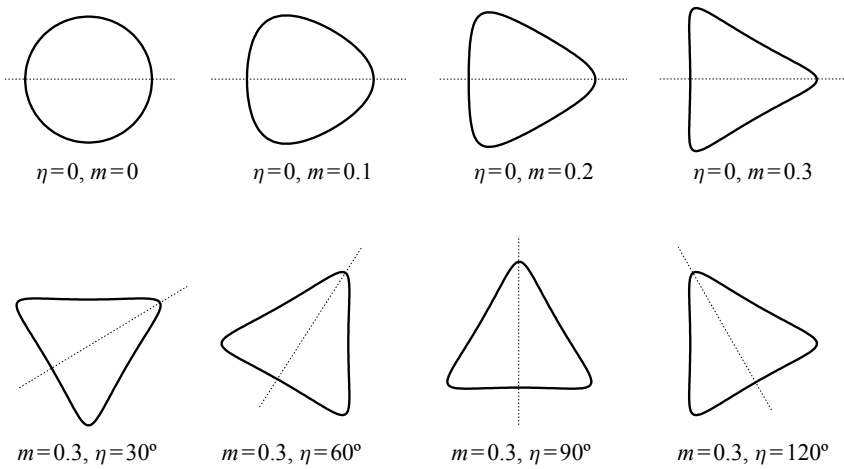

Figure 4. The effect of parameters m and η on the hole shape.

the hoop stresses produced by the far-field thermal flux. In addition, Figure 3 (bottom right) shows the comparison of our solution with that of Florence and Goodier [1960] for the ovaloid cutout under a uniform thermal flux applied at infinity. It can be found that the normalized hoop stress around the holes of given shapes obtained by the presented solution are almost identical to those of the previous work, which further verifies the validity of the present formulation.

To illustrate the application of the analysis method, the hoop stress around a triangular hole will be presented below. For the triangular hole, the mapping function (19) can be given as

$$z = \omega(\xi) = R(\xi + m\xi^{-2})e^{i\eta}. \tag{43}$$

The conditions $0 \leq m < 1/2$ ensure that the hole shape does not have loops. The radius of curvature at the corner of the hole and the orientation of the hole vary by changing the parameters m and η, respectively, as shown in Figure 4. It can be seen that the corner of the hole becomes sharper with increasing the parameter m.

The distribution of the electric current on the hole rim when a uniform electric current is solely loaded along the positive y-axis is plotted in Figure 5. It is found that the electric current around the triangular hole has a concentration at the corners. As the corner becomes sharper, the electric current concentration is more obvious. For given load direction ($\gamma = 90°$) and hole orientation ($\eta = 0$), the maximum concentration of the electric current on the hole occurs at $\theta = 0$. Furthermore, the distributions of energy flux under a uniform energy load is found to be similar with that of the electric current and thus a similar conclusion could be drawn.

When there is only electric current loaded along the vertical direction ($\gamma = 90°$), the distribution of the normalized hoop stress around the hole is plotted in Figure 6. Likely, when there is only energy flux imposed along the vertical direction, the distribution of the normalized hoop stress is plotted in Figure 7. Here, the hole orientation is set to be zero, namely $\eta = 0$. We find that both applied electric current and energy flux generate thermal stress around hole and thermal stress becomes more concentrated as the corner becomes sharper. In addition, the maximum stress concentration generated by both electric

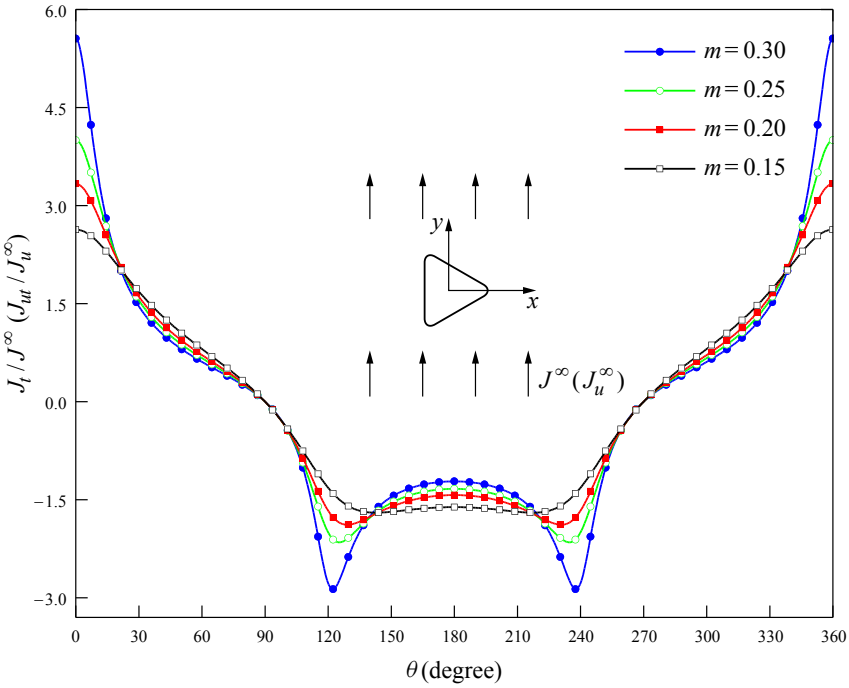

Figure 5. Variation of normalized electric current (energy flux) on the hole rim with θ when $J^\infty(J_u^\infty)$ is solely applied.

current and energy flux occurs at $\theta = 120°$ and $\theta = 240°$ in this case. The difference is that the applied electric current produces thermal stress concentration at the corner of $\theta = 0°$ but the energy flux load does not under the same loading condition. Another difference is that the applied energy flux produces the opposite stress state on any two points symmetric with respect to x-axis, however, the imposed electric current produces the same stress state.

Figures 8 and 9 show the periodic behavior of the remote electric current and energy flux induced hoop stress at point $\theta = 0°$ in terms of load angle γ, respectively. These results have been presented for the case of $\eta = 0$. It can be seen from Figure 8 that hoop stress induced by J^∞ varies periodically as the load angle γ changes (with a period of 180°). According to Figure 9, the stress induced by J_u^∞ is also a periodic function of the load angle γ, however, the period becomes to be 360°. When $\gamma = 90°$ or 270°, both the electric current and energy flux induced hoop stresses reach their minimum values.

The interesting results shown in Figures 10 and 11 are that for given load angle $\gamma = 90°$, the maximum hoop stress induced by J^∞ and J_u^∞ varies when the rotation of the hole η is changed. The normalized hoop stress produced by J^∞ obtained its maximum value when the hole oriented at 30° and 90°. On the other hand, the normalized hoop stress produced by J_u^∞ obtained its maximum value when $\eta = 30°$ and obtained its minimum value when $\eta = 90°$. It should be mentioned that the maximum normalized stresses are very important in design and implementation for thermoelectric devices. The maximum normalized stress might cause damages to thermoelectric structure and thus should be avoided.

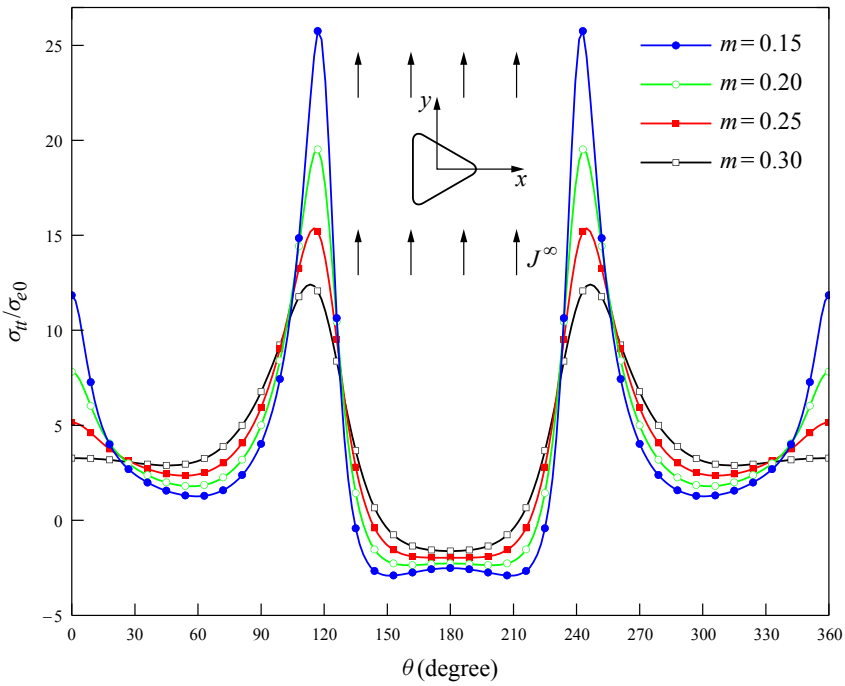

Figure 6. Variation of normalized hoop stress with θ when J^{∞} is solely applied.

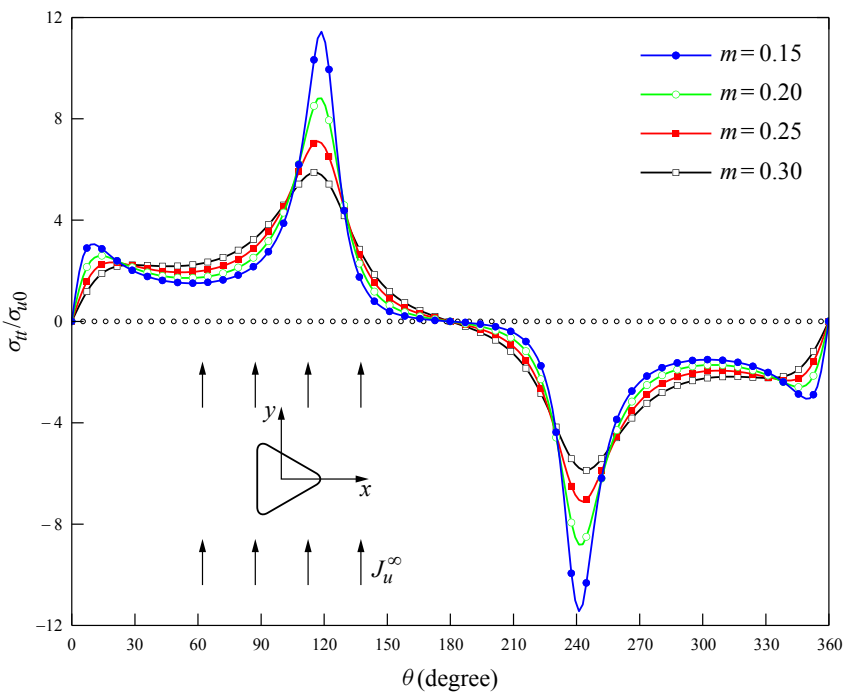

Figure 7. Variation of normalized hoop stress with θ when J_u^{∞} is solely applied.

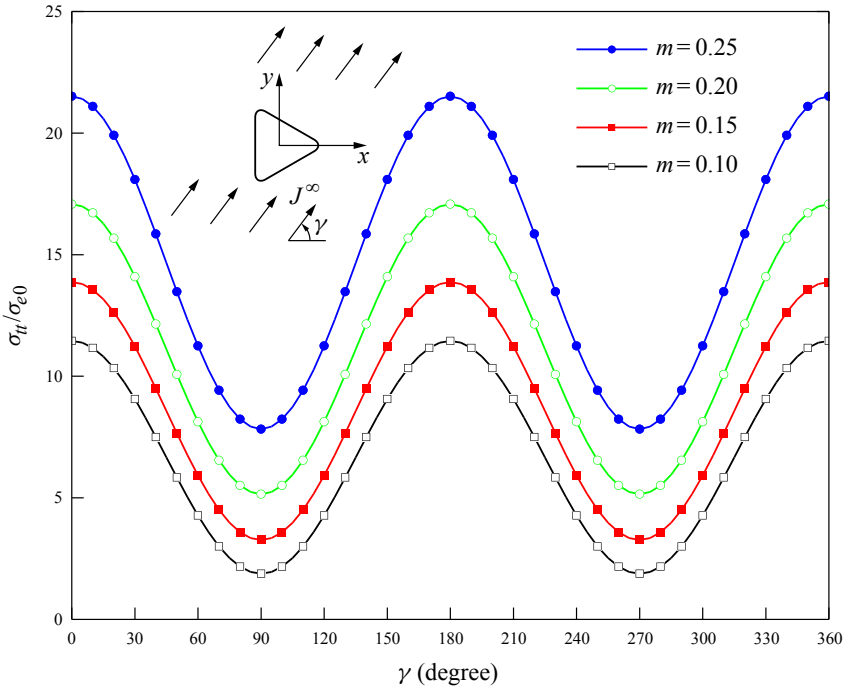

Figure 8. Periodic behavior of hoop stress at $\theta = 0°$ in terms of γ when J^{∞} is solely applied.

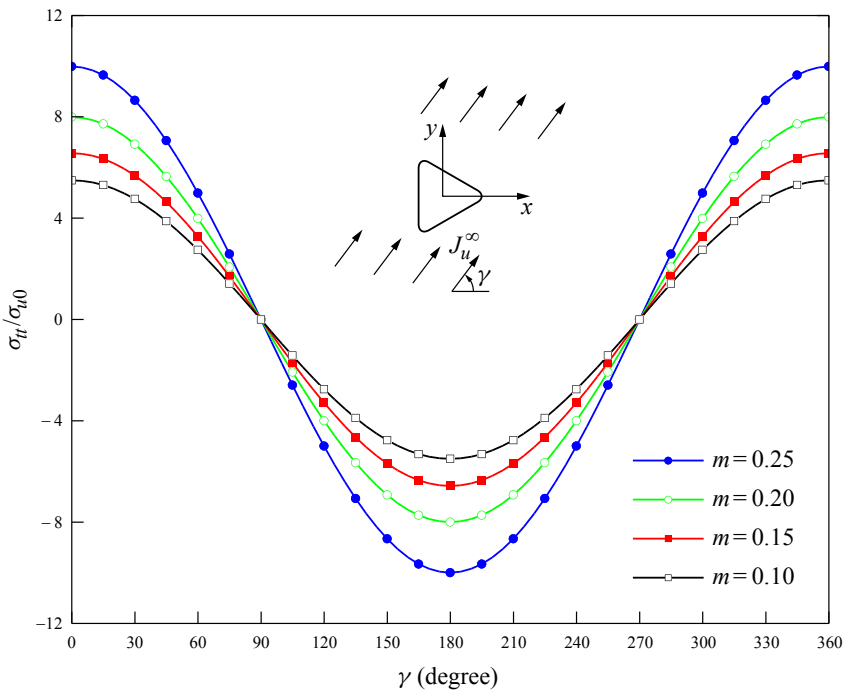

Figure 9. Periodic behavior of hoop stress at $\theta = 0°$ in terms of γ when J_u^{∞} is solely applied.

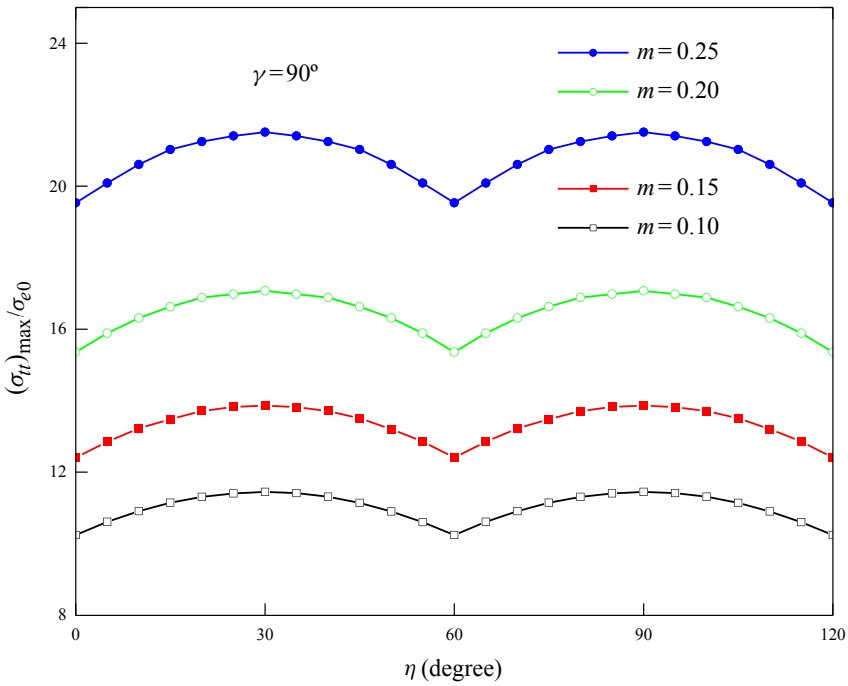

Figure 10. Variation of the maximum normalized hoop stress with η when J^{∞} is solely applied.

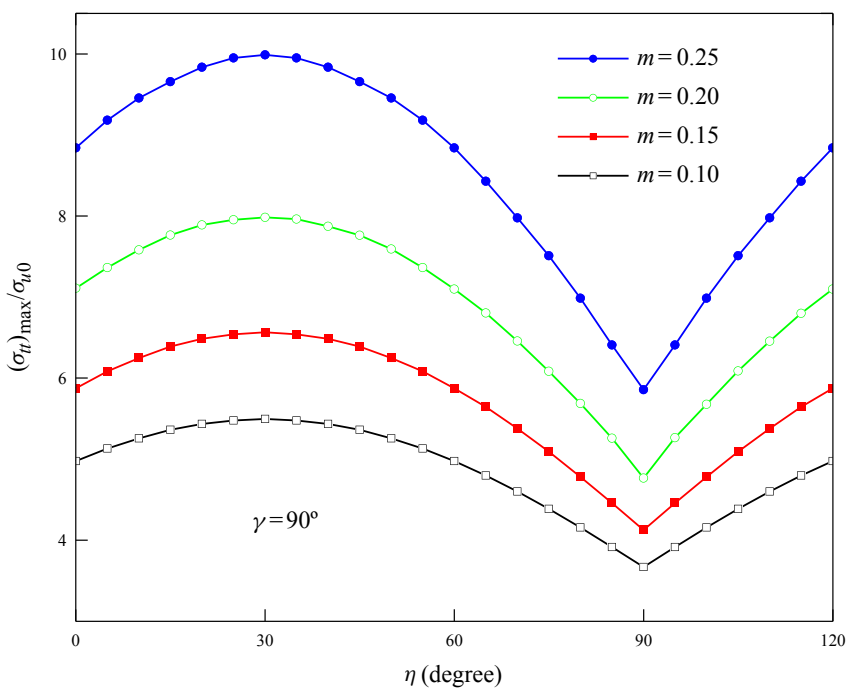

Figure 11. Variation of the maximum normalized hoop stress with η when J_u^{∞} is solely applied.

5. Concluding remarks

Stress concentration around the holes is of practical importance in designing of the thermoelectric structures. The hole shape is one of the important parameters that affects the location and amount of maximum hoop stress. Based on the complex variable method, a simple analytical solution was presented in this study. This solution provided a numerical result to obtain the normalized hoop stress for thermoelectric materials with regular holes with various shapes. Numerical study was conducted to investigate the effects of different parameters such as the load angle, rotation angle of hole, bluntness on the hoop stress. The results show that the loading angle and hole orientation have a significant impact in reducing the normalized stress in addition to increasing the bluntness. By the correct selection of these parameters, the lowest amount of thermal stress could be achieved.

Acknowledgements

Yu and Gao acknowledge the support from the National Natural Science Foundation of China (Grant Number 11232007 and 11472130) and a Project Funded by the Priority Academic Program Development of Jiangsu Higher Education Institutions (PAPD). Yang thanks the support from the National Natural Science Foundation of China (Grant Number 11702147).

References

[Bell 2008] L. E. Bell, "Cooling, heating, generating power, and recovering waste heat with thermoelectric systems", *Science* **321**:5895 (2008), 1457–1461.

[Chao and Wang 1993] C. K. Chao and J. L. Wang, "Failure prediction of a plate weakened by an elliptic hole under thermal or mechanical load", *Eng. Fract. Mech.* **45**:6 (1993), 843–856.

[Chen and Chao 2008] F. M. Chen and C. K. Chao, "Stress analysis of an infinite plate with a coated elliptic hole under a remote uniform heat flow", *J. Therm. Stresses* **31**:7 (2008), 599–613.

[Dai et al. 2014] M. Dai, C.-F. Gao, and C. Q. Ru, "Surface tension-induced stress concentration around a nanosized hole of arbitrary shape in an elastic half-plane", *Meccanica* (*Milano*) **49**:12 (2014), 2847–2859.

[Florence and Goodier 1960] A. L. Florence and J. N. Goodier, "Thermal stresses due to disturbance of uniform heat flow by an insulated ovaloid hole", *J. Appl. Mech.* (*ASME*) **27**:4 (1960), 635–639.

[Gao et al. 2002] C.-F. Gao, Y.-T. Zhao, and M.-Z. Wang, "An exact and explicit treatment of an elliptic hole problem in thermopiezoelectric media", *Int. J. Solids Struct.* **39**:9 (2002), 2665–2685.

[Hasebe 2009] N. Hasebe, "Magneto-elastic stress induced by an electric current in an infinite thin plate with an elliptical hole", *Arch. Appl. Mech.* **80**:12 (2009), 1353–1370.

[Hasebe and Wang 2005] N. Hasebe and X. Wang, "Complex variable method for thermal stress problem", *J. Therm. Stresses* **28**:6-7 (2005), 595–648.

[Hasebe et al. 2009] N. Hasebe, C. Bucher, and R. Heuer, "Analyses of thermal conduction and stress induced by electric current in an infinite thin plate with an elliptical hole", *J. Therm. Stresses* **32**:10 (2009), 1065–1086.

[He and Tritt 2017] J. He and T. M. Tritt, "Advances in thermoelectric materials research: looking back and moving forward", *Science* **357**:6358 (2017), eaak9997.

[He et al. 2015] W. He, G. Zhang, X. Zhang, J. Ji, G. Li, and X. Zhao, "Recent development and application of thermoelectric generator and cooler", *Appl. Energy* **143**:1 (2015), 1–25.

[Jafari et al. 2016] M. Jafari, M. B. Nazari, and A. Taherinasab, "Thermal stress analysis in metallic plates with a non-circular hole subjected to uniform heat flux", *Eur. J. Mech. A Solids* **59** (2016), 356–363.

[Kattis 1991] M. A. Kattis, "Thermoelastic plane problems with curvilinear boundaries", *Acta Mech.* **87**:1-2 (1991), 93–103.

[Li et al. 2015] G. Li, Q. An, W. Li, W. A. Goddard, P. Zhai, Q. Zhang, and G. J. Snyder, "Brittle failure mechanism in thermoelectric skutterudite $CoSb_3$", *Chem. Mater.* **27**:18 (2015), 6329–6336.

[Muskhelishvili 1975] N. I. Muskhelishvili, *Some basic problems of the mathematical theory of elasticity*, Noordhoff, Groningen, 1975.

[Pang et al. 2018] S.-J. Pang, Y.-T. Zhou, and F.-J. Li, "Analytic solutions of thermoelectric materials containing a circular hole with a straight crack", *Int. J. Mech. Sci.* **144** (2018), 731–738.

[Qin 1999] Q.-H. Qin, "Green's function for thermopiezoelectric plates with holes of various shapes", *Arch. Appl. Mech.* **69**:6 (1999), 406–418.

[Qin 2000] Q.-H. Qin, "General solutions for thermopiezoelectrics with various holes under thermal loading", *Int. J. Solids Struct.* **37**:39 (2000), 5561–5578.

[Rasouli and Jafari 2016] M. Rasouli and M. Jafari, "Thermal stress analysis of infinite anisotropic plate with elliptical hole under uniform heat flux", *J. Therm. Stresses* **39**:11 (2016), 1341–1355.

[Schmidt et al. 2015] R. D. Schmidt, X. Fan, E. D. Case, and P. B. Sarac, "Mechanical properties of Mg_2Si thermoelectric materials with the addition of 0–4 vol% silicon carbide nanoparticles (SiC_{NP})", *J. Mater. Sci.* **50**:11 (2015), 4034–4046.

[Tritt and Subramanian 2006] T. M. Tritt and M. A. Subramanian, "Thermoelectric materials, phenomena, and applications: a bird's eye view", *MRS Bull.* **31**:3 (2006), 188–198.

[Wang and Wang 2017] P. Wang and B. L. Wang, "Thermoelectric fields and associated thermal stresses for an inclined elliptic hole in thermoelectric materials", *Int. J. Eng. Sci.* **119** (2017), 93–108.

[Yang and Gao 2010] Q. Yang and C.-F. Gao, "Non-axisymmetric thermal stress around a circular hole in a functionally graded infinite plate", *J. Therm. Stresses* **33**:4 (2010), 318–334.

[Yang et al. 2013] Y. Yang, F. Y. Ma, C. H. Lei, Y. Y. Liu, and J. Y. Li, "Nonlinear asymptotic homogenization and the effective behavior of layered thermoelectric composites", *J. Mech. Phys. Solids* **61**:8 (2013), 1768–1783.

[Yoshikawa and Hasebe 1999] K. Yoshikawa and N. Hasebe, "Green's function for a heat source in an infinite region with an arbitrary shaped hole", *J. Appl. Mech.* (*ASME*) **66**:1 (1999), 204–210.

[Yu et al. 2017] C. Yu, D. Zou, Y.-H. Li, H.-B. Yang, and C.-F. Gao, "An arc-shaped crack in nonlinear fully coupled thermoelectric materials", *Acta Mech.* **229**:5 (2017), 1989–2008.

[Zhang and Wang 2016] A. B. Zhang and B. L. Wang, "Explicit solutions of an elliptic hole or a crack problem in thermoelectric materials", *Eng. Fract. Mech.* **151** (2016), 11–21.

Received 20 Sep 2018. Revised 24 Mar 2019. Accepted 29 May 2019.

CHUAN-BIN YU: cbyu@nuaa.edu.cn
State Key Laboratory of Mechanics and Control of Mechanical Structures, Nanjing University of Aeronautics and Astronautics, Nanjing, 210016, China

HAI-BING YANG: yanghb@scut.edu.cn
Department of Mechanics Engineering, School of Civil Engineering and Transportation, South China University of Technology, Guangzhou, 510641, China

KUN SONG: ksong3@ualberta.ca
State Key Laboratory of Mechanics and Control of Mechanical Structures, Nanjing University of Aeronautics and Astronautics, Nanjing, 210016, China

CUN-FA GAO: cfgao@nuaa.edu.cn
State Key Laboratory of Mechanics and Control of Mechanical Structures, Nanjing University of Aeronautics and Astronautics, Nanjing, 210016, China

JOURNAL OF MECHANICS OF MATERIALS AND STRUCTURES
Vol. 14, No. 2, 2019
dx.doi.org/10.2140/jomms.2019.14.277

THE EFFECT OF VARIABLE THERMAL CONDUCTIVITY ON AN INFINITE FIBER-REINFORCED THICK PLATE UNDER INITIAL STRESS

MOHAMED I. A. OTHMAN, AHMED E. ABOUELREGAL AND SAMIA M. SAID

The present paper includes an analytical study of the effect of variable thermal conductivity and initial stress on a fiber-reinforced transversely isotropic thick plate. The model of the equations of generalized thermoelasticity with phase lags in an isotropic elastic medium with temperature-dependent mechanical properties are established. The upper surface of the plate is thermally insulated with prescribed surface loading while the lower surface of the plate rests on a rigid foundation and temperature. The normal mode analysis is used to obtain the analytical expressions of the displacement components, force stress and temperature distribution. Numerical results for the physical quantities are given and illustrated graphically with temperature-dependent and temperature-independent thermal conductivity. A comparison is made with results obtained with initial stress and without initial stress. Also, a comparison is made with results obtained with reinforcement and without reinforcement proprieties. It is found from the graphs that the initial stress, the reinforcement and phase lags have great effects on the distribution of the field quantities.

1. Introduction

Fiber-reinforced composites are used in a variety of structures due to their low weight and high strength. The analysis of stress and deformation of fiber-reinforced composite materials has been an important subject of solid mechanics for last three decades. The mechanical behavior of many fiber-reinforced composite materials is adequately modeled by the theory of linear elasticity for transversely isotropic materials, with the preferred direction coinciding with the fiber direction. In such composites the fibers are usually arranged in parallel straight lines. Other configurations are used. An example is that of circumferential reinforcement, for which the fibers are arranged in concentric circles, giving strength and stiffness in the tangential (or hoop) direction. The analysis of stress and deformation of fiber-reinforced composite materials has been an important subject of solid mechanics for last three decades. The characteristic property of a reinforced concrete member is that its components, namely concrete and steel, act together as a single anisotropic unit as long as they remain in the elastic condition, i.e., the two components are bound together so that there can be no relative displacement between them.

In the past few years, attention had been given to the problems of the generation and propagation of elastic waves in anisotropic elastic solid or layers of different configurations. The propagation of elastic waves in anisotropic media is fundamentally different from their propagation in isotropic media. The information obtained from such studies is important to seismologists and geophysicists to find the

Keywords: dual-phase-lag model, fiber-reinforced, initial stress, normal mode analysis, variable thermal conductivity, thick plate.

location of the earthquakes as well as their energy, mechanism etc. and thereby gives valuable insight into the global tectonics. Some hard and soft rocks beneath the earth's surface show the reinforcement properties, i.e., the different components act as a single anisotropic unit. These rocks when come in the way of seismic waves do affect their propagation and such seismic signals are always influenced by the elastic properties of the media through which they travel. Fiber-reinforced composites are used in a variety of structures due to their low weight and high strength. A continuum model is used to explain the mechanical properties of such materials. In the case of an elastic solid reinforced by a series of parallel fibers, it is usual to assume transverse isotropy.

In the linear case, the associated constitutive relations, relating infinitesimal stress and strain components, have five materials constants. The idea of introducing a continuous self reinforcement at every point of an elastic solid was given by Belfield et al. [1983]. The model was later applied to the rotation of a tube by Verma and Rana [1983]. Sengupta and Nath [2001] discussed the problem of the surface waves in fiber-reinforced anisotropic elastic media. Hashin and Rosen [1964] gave the elastic moduli for fiber-reinforced materials. The two-dimensional problems of the generalized magneto-thermoelasticity in a fiber-reinforced anisotropic half-space was discussed by Abbas et al. [2011]. Othman and Abbas [2011] discussed the effect of rotation on plane waves at the free surface of a fiber-reinforced thermoelastic half-space using the finite element method. Ailawalia and Budhiraja [2011] discussed the effect of hydrostatic initial stress on fiber-reinforced generalized thermoelastic medium. Abbas and Abd-alla [2011] studied the effect of initial stress on a fiber-reinforced anisotropic thermoelastic thick plate. Othman and Said [2012] investigated the effect of rotation on the two-dimensional problem of a fiber-reinforced thermoelastic with one relaxation time.

The theory of thermoelasticity including the effect of temperature change has been well established. According to this theory, the temperature field is coupled with the elastic strain field. In thermoelasticity, classical heat transfer, Fourier's conduction equation is extensively used in many engineering applications. The classical theory of thermoelasticity by Nowacki [1975; 1986] rests upon the hypothesis of the Fourier law of heat conduction, in which the temperature distribution is governed by a parabolic-type partial differential equation. Consequently, the theory predicts that a thermal signal is felt instantaneously everywhere in a body. This implies that an infinite speed of propagation of the thermal signal, which is impractical from the physical point of view, particularly for short-time. Thus, the use of Fourier's equation may result in discrepancies under some special conditions, such as low-temperature heat transfer, high frequency or ultrahigh heat flux heat transfer.

The theory of the classical uncoupled theory of thermoelasticity predicts two phenomena not compatible with physical observations. First, the equation of heat conduction of this theory does not contain any elastic term contrary to the fact that the elastic changes produce heat effects. Second, the heat equation is of parabolic type predicting infinite speeds of propagation for heat waves. Biot [1956] introduced the theory of coupled thermoelasticity to overcome the first shortcoming.

Generalized thermoelasticity theories have been developed with the objective of removing the paradox of infinite speed of heat propagation inherent in the conventional coupled dynamical theory of thermoelasticity in which the parabolic type heat conduction equation is based on Fourier's law of heat conduction.

Lord and Shulman [1967] introduced a theory of generalized thermoelasticity with one relaxation time for an isotropic body. In this theory, a modified law of heat conduction, including both the heat flux and its time derivatives replaces the conventional Fourier's law. The heat equation associated with this theory

is hyperbolic and hence eliminates the paradox of infinite speeds of propagation inherent in both coupled and uncoupled theories of thermoelasticity. Green and Lindsay [1972] extended the coupled theory of thermoelasticity by introducing the thermal relaxation times in the constitutive equations. The theory of thermoelasticity without energy dissipation is another generalized theory and was formulated by Green and Naghdi [1993]. It includes the "thermal displacement gradient" among its independent constitutive variables, and differs from the previous theories in that it does not accommodate dissipation of thermal energy. Tzou [1996; 1995a] proposed the dual-phase-lag DPL model, which describes the interaction between phonons and electrons on the microscopic level as retarding sources causing a delayed response on the macroscopic scale. For macroscopic formulation, it would be convenient to use the DPL model for investigation of the micro-structural effect on the behavior of heat transfer. The DPL proposed by Chandrasekharaiah [1986] and Tzou [1995b] is such a modification of the classical thermoelastic model in which the Fourier law is replaced by an approximation to a modified Fourier law with tow different time translations: a phase lag of the heat flux τ_q and a phase lag of temperature gradient τ_θ. A Taylor series approximation of the modified Fourier law, together with the remaining field equations leads to a complete system of equations describing a DPL thermoelastic model. The model transmits thermoelastic disturbance in a wavelike manner if the approximation is linear with respect to τ_q and τ_θ, and $0 \leq \tau_\theta < \tau_q$; or quadratic in τ_q and linear in τ_θ, with $\tau_q > 0$ and $\tau_\theta > 0$. This theory is developed in a rational way to produce a fully consistent theory which is able to incorporate thermal pulse transmission in a very logical manner. It includes the "thermal displacement gradient" among its independent constitutive variables, and differs from the previous theories in that it does not accommodate dissipation of thermal energy [Ignaczak and Ostoja-Starzewski 2010]. Said and Othman [2017] studied the effect of mechanical force, rotation and moving internal heat source on a two-temperature fiber-reinforced thermoelastic medium with two theories. Abouelregal [2011] applied the DPL heat transfer model for an isotropic solid sphere.

The solution of the problem is carried out when the boundary of the sphere is maintained at constant heat flux and the displacement of the surface is constrained. Abdallah [2009] used the uncoupled thermoelastic model based on the DPL heat conduction equation to investigate the thermoelastic properties of a semi-infinite medium induced by a homogeneously illuminating ultrashort pulsed laser heating. Quintanilla and Jordan [2009] present exact solutions of two initial-boundary value problems in the setting of a recently introduced theory of heat conduction, wherein the two temperature theory of the late 1960s is merged with Tzou's DPL flux relation.

The development of initial stresses in the medium is due to many reasons, for example, resulting from differences of temperature, process of quenching, shot pinning and cold working, slow process of creep, differential external forces, gravity variations, etc. The earth is assumed to be under high initial stresses. It is, therefore, of much interest to study the influence of these stresses on the propagation of stress waves. Biot [1965] showed the acoustic propagation under initial stress, which is fundamentally different from that under a stress-free state. He has obtained the velocities of longitudinal and transverse waves along the coordinate axis only.

The wave propagation in solids under initial stresses has been studied by many authors for various models. The study of the effects of gravitational and hydrostatic initial stress on a two-temperature fiber-reinforced thermoelastic medium for three-phase-lag is due to Said and Othman [2016], Montanaro [1999] investigated the isotropic linear thermoelasticity with hydrostatic initial stress. Abbas and Othman [2012], Othman et al. [2013] and Sarkar et al. [2016] studied the effect of the hydrostatic initial stress, the

gravity and the magnetic field on a fiber-reinforced thermoelastic medium with a fractional derivative heat transfer. Ailawalia et al. [2009] investigated deformation in a generalized thermoelastic medium with hydrostatic initial stress.

In this study, the dual phase lag theory is applied to study the two-dimensional problem of generalized thermoelasticity for a fiber-reinforced thick plate under initial stress and variable thermal conductivity. The problem is solved numerically using a normal mode analysis method. Numerical results for the temperature distribution and the displacement and stress components are given and illustrated graphically. It is found from the graphs that variability thermal conductivity parameter and the initial stress significantly influences the variations of field quantities. This article is a continuation of the work by Abbas and Abd-alla [2011] and Othman and Said [2012] to include the effect of reference temperature on thermal stress distribution.

2. Basic equations

The linear equations governing thermoelastic interactions in a homogeneous transversely isotropic fiber-reinforced solid without any heat sources or body forces with hydrostatic initial stress in the context of generalized thermoelasticity with dual phase lags are given now.

The equation of motion in the absence of body forces can be written as

$$\sigma_{ij,j} + \left(u_{i,k}\,\sigma^0_{kj}\right)_{,j} = \rho \frac{\partial^2 u_i}{\partial t^2}, \tag{1}$$

where σ_{ij} are the components of stress, σ^0_{kj} is the initial stress tensor, ρ is the density, u_i are the components of displacement vector and $i, j, k = 1, 2, 3$. The comma denotes space-coordinate differentiation and the repeated index in the subscript implies summation.

The heat conduction equation corresponding to the DPL model proposed by Tzou [1996] takes the form

$$\left(1 + \tau_\theta \frac{\partial}{\partial t}\right)(K_{ij}\,\theta_{,j})_{,i} = \left(\delta + \tau_q \frac{\partial}{\partial t}\right)\left(\rho C_E \frac{\partial T}{\partial t} + \beta_{ij} T_0\, u_{i,j}\right), \tag{2}$$

where K_{ij} is the thermal conductivity, C_E is the specific heat at constant strain, $\theta = T - T_0$ is the temperature increment of the resonator, in which T_0 is the environmental temperature, assumed to be such as $|(T - T_0)/T| \ll 1$, β_{ij} is the thermal elastic coupling tensor, τ_q is the phase lag of the heat flux, τ_θ is the phase lag of the gradient of temperature where $0 \le \tau_\theta < \tau_q$.

The constitutive equations for a fiber-reinforced linearly elastic anisotropic medium with respect to the reinforcement direction $\boldsymbol{b} \equiv (b_1, b_2, b_3)$, with $b_1^2 + b_2^2 + b_3^2 = 1$ are

$$\sigma_{ij} = \lambda e_{kk}\,\delta_{ij} + 2\mu_T\, e_{ij} + \alpha(b_k b_m e_{km}\delta_{ij} + b_i b_j e_{kk}) + 2(\mu_L - \mu_T)(b_k b_i e_{kj} + b_k b_j e_{ki}) + \beta b_k b_m e_{km} b_i b_j - \beta_{ij}(T - T_0), \tag{3}$$

where e_{ij} are the components of strain, λ, μ_T are the elastic constants, α, β, $\mu_L - \mu_T$ are the reinforcement parameters, and δ_{ij} is Kronecker's delta.

Strain-displacement relations

$$e_{ij} = \tfrac{1}{2}(u_{i,j} + u_{j,i}). \tag{4}$$

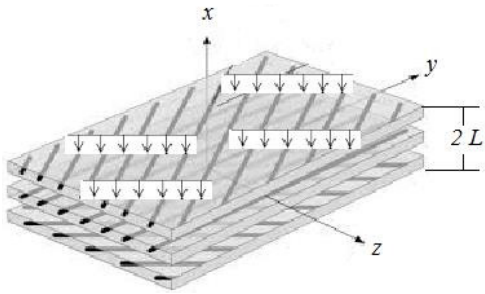

Figure 1. Geometry of the problem.

In physics, thermal conductivity is the property of a material's ability to conduct heat. It appears primarily in Fourier's law for heat conduction. Thermal conductivity is measured in watt per Kelvin per meter ($\mathrm{W\,K^{-1}\,m^{-1}}$) multiplied by a temperature difference and an area, and divided by a thickness, the thermal conductivity predicts the rate of energy loss through a piece of material. In the window building industry "thermal conductivity" is expressed as the U-Factor, which measures the rate of heat transfer and tells you how well the window insulates.

3. Formulation of the problem

In the present paper, we consider an infinite thick plate with traction free surfaces at $x = \pm L$ (layer of thickness $2L$), which consists of homogeneous, transversely isotropic thermoelastic material. We take the origin of the coordinate system (x, y, z) on the middle surface of the layer. The $x - y$ plane is chosen to coincide with the middle surface and y axis normal to it along the thickness. Then the components of the displacement vector and temperature are independent of z and can be taken in the following forms

$$u = u(x, y, t), \qquad v = v(x, y, t), \qquad w = 0, \qquad \theta = \theta(x, y, t). \tag{5}$$

The constitutive relations and field equations with an initial stress and without body forces and heat sources in the present case are

$$\sigma_{xx} = (\lambda + 2\alpha + 4\mu_L - 2\mu_T + \beta)\frac{\partial u}{\partial x} + (\lambda + \alpha)\frac{\partial v}{\partial y} - \beta_{11}(T - T_0), \tag{6}$$

$$\sigma_{yy} = (\lambda + 2\mu_T)\frac{\partial v}{\partial y} + (\lambda + \alpha)\frac{\partial u}{\partial x} - \beta_{22}(T - T_0), \tag{7}$$

$$\sigma_{xy} = \mu_L\Big(\frac{\partial v}{\partial x} + \frac{\partial u}{\partial y}\Big), \tag{8}$$

where $\boldsymbol{b}$ is chosen so that its components are $(1, 0, 0)$.

The equations of motion along x and y directions can be obtained as

$$[\lambda + 2(\alpha + \mu_T) + 4(\mu_L - \mu_T) + \beta + \sigma_0]\frac{\partial^2 u}{\partial x^2} + (\sigma_0 + \mu_L)\frac{\partial^2 u}{\partial y^2} + (\alpha + \lambda + \mu_L)\frac{\partial^2 v}{\partial x\,\partial y} - \beta_{11}\frac{\partial T}{\partial x} = \rho\frac{\partial^2 u}{\partial t^2}, \tag{9}$$

$$(\lambda + 2\mu_T + \sigma_0)\frac{\partial^2 v}{\partial y^2} + (\sigma_0 + \mu_L)\frac{\partial^2 v}{\partial x^2} + (\alpha + \lambda + \mu_L)\frac{\partial^2 u}{\partial x\,\partial y} - \beta_{22}\frac{\partial T}{\partial y} = \rho\frac{\partial^2 v}{\partial t^2}, \tag{10}$$

where σ_0 is the initial pressure and

$$\beta_{11} = (2\lambda + 3\alpha + 4\mu_L - 2\mu_T + \beta)\alpha_{11} + (\lambda + \alpha)\alpha_{22}, \qquad \beta_{22} = (2\lambda + \alpha)\alpha_{11} + (\lambda + 2\mu_T)\alpha_{22}. \quad (11)$$

The heat equation can be written as

$$\left(1 + \tau_\theta \frac{\partial}{\partial t}\right)\left[\frac{\partial}{\partial x}\left(K_{11}\frac{\partial \theta}{\partial x}\right) + \frac{\partial}{\partial y}\left(K_{22}\frac{\partial \theta}{\partial y}\right)\right] = \left(\delta + \tau_q \frac{\partial}{\partial t}\right)\left[\rho C_E \frac{\partial \theta}{\partial t} + T_0 \frac{\partial}{\partial t}\left(\beta_{11}\frac{\partial u}{\partial x} + \beta_{22}\frac{\partial v}{\partial y}\right)\right]. \quad (12)$$

Modern structural elements are often subjected to temperature changes of such magnitude that their material properties may no longer be regarded as having constant values even in an approximate sense. The thermal and mechanical properties of materials vary with temperature, so that the temperature dependence of material properties must be taken into consideration in the thermal stress analysis of these elements. In physics, thermal conductivity is the property of a material to conduct heat. It is evaluated primarily in terms of Fourier's law for heat conduction. Heat transfer occurs at a higher rate across materials of higher thermal conductivity than across materials of low thermal conductivity. Generally, thermal conductivity of materials is temperature dependent.

Our goal is to investigate the effect of temperature dependency of thermal conductivity keeping the other elastic and thermal parameter constants; therefore we assume the thermal conductivities and thermal diffusivity are assumed to vary linearly with temperature according to

$$K_{11} = K_{11}(\theta) = K_{01}(1+K_1\theta), \;\; K_{22} = K_{22}(\theta) = K_{02}(1+K_1\theta), \;\; \rho C_E = \rho C_E(\theta) = \rho_0 C_{E0}(1+K_1\theta), \quad (13)$$

where K_{01}, K_{02}, ρ_0 and C_{E0} are considered constants, in case of temperature-independent modulus of elasticity $K_1 = 0$.

Now, using the mapping [Tzou 1996]:

$$\psi = \int_0^\theta (1 + K_1\xi)\,\mathrm{d}\xi, \quad (14)$$

where ψ is a new function expressing the heat conduction.

From (14), we get

$$\psi = \theta\left(1 + \tfrac{1}{2}K_1\theta\right). \quad (15)$$

Differentiating (15) with respect to x and y, we obtain

$$K_{01}\frac{\partial \psi}{\partial x} = K_{11}(\theta)\frac{\partial \theta}{\partial x}, \qquad K_{02}\frac{\partial \psi}{\partial y} = K_{22}(\theta)\frac{\partial \theta}{\partial y}. \quad (16)$$

With the same manner, by differentiating the mapping with respect to time t, we have

$$\rho_0 C_{E0}\frac{\partial \psi}{\partial t} = \rho C_E \frac{\partial \theta}{\partial t}. \quad (17)$$

Using (16) and (17), the modified model of heat equation will take the form

$$\left(1 + \tau_q \frac{\partial}{\partial t}\right)\left[\rho_0 C_{E0}\frac{\partial \psi}{\partial t} + T_0 \frac{\partial}{\partial t}\left(\beta_{11}\frac{\partial u}{\partial x} + \beta_{22}\frac{\partial v}{\partial y}\right)\right] = \left(1 + \tau_\theta \frac{\partial}{\partial t}\right)\left[K_{01}\frac{\partial^2 \psi}{\partial x^2} + K_{02}\frac{\partial^2 \psi}{\partial y^2}\right]. \quad (18)$$

For simplification, we shall use the following nondimensional variables:

$$x' = c_0\eta x, \qquad y' = c_0\eta y, \qquad u' = c_0\eta u, \qquad v' = c_0\eta v, \qquad t' = c_0^2\eta t,$$
$$\sigma_0' = \frac{\sigma_0}{\rho_0 c_0^2}, \qquad \sigma_{ij}' = \frac{\sigma_{ij}}{\rho_0 c_0^2}, \qquad \tau_q' = c_0^2\eta\tau_q, \qquad \tau_\theta' = c_0^2\eta\tau_\theta, \qquad \psi' = \frac{\beta_{11}\psi}{\rho_0 c_0^2}. \tag{19}$$

where,

$$c_0^2 = \frac{A_{11}}{\rho_0}, \qquad A_{11} = \lambda + 2(\alpha + \mu_T) + 4(\mu_L - \mu_T) + \beta, \qquad \eta = \frac{\rho_0 C_{E0}}{K_{01}}.$$

The thermal property variations are assumed to be small and the approximate symmetries of the equation are calculated. A linear functional variation is assumed for the thermal properties and a similarity solution is constructed. For linearity, such that $|\theta/T_0| \ll 1$, then equations of motion, with the help of (16), may be recast into the dimensionless form after suppressing the primes as

$$(1+\sigma_0)\frac{\partial^2 u}{\partial x^2} + (\sigma_0 + B_4)\frac{\partial^2 u}{\partial y^2} + (B_1 + B_4)\frac{\partial^2 v}{\partial x\,\partial y} - \frac{\partial \psi}{\partial x} = \frac{\partial^2 u}{\partial t^2}, \tag{20}$$

$$(B_2+\sigma_0)\frac{\partial^2 v}{\partial y^2} + (\sigma_0 + B_4)\frac{\partial^2 v}{\partial x^2} + (B_1 + B_4)\frac{\partial^2 u}{\partial x\,\partial y} - B_3\frac{\partial \psi}{\partial y} = \frac{\partial^2 v}{\partial t^2}, \tag{21}$$

$$\left(1 + \tau_\theta \frac{\partial}{\partial t}\right)\left(\frac{\partial^2 \psi}{\partial x^2} + \varepsilon_1 \frac{\partial^2 \psi}{\partial y^2}\right) = \left(\delta + \tau_q \frac{\partial}{\partial t}\right)\left[\frac{\partial \psi}{\partial t} + \frac{\partial}{\partial t}\left(\varepsilon_2 \frac{\partial u}{\partial x} + \varepsilon_3 \frac{\partial v}{\partial y}\right)\right]. \tag{22}$$

The constitutive relations given in (1) in dimensionless forms and for linearity take the form

$$\sigma_{xx} = \frac{\partial u}{\partial x} + B_1 \frac{\partial v}{\partial y} - \psi, \tag{23}$$

$$\sigma_{xy} = B_4\left(\frac{\partial u}{\partial y} + \frac{\partial v}{\partial x}\right), \tag{24}$$

where

$$B_1 = \frac{A_{12}}{A_{11}}, \quad B_2 = \frac{A_{22}}{A_{11}}, \quad B_3 = \frac{\beta_{22}}{\beta_{11}}, \quad B_4 = \frac{\mu_L}{A_{11}}, \quad A_{12} = \alpha + \lambda, \quad A_{22} = \lambda + 2\mu_T,$$
$$\varepsilon_1 = \frac{K_{02}}{K_{01}}, \quad \varepsilon_2 = \frac{\beta_{11}^2 T_0}{\rho_0 C_{E0} A_{11}}, \quad \varepsilon_3 = \frac{\beta_{11}\beta_{22} T_0}{\rho_0 C_{E0} A_{11}}.$$

4. Normal mode analysis

The normal mode analysis gives exact solutions without any assumed restrictions on the temperature, displacement, and stress distributions. It is applied to a wide range of problems in different branches. It can be applied to boundary-layer problems, which are described by the linearized Navier–Stokes equations in electro-hydro-dynamics. The normal mode analysis is, in fact, to look for the solution in the Fourier transformed domain, assuming that all the field quantities are sufficiently smooth on the real line so that the normal mode analysis of these functions exists. The normal mode expansion method has been proposed by Cheng et al. [2000] for modeling the thermoelastic generation process of elastic waveforms in an isotropic plate.

The solution of the considered physical variable can be decomposed in terms of normal modes as the following form

$$[u, v, \psi, \sigma_{ij}](x, y, t) = \left[u^*, v^*, \psi^*, \sigma_{ij}^*\right](x)\, e^{\omega t + iay}, \tag{25}$$

where ω is the (complex) frequency constant, $i = \sqrt{-1}$, a is the wave number in the y direction, and $u^*(x)$, $v^*(x)$, $\psi^*(x)$ and $\sigma_{ij}^*(x)$ are the amplitudes of the field quantities.

Using (25), (20)–(24) take the forms

$$\left(\frac{d^2}{dx^2} - g_1\right)u^* + g_2\frac{dv^*}{dx} = g_3\frac{d\psi^*}{dx}, \tag{26}$$

$$\left(\frac{d^2}{dx^2} - g_4\right)v^* + g_5\frac{du^*}{dx} = g_6\psi^*, \tag{27}$$

$$\left(\frac{d^2}{dx^2} - g_7\right)\psi^* = g_8\frac{du^*}{dx} + g_9 v^*, \tag{28}$$

$$\sigma_{xx}^* = \frac{du^*}{dx} + iaB_1 v^* - \psi^*, \tag{29}$$

$$\sigma_{xy}^* = B_4\left(iau^* + \frac{dv^*}{dx}\right), \tag{30}$$

where

$$g_1 = \frac{a^2(\sigma_0+B_4)}{1+\sigma_0}+\frac{\omega^2}{1+\sigma_0},\ g_2 = \frac{ia(B_1+B_4)}{1+\sigma_0},\ g_3 = \frac{1}{1+\sigma_0},\ g_4 = \frac{a^2(\sigma_0+B_2)+\omega^2}{\sigma_0+B_4},$$
$$g_5 = \frac{ia(B_1+B_4)}{\sigma_0+B_4},\ g_6 = \frac{iaB_3}{\sigma_0+B_4},\ g_7 = a^2\varepsilon_1+\frac{\omega(\delta+\tau_q\omega)}{1+\tau_\theta\omega},\ g_8 = \frac{\varepsilon_2\omega(\delta+\tau_q\omega)}{1+\tau_\theta\omega},\ g_9 = \frac{ia\varepsilon_3\omega(\delta+\tau_q\omega)}{1+\tau_\theta\omega}.$$

Eliminating $\psi^*(x)$ and $v^*(x)$ in (26)–(28), one obtains

$$\left(\mathrm{D}^6 - A\mathrm{D}^4 + B\mathrm{D}^2 - C\right)u^*(x) = 0, \tag{31}$$

where

$$\mathrm{D} = \frac{d}{dx}, \quad A = g_3 g_8 + g_2 g_5 + g_1 + g_4 + g_7,$$
$$B = g_2 g_5 g_7 + g_2 g_6 g_8 + g_3 g_4 g_8 + g_1 g_4 + g_1 g_7 + g_4 g_7 - g_6 g_9 + g_3 g_5 g_9, \quad C = g_1 g_4 g_7 - g_1 g_6 g_9.$$

Equation (31) can be factorized as

$$\left(\mathrm{D}^2 - k_1^2\right)\left(\mathrm{D}^2 - k_2^2\right)\left(\mathrm{D}^2 - k_3^2\right)u^*(x) = 0, \tag{32}$$

where k_n^2 $(n = 1, 2, 3)$ are the roots of the following characteristic equation:

$$k^6 - Ak^4 + Bk^2 - C = 0. \tag{33}$$

The solution of (31), bound at $x \to \infty$, is given by

$$u^*(x) = \sum_{n=1}^{3} M_{1n}\, e^{-k_n x}. \tag{34}$$

In a similar manner, one gets

$$\psi^*(x) = \sum_{n=1}^{3} H_{1n} M_{1n}\, e^{-k_n x}, \quad v^*(x) = \sum_{n=1}^{3} H_{2n} M_{1n}\, e^{-k_n x}, \tag{35}$$

where

$$H_{1n} = \frac{(g_5 g_9 + g_4 g_8)k_n - g_8 k_n^3}{k_n^4 - (g_4 + g_7)k_n^2 + (g_4 g_7 - g_6 g_9)}, \qquad H_{2n} = \frac{g_8 k_n + (k_n^2 - g_7)H_{1n}}{g_9}.$$

Introducing (34)–(35) into (29) and (30), we obtain

$$\sigma_{xx}^* = \sum_{n=1}^{3} H_{3n} M_{1n} e^{-k_n x}, \quad \sigma_{xy}^* = \sum_{n=1}^{3} H_{4n} M_{1n} e^{-k_n x}, \tag{36}$$

where $H_{3n} = -k_n + \mathrm{i}a B_1 H_{2n} - H_{1n}$, $H_{4n} = B_4(\mathrm{i}a - k_n H_{3n})$.

5. Boundary conditions

In this section we determine the parameters M_{1n} $(n = 1, 2, 3)$. In the physical problem, we should suppress the positive exponentials that are unbounded at infinity. The constants M_{11}, M_{12}, M_{13} have to be chosen such that the boundary conditions on the surface at $x = L$ take the form

$$\sigma_{xx}(L, y, t) = -P_1 f, \qquad \sigma_{xy}(L, y, t) = 0, \qquad \psi(L, y, t) = P_3, \tag{37}$$

where f is constant, P_1 is the magnitude of a hydrostatic initial stress and $P_3 = P_2 + \frac{1}{2}K_1 P_2^2$. If $P_2 = 0$, we obtain the corresponding expressions for normal force applied on the plane surface. If we put $P_1 = 0$, then the corresponding expressions yield the results for thermal sources.

Substituting the expressions of the variables considered into the above boundary conditions, we obtain

$$\psi^*|_{x=L} = \sum_{n=1}^{3} H_{1n} M_{1n} e^{-k_n x} = P_3^*, \tag{38}$$

$$\sigma_{xx}^*|_{x=L} = \sum_{n=1}^{3} H_{3n} M_{1n} e^{-k_n x} = -P_1^*, \tag{39}$$

$$\sigma_{xy}^*|_{x=L} = \sum_{n=1}^{3} H_{4n} M_{1n} e^{-k_n x} = 0, \tag{40}$$

where $P_1^* = P_1 e^{-(\omega t + \mathrm{i}ay)}$, $P_3^* = P_3 e^{-(\omega t + \mathrm{i}ay)}$.

Solving the above system of (38)–(40), we obtain a system of three equations. After applying the inverse of the matrix method, we have the values of the three constants M_{1n} $(n = 1, 2, 3)$. Hence, we obtain the expressions for the displacements, the temperature distribution, and other physical quantities:

$$\begin{pmatrix} M_{11} \\ M_{12} \\ M_{13} \end{pmatrix} = \begin{pmatrix} H_{11} e^{-k_1 L} & H_{12} e^{-k_2 L} & H_{13} e^{-k_3 L} \\ H_{31} e^{-k_1 L} & H_{32} e^{-k_2 L} & H_{33} e^{-k_3 L} \\ H_{41} e^{-k_1 L} & H_{42} e^{-k_2 L} & H_{43} e^{-k_3 L} \end{pmatrix}^{-1} \begin{pmatrix} P_3^* \\ -P_1^* \\ 0 \end{pmatrix}. \tag{41}$$

After obtaining ψ, the temperature increment θ can be obtained by solving (15) to give

$$\theta = \frac{-1 + \sqrt{1 + 2K_1\psi}}{K_1}. \tag{42}$$

6. Particular cases

(1) Generalized thermoelastic medium with hydrostatic initial stress and with temperature-dependent thermal conductivity from above equations with $\mu_L = \mu_T = \mu,\ \alpha = \beta = 0$.

(2) Fiber-reinforced generalized thermoelastic medium without hydrostatic initial stress and with temperature-dependent thermal conductivity from above equations with $P_1 = \sigma_0 = 0$.

(3) Fiber-reinforced generalized thermoelastic medium without temperature-dependent thermal conductivity from above equations with $K_1 = 0$.

(4) Equation of coupled thermoelasticity (CD theory) when $\tau_\theta = \tau_q = 0,\ \delta = 1$.

(5) Lord–Shulman theory (LS theory) $\tau_\theta = 0,\ \delta = 1,\ \tau_q > 0$.

(6) Green–Naghdi theory (GN II theory) when $\tau_\theta = 0,\ \delta = 0,\ \tau_q = 1$.

(7) Equations of generalized thermoelasticity with phase lags (DPL theory) when $\delta = 1,\ \tau_q \geq \tau_\theta > 0$.

7. Numerical results

In order to illustrate the theoretical results obtained in the preceding section and to compare these in the context of the DPL model, the CD theory and the LS theory, we now present some numerical results for the physical constants as $\lambda = 3.76 \cdot 10^9\,\mathrm{N/m^2}$, $\mu_T = 1.89 \cdot 10^{10}\,\mathrm{N/m^2}$, $\mu_L = 2.45 \cdot 10^{10}\,\mathrm{N/m^2}$, $\alpha = -1.28 \cdot 10^{10}\,\mathrm{N/m^2}$, $\beta = 0.32 \cdot\,\mathrm{N/m^2}$, $\tau_q = 0.95\,\mathrm{s}$, $C_{E0} = 23.1\,\mathrm{J/(kg\,K)}$, $\rho_0 = 7800\,\mathrm{kg/m^3}$, $\mu = 3.86 \cdot 10^{10}\,\mathrm{N/m^2}$, $\alpha_{11} = 1.7 \cdot 10^{-5}\,\mathrm{K^{-1}}$, $\alpha_{22} = 1.5 \cdot 10^{-5}\,\mathrm{K^{-1}}$, $\tau_\theta = 0.8\,\mathrm{s}$, $K_{01} = 9.21 \cdot 10^5\,\mathrm{J/(ms\,K)}$, $K_{02} = 9.63 \cdot 10^5\,\mathrm{J/(ms\,K)}$, $\omega = \omega_0 + i\xi$, $\omega_0 = 0.6$, $\xi = 0.2$, $a = 0.5$, $P_1 = 30$, $L = 0.1\,\mathrm{m}$, $T_0 = 293\,\mathrm{K}$, $K_1 = -5$, $f = 1$, $P_2 = 0.5$, $\sigma_0 = 1.45 \cdot 10^8\,\mathrm{N/m^2}$, $\alpha_t = 1.78 \cdot 10^{-5}\,\mathrm{K^{-1}}$, $P = 0.5$.

The computations were carried out for a value of time $t = 0.3$. The variations of the thermal temperature θ, the horizontal displacement u, and the stress components σ_{xx}, σ_{xy} with distance x for the value of y, namely $y = 1.5$, were substituted in performing the computation. The results are shown in Figures 2–12. The graphs show the six curves predicted by three different theories of thermoelasticity. In these figures, the solid line represents the solution in the coupled theory, the dotted line represents the solution in the generalized LS theory, and the dashed line represents the solution derived using the DPL model. Here all the variables are taken in nondimensional forms and the physical quantities depend not only on space x and time t, but also on phase lags τ_θ and τ_q.

Figures 2–5 show comparisons between the horizontal displacement components u, the thermal temperature θ and the stress components σ_{xx}, σ_{xy} with temperature-dependent and temperature-independent thermal conductivity. Figure 2 depicts that the distribution of the horizontal displacement u begins from positive values. In the context of the three theories, u starts with decreasing, then increases, and again decreases. The values of u, increasing with the temperature-dependent thermal conductivity in the first and then, decrease. It is clear from Figure 3 that the thermal temperature θ begins from negative values with temperature-dependent thermal conductivity, but it begins from positive values with temperature-independent thermal conductivity and satisfies the boundary condition at $x = 0.1$. In the context of the three theories with temperature-dependent thermal conductivity, θ increases in the range $0 \leq x \leq 6$, but with the temperature-independent thermal conductivity, θ decreases in the range $0 \leq x \leq 6$. The values

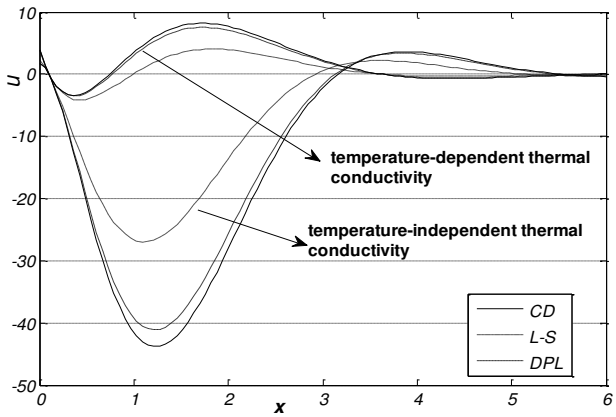

Figure 2. Horizontal displacement distribution u with temperature-dependent and temperature-independent thermal conductivity.

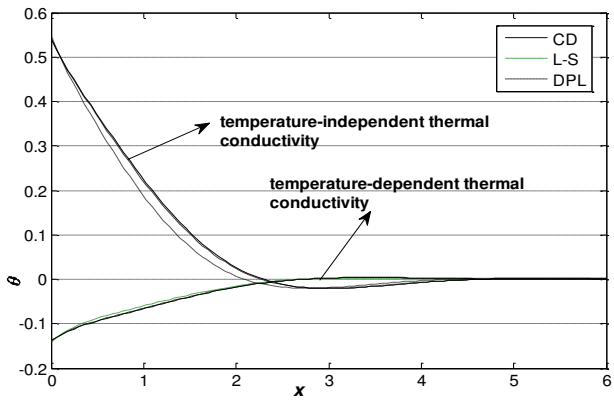

Figure 3. Thermal temperature distribution θ with temperature-dependent and temperature-independent thermal conductivity.

of θ decrease and then increasing with temperature-dependent thermal conductivity. Therefore, the effect of temperature-dependent thermal conductivity should be taken into consideration.

Figure 4 displays that the distribution of the stress component σ_{xx} begins from negative values and satisfies the boundary condition at $x = 0.1$. In the context of the three theories with temperature-dependent thermal conductivity, σ_{xx} starts with increasing, then decreases, and again increases. However, the context of the three theories with temperature-independent thermal conductivity, σ_{xx} starts with decreasing to a minimum value, then increases to a maximum value, and again decreases. The temperature-dependent thermal conductivity increase, then decrease, and last increase values of σ_{xx}. Figure 5 shows the distribution of the stress component σ_{xy} and demonstrates that it reaches a zero value and satisfies the boundary condition at $x = 0.1$. In the context of the three theories with temperature-dependent thermal conductivity, σ_{xy} starts with increasing, and then decreases.

However, in the context of the three theories with temperature-independent thermal conductivity, σ_{xy} starts with decreasing to a minimum value, then increase to a maximum value, and again decreases. The

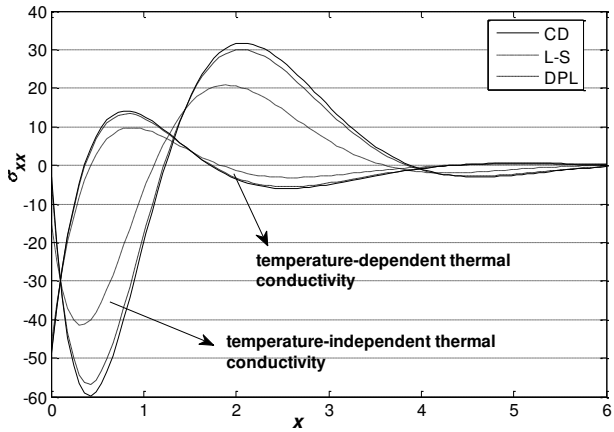

Figure 4. Distribution of stress component σ_{xx} with temperature-dependent and temperature-independent thermal conductivity.

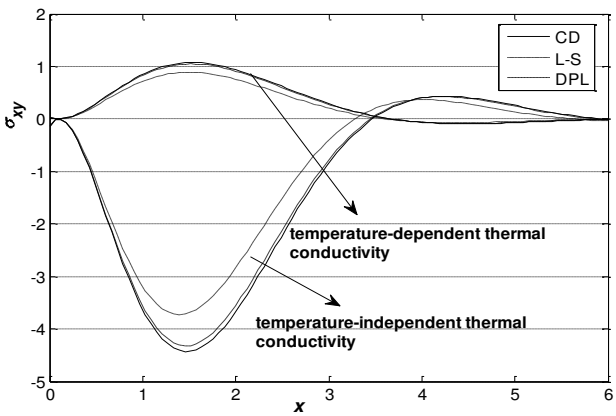

Figure 5. Distribution of stress component σ_{xy} with temperature-dependent and temperature-independent thermal conductivity.

values of σ_{xy} increase and then, decrease with temperature-dependent thermal conductivity. Figures 2–5 demonstrate that the temperature-dependent thermal conductivity has a significant role on all the physical quantities. The result provides a motivation to investigate the thermoelastic materials with temperature-dependent thermal conductivity as a new class of applications thermoelastic materials.

Also, the results obtained in this case should be useful for physicists, researchers in material science, designers of new materials as well as for those working on the development of thermal stresses and in practical situations as in optics, geophysics, geomagnetic, acoustics and oil prospecting.

Figures 6–9 show comparisons between the horizontal displacement components u, the thermal temperature θ, and the stress components σ_{xx}, σ_{xy} with and without the initial stress. Figure 6 depicts that the distribution of the horizontal displacement u begins from positive values. In the context of the three theories without initial stress, u decreases in the range $0 \leq x \leq 6$. The values of u increase with initial stress in the first and then decrease. It is clear from Figure 7 that the thermal temperature θ begins

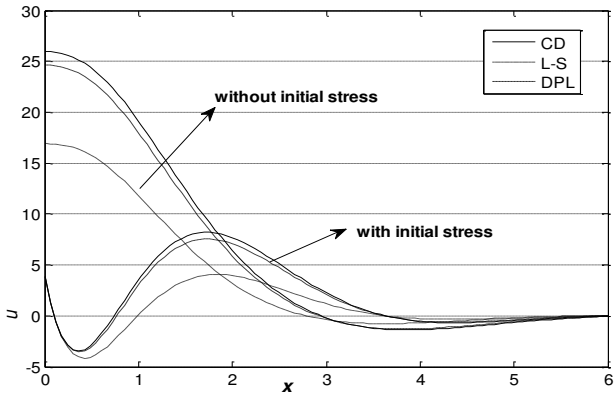

Figure 6. Horizontal displacement distribution u with initial stress and without initial stress.

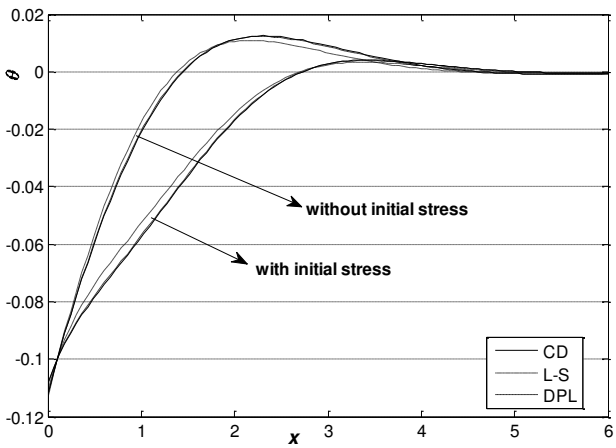

Figure 7. Thermal temperature distribution θ with initial stress and without initial stress.

from negative values and satisfies the boundary condition at $x = 0.1$. In the context of the three theories with without initial stress, θ increases in the range $0 \leq x \leq 6$. The values of θ decrease with initial stress. Figure 8 displays that the distribution of the stress component σ_{xx} begins from negative values and satisfies the boundary condition at $x = 0.1$. In the context of the three theories without initial stress, σ_{xx} starts with decreasing to a minimum value, and then increases. The initial stress, decrease, then increase, and last decrease values of σ_{xx}. Figure 9 shows the distribution of the stress component σ_{xy}, and demonstrates that it reaches a zero value and satisfies the boundary condition at $x = 0.1$. In the context of the three theories without initial stress, σ_{xy} starts with decreasing to a minimum value, and then increases. The initial stress increase and then decrease values of σ_{xy}. Figures 6–9 demonstrate that the initial stress has a significant role on all the physical quantities. Figures 10–12 show that the values of horizontal displacement components u, and the stress components σ_{xx}, σ_{xy} increase and then, decrease with reinforcement.

Due to the presence of reinforcement and initial stress, the magnitude of the thermophysical quantities

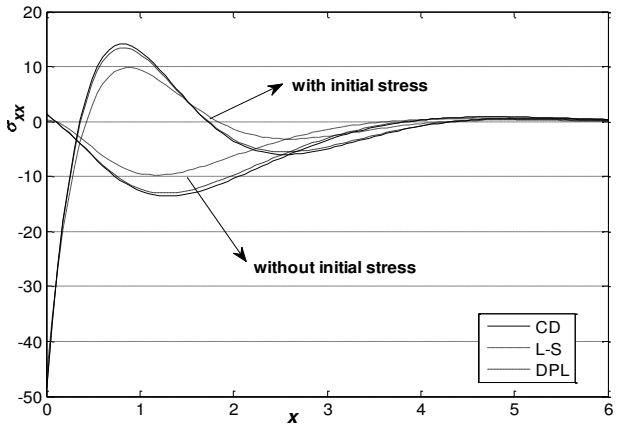

Figure 8. Distribution of stress component σ_{xx} with initial stress and without initial stress.

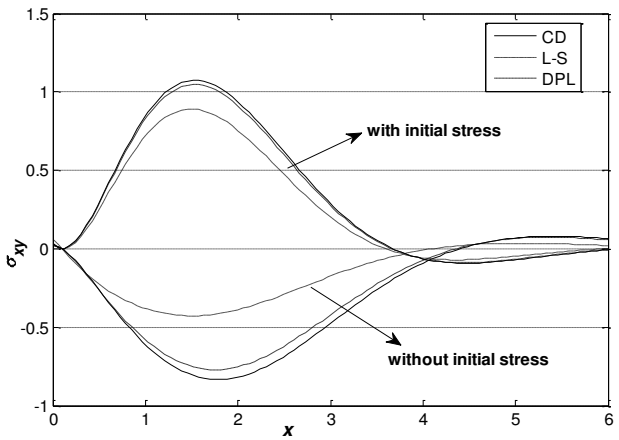

Figure 9. Distribution of stress component σ_{xy} with initial stress and without initial stress.

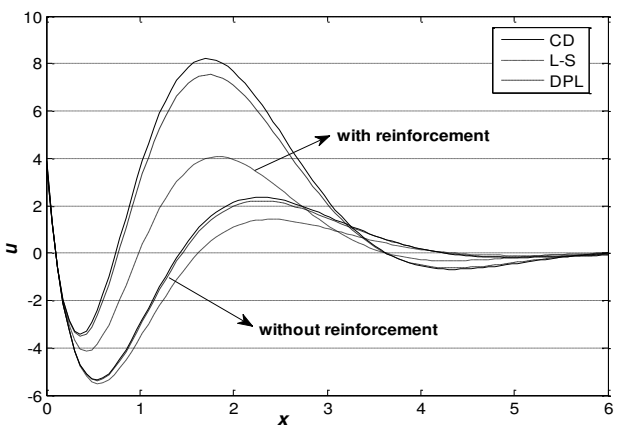

Figure 10. Horizontal displacement distribution u with and without reinforcement.

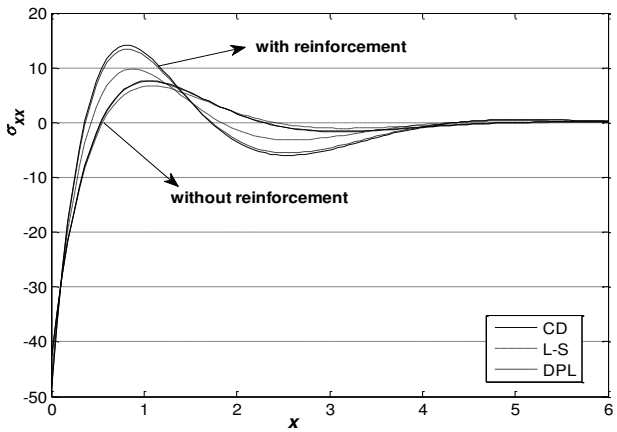

Figure 11. Distribution of stress component σ_{xx} with and without reinforcement.

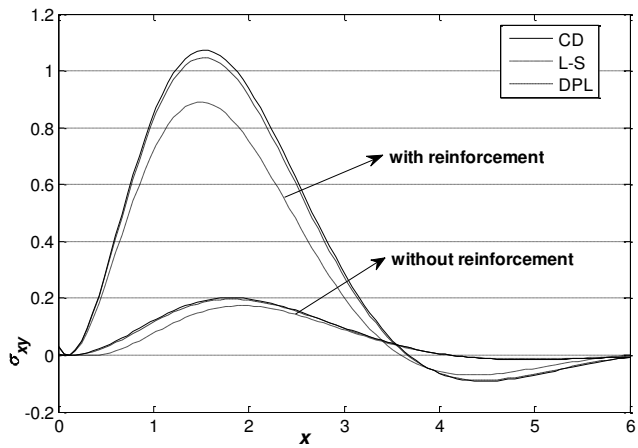

Figure 12. Distribution of stress component σ_{xy} with and without reinforcement.

decay, which indicates that initial stress and reinforcement have a tendency in maintaining the smoothness of the profiles of the thermophysical quantities. So it is more advantageous to consider the effect of initial stress and reinforcement in such problems of engineering.

In addition, for a fiber-reinforced generalized thermoelastic medium without temperature-dependent thermal conductivity ($K_1 = 0$) the results agree with the existing literature [Abbas and Abd-alla 2011].

8. Conclusion

In the present study, normal mode analysis is used to study the effect of the initial stress and temperature-dependent thermal conductivity on fiber-reinforced generalized thermoelastic medium based on the DPL theory, CD theory and the LS theory. We obtain the following conclusions based on the above analysis:

(1) It is clear that the initial stress, temperature-dependent thermal conductivity, and the reinforcement play significant roles on all the physical quantities.

(2) The phase lags τ_q and τ_θ has great influence on the distribution of all physical quantities.

(3) The curves in the context of the DPL model, CD theory and the LS theory, decrease exponentially with increasing x; this indicates that the thermoelastic waves are unattenuated and nondispersive, while purely thermoelastic waves undergo both attenuation and dispersion.

(4) Deformation of a generalized thermoelastic medium depends on the nature of the applied force as well as the type of boundary conditions.

(5) Analytical solutions based upon normal mode analysis of the thermoelastic problem in solids have been developed and utilized.

The results carried out in this paper can be used to design various fiber reinforced anisotropic media with initial stress in order to meet special engineering requirements.

References

[Abbas and Abd-alla 2011] I. A. Abbas and A. N. Abd-alla, "Effect of initial stress on a fiber-reinforced anisotropic thermoelastic thick plate", *Int. J. Thermophys.* **32**:5 (2011), 1098–1110.

[Abbas and Othman 2012] I. A. Abbas and M. I. A. Othman, "Generalized thermoelastic interaction in a fiber-reinforced anisotropic half-space under hydrostatic initial stress", *J. Vib. Control* **18**:2 (2012), 175–182.

[Abbas et al. 2011] I. A. Abbas, A. N. Abd-alla, and M. I. A. Othman, "Generalized magneto-thermoelasticity in a fiber-reinforced anisotropic half-space", *Int. J. Thermophys.* **32**:5 (2011), 1071–1085.

[Abdallah 2009] I. A. Abdallah, "Dual phase lag heat conduction and thermoelastic properties of a semi-infinite medium induced by ultrashort pulsed laser", *Prog. Phys.* **3** (2009), 60–63.

[Abouelregal 2011] A. E. Abouelregal, "Generalized thermoelasticity for an isotropic solid sphere in dual-phase-lag of heat transfer with surface heat flux", *Int. J. Comput. Methods Eng. Sci. Mech.* **12**:2 (2011), 96–105.

[Ailawalia and Budhiraja 2011] P. Ailawalia and S. Budhiraja, "Fibre-reinforced generalized thermoelastic medium under hydrostatic initial stress", *Engineering* **3**:6 (2011), 622–631.

[Ailawalia et al. 2009] P. Ailawalia, S. Kumar, and G. Khurana, "Deformation in a generalized thermoelastic medium with hydrostatic initial stress subjected to different sources", *Mech. Mech. Eng.* **13**:1 (2009), 5–24.

[Belfield et al. 1983] A. J. Belfield, T. G. Rogers, and A. J. M. Spencer, "Stress in elastic plates reinforced by fibres lying in concentric circles", *J. Mech. Phys. Solids* **31**:1 (1983), 25–54.

[Biot 1956] M. A. Biot, "Thermoelasticity and irreversible thermodynamics", *J. Appl. Phys.* **27**:3 (1956), 240–253.

[Biot 1965] M. A. Biot, *Mechanics of incremental deformations*, Wiley, New York, 1965.

[Chandrasekharaiah 1986] D. S. Chandrasekharaiah, "Thermoelasticity with second sound: a review", *Appl. Mech. Rev.* (*ASME*) **39**:3 (1986), 355–376.

[Cheng et al. 2000] J. C. Cheng, T. H. Wang, and S. Y. Zhang, "Normal mode expansion method for laser-generated ultrasonic Lamb waves in orthotropic thin plates", *Appl. Phys. B* **70**:1 (2000), 57–63.

[Green and Lindsay 1972] A. E. Green and K. A. Lindsay, "Thermoelasticity", *J. Elasticity* **2**:1 (1972), 1–7.

[Green and Naghdi 1993] A. E. Green and P. M. Naghdi, "Thermoelasticity without energy dissipation", *J. Elasticity* **31**:3 (1993), 189–208.

[Hashin and Rosen 1964] Z. Hashin and B. W. Rosen, "The elastic moduli of fiber-reinforced materials", *J. Appl. Mech.* (*ASME*) **31**:2 (1964), 223–232.

[Ignaczak and Ostoja-Starzewski 2010] J. Ignaczak and M. Ostoja-Starzewski, *Thermoelasticity with finite wave speeds*, Oxford University Press, New York, 2010.

[Lord and Shulman 1967] H. W. Lord and Y. Shulman, "A generalized dynamical theory of thermoelasticity", *J. Mech. Phys. Solids* **15**:5 (1967), 299–309.

[Montanaro 1999] A. Montanaro, "On singular surfaces in isotropic linear thermoelasticity with initial stress", *J. Acoust. Soc. Am.* **106**:3 (1999), 1586–1588.

[Nowacki 1975] W. Nowacki, *Dynamic problems of thermoelasticity*, Noordhoff, Leyden, The Netherlands, 1975.

[Nowacki 1986] W. Nowacki, *Thermoelasticity*, 2nd ed., Pergamon Press, Oxford, 1986.

[Othman and Abbas 2011] M. I. A. Othman and I. A. Abbas, "Effect of rotation on plane waves at the free surface of a fibre-reinforced thermoelastic half-space using the finite element method", *Meccanica* (*Milano*) **46**:2 (2011), 413–421.

[Othman and Said 2012] M. I. A. Othman and S. M. Said, "The effect of rotation on two-dimensional problem of a fibre-reinforced thermoelastic with one relaxation time", *Int. J. Thermophys.* **33**:1 (2012), 160–171.

[Othman et al. 2013] M. I. Othman, S. M. Said, and N. Sarker, "Effect of hydrostatic initial stress on a fiber-reinforced thermoelastic medium with fractional derivative heat transfer", *Multidisc. Modeling Mater. Struct.* **9**:3 (2013), 410–426.

[Quintanilla and Jordan 2009] R. Quintanilla and P. M. Jordan, "A note on the two temperature theory with dual-phase-lag delay: some exact solutions", *Mech. Res. Commun.* **36**:7 (2009), 796–803.

[Said and Othman 2016] S. M. Said and M. I. A. Othman, "Effects of gravitational and hydrostatic initial stress on a two-temperature fiber-reinforced thermoelastic medium for three-phase-lag", *J. Solid Mech.* **8**:4 (2016), 806–822.

[Said and Othman 2017] S. M. Said and M. I. A. Othman, "Effect of mechanical force, rotation and moving internal heat source on a two-temperature fiber-reinforced thermoelastic medium with two theories", *Mech. Time-Depend. Mater.* **21**:2 (2017), 245–261.

[Sarkar et al. 2016] N. Sarkar, S. Y. Atwa, and M. I. A. Othman, "The effect of hydrostatic initial stress on the plane waves in a fiber-reinforced magneto-thermoelastic medium with fractional derivative heat transfer", *Int. Appl. Mech.* **52**:2 (2016), 203–216.

[Sengupta and Nath 2001] P. R. Sengupta and S. Nath, "Surface waves in fibre-reinforced anisotropic elastic media", *Sadhana* **26**:4 (2001), 363–370.

[Tzou 1995a] D. Y. Tzou, "A unified field approach for heat conduction from macro- to micro-scales", *J. Heat Transf.* (*ASME*) **117**:1 (1995), 8–16.

[Tzou 1995b] D. Y. Tzou, "Experimental support for the lagging behavior in heat propagation", *J. Thermophys. Heat Transf.* **9**:4 (1995), 686–693.

[Tzou 1996] D. Y. Tzou, *Macro- to microscale heat transfer: the lagging behavior*, Taylor & Francis, Washington, DC, 1996.

[Verma and Rana 1983] P. D. S. Verma and O. H. Rana, "Rotation of a circular cylindrical tube reinforced by fibres lying along helices", *Mech. Mater.* **2**:4 (1983), 353–359.

Received 18 Apr 2018. Revised 23 Mar 2019. Accepted 2 May 2019.

MOHAMED I. A. OTHMAN: m_i_a_othman@yahoo.com
Department of Mathematics, Faculty of Science, Zagazig University, Egypt

AHMED E. ABOUELREGAL: ahabogal@gmail.com
Department of Mathematics, Faculty of Science, Mansoura University, Mansoura, Egypt

and

Department of Mathematics, College of Science and Arts, Aljouf University, El-Qurayat, Saudi Arabia

SAMIA M. SAID: samia_said59@yahoo.com
Department of Mathematics, Faculty of Science, Zagazig University, Zagazig, Egypt

and

Department of Mathematics, Faculty of Science and Arts, Qassim University, Al-mithnab, Saudi Arabia

JOURNAL OF MECHANICS OF MATERIALS AND STRUCTURES
Vol. 14, No. 2, 2019
dx.doi.org/10.2140/jomms.2019.14.295

LARGE DEFLECTIONS AND STABILITY OF SPRING-HINGED CANTILEVER BEAM

MILAN BATISTA

We investigate the influence of spring stiffness on large deflections and the stability of a spring-hinged cantilever subjected to a conservative tip force. Using the closed-form solution of the equilibrium equation and the Jacobi accessory equation, we determine the beam equilibrium forms and their stability. The solution for a spring-hinged cantilever beam subjected to a follower force is provided. The results are presented in graphical and tabular forms.

1. Introduction

The cantilever beam is one of the most commonly used construction elements for mechanical and civil engineering applications. In recent decades, it has also been used in robotics and micro- and nanoengineering applications. Therefore, the large deflection and stability of a cantilever beam has attracted considerable attention. Most studies have focused on the clamped cantilever beam (see [Timoshenko 1961; Frisch-Fay 1962; Ziegler 1977; Popov 1986; Zakharov et al. 2004; Batista 2014; Armanini et al. 2017; Bigoni 2015; O'Reilly 2017; Zhang and Shan 2008]). The spring-hinged cantilever beam, subjected to a conservative force, has not been studied extensively. The stability of a spring-hinged cantilever beam is discussed in the books [Rzhanitsyn 1955; Alfutov 2000], which derive the equation for the buckling force using Euler's method. Rao and Raju [1979] analyzed the postbuckling behavior of the spring-hinged cantilever beam using the finite element method. Ohtsuki and Yasui [1994] solved the large deflection of the spring-hinged cantilever beam under the inclined force using elliptic integrals. These authors experimentally verified their calculations through bending tests. Rao and Raju [2002] calculated the critical load parameter for the cantilever under axial force and distributed load using the semianalytic Rayleigh–Ritz method. There is a difference in opinion for a follower force that might act on the cantilever, particularly for a beam under pure compression [Koiter 1996; Antman 2005; Elishakoff 2005]. Large deflections of a spring-supported cantilever subjected to a follower force were considered using elliptic integrals by Rao et al. [1987]. Rao and Rao [1987] examined the large deflections of a spring-hinged tapered cantilever beam subjected to a rotational distributed loading using Runge–Kutta numerical integration. Shvartsman [2007] considered the large bending of a spring-supported cantilever subjected to a follower force using numerical integration. For the analysis of the stability of the cantilever beam under a follower force using dynamical methods, we refer to [Bolotin 1963; Bigoni et al. 2018] and to [Rao and Rao 1975; Kar and Sujata 1990; Guran and Plaut 1993; Sankaran and Rao 1976] in particular for spring-hinged cantilever beams. For other elastically supported cases of beams, refer to [Simitses and Hodges 2006; Mahnken 2015; Glavardanov et al. 2017].

Keywords: elastic beams, elastic support, large deformations, stability, Jacobi test.

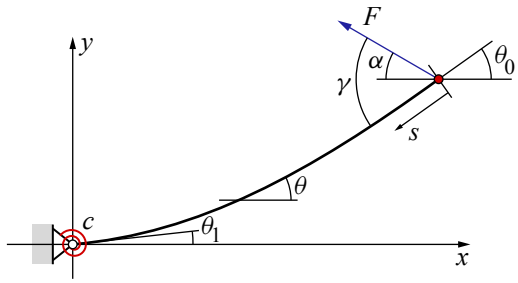

Figure 1. Geometry and load of the spring-hinged cantilever beam.

From the available literature, we conclude that the stability of postbuckling forms of the spring-hinged column beam has not been reported yet. Therefore, in this study, we aim to fill this gap. In the next section, we derive the governing equations of the problem using the principle of minimum total potential energy. The Euler equilibrium equation can be obtained using the first variation of this energy, and its second variation is used to obtain the Jacobi accessory equation [Fox 1954], which is then used to obtain the equilibrium stability. In Section 3, we provide the solution of these equations in terms of the Jacobi elliptic function. Then, in Section 4, we provide some numerical examples and discuss the cantilever under compression in detail. A cantilever subjected to a follower force is discussed in Section 5. Finally, the results are summarized in the last section.

2. Governing equations

We consider an elastic spring-hinged cantilever beam subjected to a force F. The cantilever length is l, its flexural rigidity is EI, the rotational spring stiffness is c, and the force inclination angle is α (Figure 1).

The differential equations of the column base curve are

$$\frac{dx}{ds} = -\cos\theta, \quad \frac{dy}{ds} = -\sin\theta, \tag{1}$$

in which $0 \le s \le \ell$ is the arc length measured from the free end to the fixed end, x and y are the base curve coordinates, and θ is the tangent angle. The conditions at the fixed end are $x(\ell) = y(\ell) = 0$. Using this, from (1), we obtain the coordinates $x_0 \equiv x(0)$ and $y_0 \equiv y(0)$ of the free end as

$$x_0 = \int_0^\ell \cos\theta \, ds, \quad y_0 = \int_0^\ell \sin\theta \, ds. \tag{2}$$

The expression for the cantilever total potential energy Π is

$$\Pi = \int_0^1 \tfrac{1}{2} EI \kappa^2 \, ds - F\cos\alpha(\ell - x_0) - F\sin\alpha \, y_0 + \tfrac{1}{2} c\,\theta_1^2, \tag{3}$$

where $\theta_1 \equiv \theta(\ell)$, and κ is the base curve curvature given by

$$\kappa = -\frac{d\theta}{ds}. \tag{4}$$

For the equilibrium, Π has to be a minimum [Alfutov 2000]. This means that the first variation of Π must vanish, and the second variation of Π must be positive. We derive the governing equations of the problems through the well-known variational procedure [Fox 1954].

The first variation of Π, from (3) and (2), is

$$\delta\Pi = \int_0^\ell [EI\,\kappa\,\delta\kappa - F\sin(\theta+\alpha)\,\delta\theta]\,ds + c\theta_1\,\delta\theta_1, \tag{5}$$

where $\delta\theta$ is the variation of θ, and $\delta\kappa = -d\,\delta\theta/ds$. After integration by parts and from (4), we obtain

$$\delta\Pi = -EI\,\kappa\,\delta\theta|_0^\ell - \int_0^\ell \left[EI\frac{d^2\theta}{ds^2} + F\sin(\theta+\alpha)\right]\delta\theta\,ds + c\theta_1\,\delta\theta_1. \tag{6}$$

Taking $\delta\Pi = 0$, we obtain the differential equation

$$EI\frac{d^2\theta}{ds^2} + F\sin(\theta+\alpha) = 0, \tag{7}$$

and the following boundary conditions:

$$\kappa(0) = 0, \quad -EI\,\kappa(\ell) + c\theta_1 = 0. \tag{8}$$

Thus, the cantilever equilibrium forms are solutions of the second-order ordinary differential equation (7) subject to boundary conditions (8).

The second variation of Π as given by (3) is

$$\delta^2\Pi = -EI\delta\kappa\,\delta\theta|_0^\ell - \int_0^\ell \left[EI\frac{d^2\delta\theta}{ds^2} + F\cos(\theta+\alpha)\,\delta\theta\right]\delta\theta\,ds + c(\delta\theta_1)^2. \tag{9}$$

Taking $\delta^2\Pi = 0$, we obtain the Jacobi accessory equation

$$EI\frac{d^2\delta\theta}{ds^2} + F\cos(\theta+\alpha)\,\delta\theta = 0, \tag{10}$$

and the following boundary conditions, which are consistent with (8):

$$\delta\kappa_0 = 0, \quad -EI\,\delta\kappa(\ell) + c\,\delta\theta(\ell) = 0. \tag{11}$$

We recall that by the Jacobi test, the equilibrium shape of the beam is unstable if any nontrivial solution of (10) under the boundary conditions (11) has a solution (conjugate points) for $0 < s \le \ell$.

3. Solution

In the following, we will use the Jacobian elliptic functions $\mathrm{sn}(x,k)$, $\mathrm{cn}(x,k)$, $\mathrm{dn}(x,k)$, Jacobi's epsilon function $\varepsilon(x,k) \equiv \int_0^x \mathrm{dn}^2(t,k)\,dt$, and complete elliptic integral of the first kind $K(k)$. Further, we will use the following derived Jacobian elliptic function: $\mathrm{sd}(x,k) \equiv \mathrm{sn}(x,k)/\mathrm{dn}(x,k)$ and $\mathrm{cd}(x,k) \equiv \mathrm{cn}(x,k)/\mathrm{dn}(x,k)$ [Reinhardt and Walker 2010].

3.1. ***Equilibrium.*** We introduce the nondimensional parameters

$$\omega^2 \equiv \frac{F\ell^2}{EI}, \quad \beta^2 \equiv \frac{c\ell}{EI}. \tag{12}$$

Hereinafter, we use ℓ as a unit of length, so we have $0 \le s \le 1$. Note that ω^2 represents nondimensional force. However, in figures and tables, we use the normalized force

$$\frac{F}{F_E} = \frac{\omega^2}{\pi^2}, \tag{13}$$

where $F_E \equiv \pi^2(EI/\ell^2)$ is the Euler critical force for the buckling of a pin-ended column.

Using (12), equations (7) and (8) can be written as

$$\frac{d^2\theta}{ds^2} + \omega^2 \sin(\theta + \alpha) = 0, \tag{14}$$

$$\kappa(0) = 0, \quad -\ell\kappa(1) + \beta^2\theta_1 = 0. \tag{15}$$

The solution of (14) is [Batista 2014; 2016; Love 1944; Goss 2003]

$$\theta = -\alpha + 2\sin^{-1}[k\,\mathrm{sn}(\omega s + C, k)], \tag{16}$$

where C is a constant of integration, and k is the elliptic modulus. The base curve curvature is determined from (4) as

$$\ell\kappa = -2\kappa\omega\,\mathrm{cn}(\omega s + C, k). \tag{17}$$

From (17), (16), and (15), we obtain the relations

$$\mathrm{cn}(C, k) = 0, \tag{18}$$

$$-\tfrac{1}{2}\alpha + \sin^{-1}[k\,\mathrm{sn}(\omega + C, k)] + \frac{\kappa\omega}{\beta^2}\,\mathrm{cn}(\omega + C, k) = 0. \tag{19}$$

From these we obtain

$$C = K(\kappa), \tag{20}$$

$$-\tfrac{1}{2}\alpha + \sin^{-1}[k\,\mathrm{cd}(\omega, k)] - \frac{k\sqrt{1-k^2}\,\omega}{\beta^2}\,\mathrm{sd}(\omega, k) = 0. \tag{21}$$

In this manner, we reduce the problem to solving (21) for an unknown k; the equation can be solved numerically. Finally, substituting (16) in (1) and by integrating the equation, we obtain the coordinates of the points of the beam base curve

$$x = \xi\cos\alpha + \eta\sin\alpha, \quad y = -\xi\sin\alpha + \eta\cos\alpha, \tag{22}$$

where

$$\xi = \frac{2}{\omega}[\varepsilon(\omega + C, k) - \varepsilon(\omega s + C, k)] - (1 - s), \tag{23}$$

$$\eta = \frac{2k}{\omega}[\mathrm{cn}(\omega s + C, k) - \mathrm{cn}(\omega + C, k)]. \tag{24}$$

3.2. ***Stability.*** Using (12), from (10) and (11) we obtain the Jacobi accessory equation in the following form [Fox 1954]:

$$\frac{d^2\vartheta}{ds^2} + \omega^2 \cos(\theta+\alpha)\vartheta = 0, \tag{25}$$

where $\vartheta \equiv \delta\theta$. The corresponding boundary conditions (11) can be written as

$$\frac{d\vartheta}{ds}(0) = 0, \quad \left(\frac{d\vartheta}{ds} + \beta^2\vartheta\right)(s_c) = 0, \tag{26}$$

where s_c is an unknown upper value of the normalized arc parameter. The solution of (25) can be expressed as [Batista 2015a]

$$\vartheta(s) = C_1\vartheta_1(s) + C_2\vartheta_2(s), \tag{27}$$

where C_1, C_2 are the constants of integration and

$$\vartheta_1 \equiv \frac{\partial\theta}{\partial C} = 2k\,\mathrm{cn}(\omega s+C, k), \tag{28}$$

$$\vartheta_2 \equiv \frac{\partial\theta}{\partial k} = \frac{2}{1-k^2}\Big\{\mathrm{sn}(\omega s+C, k)\,\mathrm{dn}(\omega s+C, k) - [\varepsilon(\omega s+C, k) - (1-k^2)(\omega s+C)]\,\mathrm{cn}(\omega s+C, k)\Big\}. \tag{29}$$

Substituting (27) in the boundary conditions (26), we obtain a homogeneous system of equations for C_1 and C_2, which has a nontrivial solution if its determinate vanishes. This condition leads to the following equation for s_c:

$$[\varepsilon(\omega s_c, k) - (1-k^2)\omega s_c]\left[\mathrm{sn}(\omega s_c, k) + \frac{\omega}{\beta^2}\,\mathrm{cd}(\omega s_c, k)\right] + \mathrm{cn}(\omega s_c, k)\,\mathrm{dn}(\omega s_c, k) - (1-k^2)\frac{\omega}{\beta^2}\,\mathrm{sn}(\omega s_c, k) = 0, \tag{30}$$

where we omit the factor $k\omega$. By Jacobi's test [Fox 1954], the necessary condition for $\delta^2\Pi > 0$ is that the smallest root of this equation is $s_c > 1$. Therefore, if $0 < s_c \le 1$, the beam shape is unstable. From the stability analysis, we note that α is not included. This should be clear from the expressions of the beam coordinates (22); α only affects the rod position and not its shape.

To verify the above equations, we consider the case $\beta^2 = \infty$ (clamped cantilever). In this case, (21) is reduced to the well-known expression $\mathrm{cn}(\omega, k) = 0$; therefore, $\omega = (2n-1)\,K(k)$, where n is an integer. In addition, (30) becomes the equation for the cantilever [Batista 2015a, Equation 21] (with the first "−" sign corrected to "+").

4. Examples

Using the above solution, we can easily construct various bifurcation diagrams and load-deflection diagrams. Further, we can calculate a deformed beam shape. The stability of the beam shapes can be treated by a numerical solution of (30) through the procedure described by Batista [2015b]. For all numerical calculations with elliptic functions, we use Elfun18 library [Batista 2018].

To verify the present solution, we compare our calculations for the beam's free end coordinates and the tangent angle at the beam ends with those of Ohtsuki and Yasui [1994]. The results are summarized

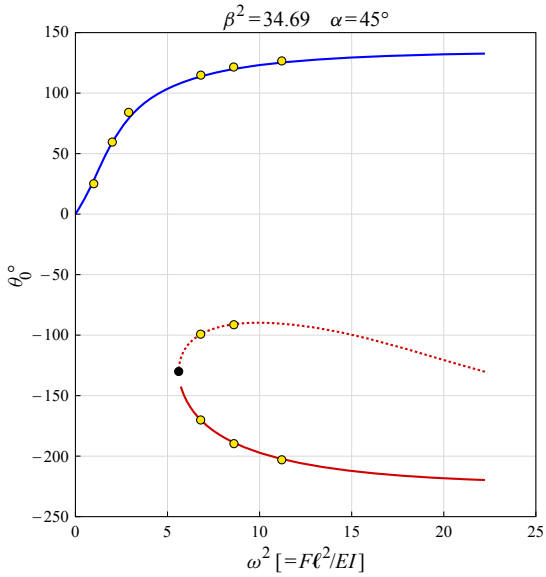

Figure 2. Free end tangent angle as a function of normalized force. Dotted line represents an unstable solution branch. Bright dots indicate values from [Ohtsuki and Yasui 1994]. Critical normalized force is 5.6071, corresponding free end $-130.012°$, represented by the black dot.

in Figure 3, bottom; the values have an acceptable difference of 10% for all cases, except for $\omega^2 = 1$, where the difference is up to 20%. The comparison is also shown in Figure 2.

As an example of the application of the present solution, we consider the case $\beta^2 = \frac{1}{2}\pi^2$ and $\alpha = \frac{1}{4}\pi$. The bifurcation diagram for this case is shown in Figure 3. Each branch starts where $dk/d\omega = 0$. Using (21),

$$\left(1 + \frac{1}{\beta^2}\right) \mathrm{sn}(\omega, k) + \frac{\omega}{\beta^2}\, \mathrm{cd}(\omega, k) = 0. \tag{31}$$

Thus, the start point of the branch is the solution of the system of equations (21) and (31). For each branch, we have two solutions, i.e., each branch is split into two, $k > 0$ (upper) and $k < 0$ (lower). From the figure, we see that only the first branch can be stable; all other branches are unstable. The upper part of the first branch that emerges from the initial beam is completely stable (Figure 4, left). The lower part can only be attained by applying a force greater than the critical force to some predeformed shape (Figure 4, right). Note that this part is unstable from point A to B (see Figure 3). The stationary point of the lower part is at $d\omega/dk = 0$. For this condition, using (21), we obtain an equation, which is the same as (30) for $s_c = 1$, i.e., the stationary point lies on the boundary of the stable region. Thus, we obtain the critical value of ω and k by a solution of the system of equations (21) and (30).

We observe similar behavior for other values of β^2 and α. For $\beta^2 = \infty$, we obtain the solution for the clamped beam, which is discussed by Batista [2015b]. Thus, we conclude that, in general, only the first branch of the spring-hinged cantilever beam can be stable; all other branches are unstable.

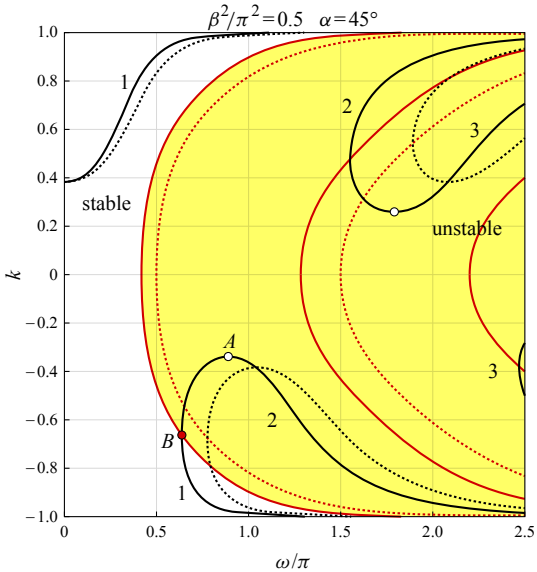

$F\ell^2/EI$	[Ohtsuki and Yasui 1994] x_0/ℓ	y_0/ℓ	θ_0°	θ_1°	present x_0/ℓ	y_0/ℓ	θ_0°	θ_1°	relative difference % x_0/ℓ	y_0/ℓ	θ_0°	θ_1°
1	0.951	0.258	25.1	1.2	0.93611	0.32338	28.013	1.471	1.6	−20.2	−10.4	−18.4
2	0.750	0.601	59.5	3.0	0.72701	0.62366	59.184	3.155	3.2	−3.6	0.5	−4.9
2.9	0.561	0.752	84.0	4.8	0.53216	0.75927	78.919	4.374	5.4	−1.0	6.4	9.7
6.8	0.099	0.856	114.8	7.5	0.09051	0.86115	113.691	7.558	9.4	−0.6	1.0	−0.8
11.2	−0.105	0.842	126.6	10.2	−0.10100	0.84792	125.142	9.770	4.0	−0.7	1.2	4.4

Figure 3. Top: bifurcation diagram with two solution branches. Dotted lines indicate the clamped cantilever beam. Start point A of the lower part of the first branch is at $(0.88888, -0.33870)$. This part of the branch becomes stable after passing point B, which is at $(0.63713, -0.66276)$. Bottom: numerical values for column shapes shown in top graph: $\beta^2 = 34.69$, $\alpha = \frac{1}{4}\pi$.

For the last example, we consider the spring-hinged cantilever beam under pure compression. From the graph of critical force in Figure 5, we see that the effect of the spring is relatively small for $\beta^2 > 40$ wherever it is less than 5% of critical force for the clamped beam. From the graph in Figure 6, we can see that after buckling, the beam continues to support the load, i.e., the force still increases with an increase in the deflection. From the bifurcation diagram in Figure 7, we see that only the first buckled form is stable; all other shapes are unstable. Some stable shapes are shown in Figure 8.

We demonstrate the stability of the beam with the graphs; however, two cases can be treated analytically. The first case is a straight beam, and the second case considers a beam with small deflections.

The solution of (21) corresponding to the straight form is $k = 0$. In this case, from (16), (17), (23), and (24), we obtain

$$\theta = 0, \quad \kappa = 0, \quad x = 1 - s, \quad y = 0. \tag{32}$$

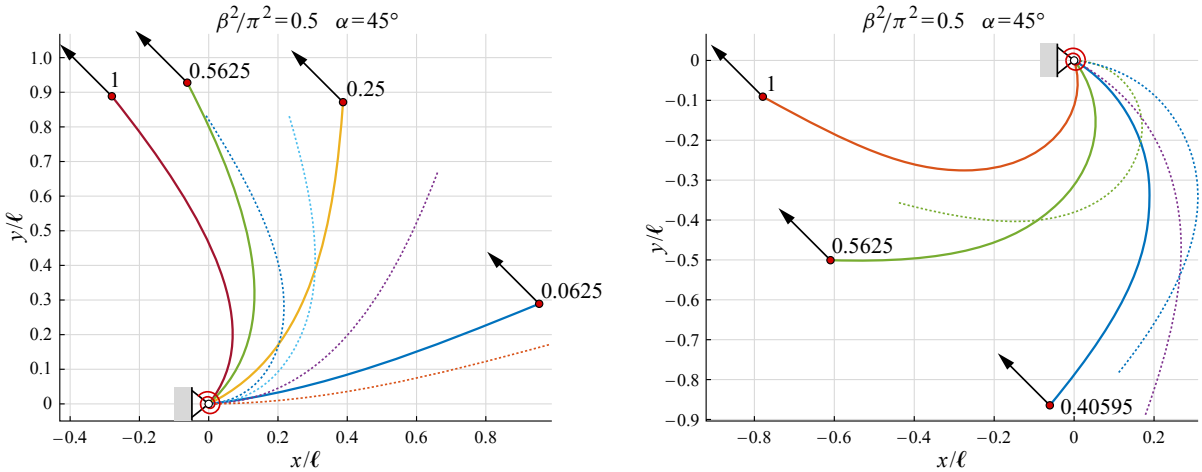

ω/π	k	F/F_E	x_0/ℓ	y_0/ℓ	θ_0°	θ_1°
0.25	0.55357	0.0625	0.95367	0.28915	22.224	6.294
0.5	0.90653	0.25	0.38751	0.87127	85.062	25.499
0.75	0.98578	0.5625	−0.06172	0.92742	115.655	39.457
1	0.99770	1	−0.27987	0.88885	127.221	49.345

ω/π	k	F/F_E	x_0/ℓ	y_0/ℓ	θ_0°	θ_1°
0.63714	−0.66642	**0.40595**	−0.06048	−0.86397	−128.583	−30.412
0.75	−0.92533	0.5625	−0.60967	−0.49959	−180.436	−50.558
1	−0.99022	1	−0.77905	−0.09016	−208.963	−70.431

Figure 4. Top: stable equilibrium shapes for various values of F/F_E. Dotted lines indicate the shapes (left) and forms (right) for the clamped cantilever. Middle: numerical values for the beam shapes shown in top-left graph. Bottom: Numerical values for column shapes shown in top-right graph. Bold indicates the critical force. $\beta^2 = \frac{1}{2}\pi^2$ and $\alpha = \frac{1}{4}\pi$ for both graphs.

To determine straight-form stability, we consider (30), which for $k = 0$ reduces to

$$-\frac{\omega}{\beta^2}\sin(\omega s_c) + \cos(\omega s_c) = 0. \tag{33}$$

The solution to this equation is $s_c = (1/\omega)\tan^{-1}(\beta^2/\omega)$. For $s_c = 1$, it becomes the well-known characteristic equation for the critical value ω_c of ω [Alfutov 2000]:

$$\beta^2 = \omega_c \tan\omega_c. \tag{34}$$

Thus, the straight beam is stable for $\omega < \omega_c$. In particular, if $\beta^2 = 0$ (no spring), $\omega_c = 0$, i.e., the straight beam is unstable. If $\beta^2 = \infty$ (clamped end), $\omega_c = \frac{1}{2}\pi$. The graph from (34) is shown in Figure 6.

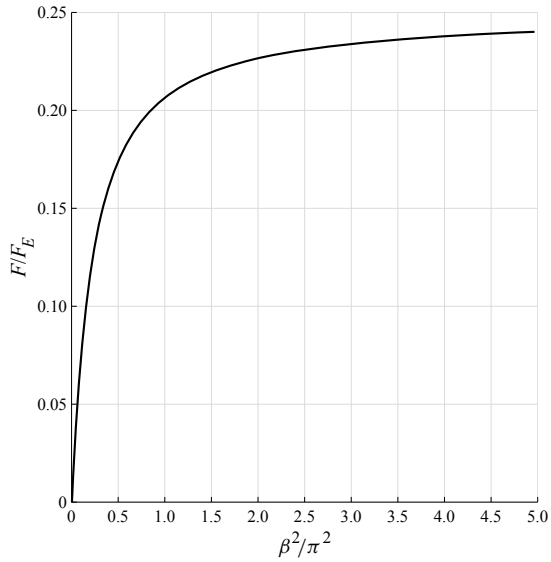

Figure 5. Critical force F/F_E versus spring stiffness β^2 for the spring-hinged cantilever beam under pure compression: $F/F_E \to \frac{1}{4}$ as $\beta^2 \to \infty$.

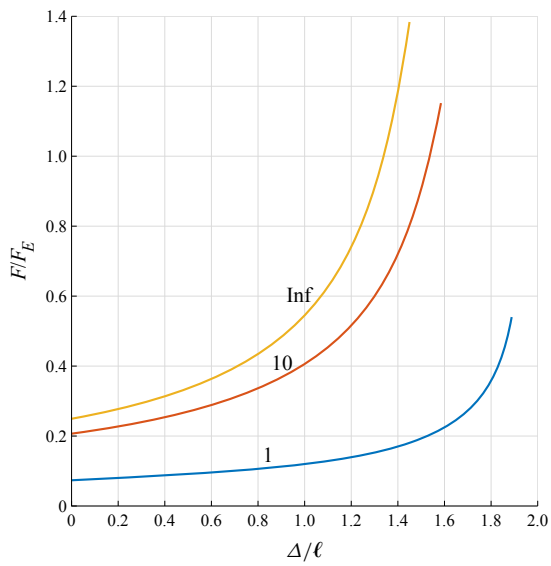

Figure 6. Load-deflection diagram for beam under compression for various values of normalized spring stiffness β^2.

For a small k, i.e., a small deflection, from (20) and (21), we obtain

$$C = \tfrac{1}{2}\pi + O(k^2), \tag{35}$$

$$\frac{\omega}{\omega_0} = 1 + \tfrac{1}{12}\omega_2\, k^2 + O(k^4), \tag{36}$$

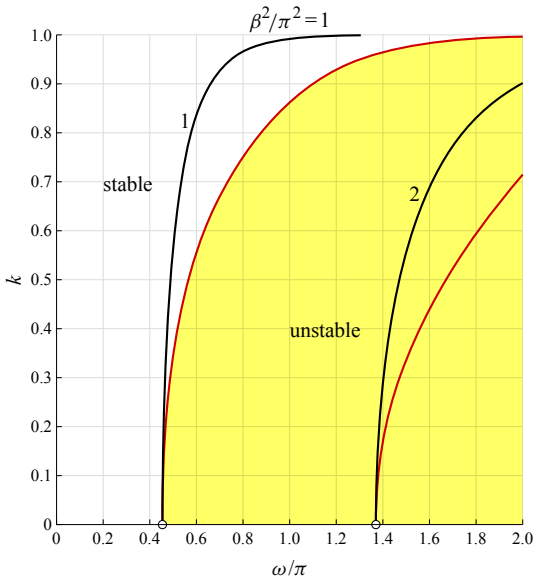

Figure 7. Bifurcation diagram with the first two branches for the cantilever beam under pure compression.

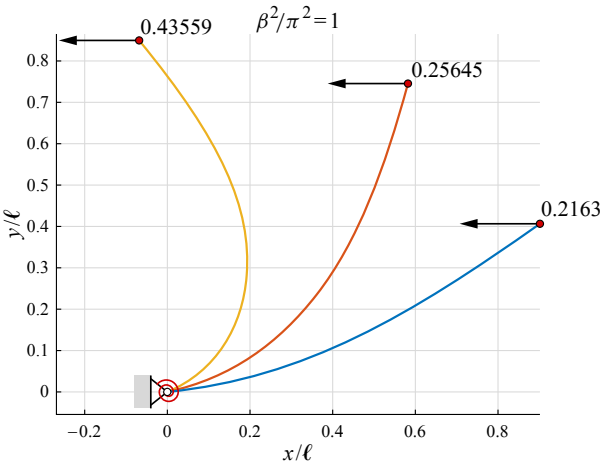

k	ω	F/F_E	$\Delta/\ell = 1 - x_0/\ell$	y_0/ℓ
0	**1.427187**	0.206377	0	0
0.3	1.461077	0.216295	0.100091	0.406231
0.6	1.590929	0.256449	0.417597	0.744692
0.9	2.073437	0.435594	1.067300	0.849782

Figure 8. Left: equilibrium shapes for various values of F/F_E. Right: numerical values for column shapes shown on left. Bold indicates the critical value and $\beta^2 = \pi^2$.

where

$$\omega_2 = \frac{3\omega_0^4 + (5+6\beta^2)\beta^2\omega_0^2 + 3\beta^6(1+\beta^2)}{(\omega_0^2+\beta^4)(\omega_0^2+\beta^4+\beta^2)}, \tag{37}$$

and ω_0 is the solution of

$$-\frac{\omega_0}{\beta_0}\sin\omega_0 + \cos\omega_0 = 0. \tag{38}$$

From (16), (17), (23), and (24) we have

$$\theta = 2k\cos(\omega_0 s) + O(k^3), \tag{39}$$

$$\kappa = 2k\omega_0 \sin(\omega_0 s) + O(k^3), \tag{40}$$

$$x = 1 - s + O(k^2), \tag{41}$$

$$y = \frac{2k}{\omega_0}[\sin\omega_0 - \sin(\omega_0 s)] + O(k^3). \tag{42}$$

To assess the stability of a small deflection, we substitute $s_c = 1$ in (30) and express the equation as a power series of k. In this manner, we obtain

$$\frac{\omega_c}{\omega_0} = 1 + \tfrac{1}{4}\omega_2 k^2 + O(k^4). \tag{43}$$

Comparing (36) and (43), we find that $\omega < \omega_c$, i.e., the initial deflected form is stable.

5. Follower force

We obtain a solution for a large deflection of the rod under a follower force by setting [Antman 2005]

$$\alpha = \gamma - \theta_0, \tag{44}$$

where θ_0 is the free-end tangent angle, and γ is the angle between the force and the base curve tangent at the free end. Substituting this in (16) and setting $s = 0$, we obtain

$$k = \sin\tfrac{1}{2}\gamma. \tag{45}$$

Substituting (44) into the characteristic equation (21), we obtain the following equation for the tangent angle at the free end:

$$\theta_0 = \gamma - 2\sin^{-1}[k\,\mathrm{cd}(\omega, k)] + \frac{2k\sqrt{1-k^2}\,\omega}{\beta^2}\,\mathrm{sd}(\omega, k). \tag{46}$$

Thus, for each ω and γ, we can calculate k from (45), θ_0 from (46), and α from (44). In other words, the problem has a unique solution, i.e., an equilibrium form of the spring-hinged cantilever under a follow force is unique. This generalizes the results of Antman [2005], where $\beta^2 = \infty$ and $\gamma = 0$.

The angle θ_0 is constant when $d\theta_0/d\omega = 0$. From this condition, we deduce the following equation:

$$\mathrm{sd}(\omega, k) + \omega\,\mathrm{cd}(\omega, k) + \beta^2\,\mathrm{sn}(\omega, k) = 0. \tag{47}$$

For example, when $\beta^2 = \infty$, Equation (47) reduces to $\mathrm{sn}(\omega, k) = 0$. The smallest positive root of this equation is $\omega = 2K(k)$. For $\gamma = \frac{1}{2}\pi$, we obtain $\omega = 3.70815$ or $F_c = 13.75037$. The difference between this value and that of Shvartsman [2007] is less than 0.3%. Note that when $\omega = 2K(k)$, $\mathrm{cn}(\omega, k) = -1$, and $\mathrm{dn}(\omega, k) = 1$; therefore, (46) reduces to $\theta_0 = 2\gamma$, i.e., it is independent of β^2. This can be observed in Figure 9. To obtain the value of β^2 for which $\theta_{0,\max} = 2\pi$, we substitute β^2 from (47) into (46). We get $\omega = 2.52909$ as a solution of the resulting equation; thus, $\beta^2 = 0.74324$.

Because the follower problem has a unique solution, we may assume that the cantilever beam subjected to a static tangential follower force cannot lose stability simply because there are no neighboring

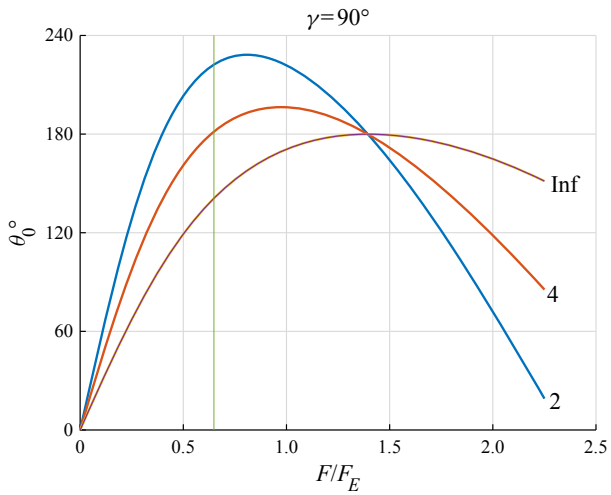

Figure 9. Free end tangent angle θ_0 as a function of normalized follower force F/F_E for various values of normalized spring stiffness β^2. The maximum value of θ_0 when $\beta^2 = 0$ is at $F/F_E = 0.64807$.

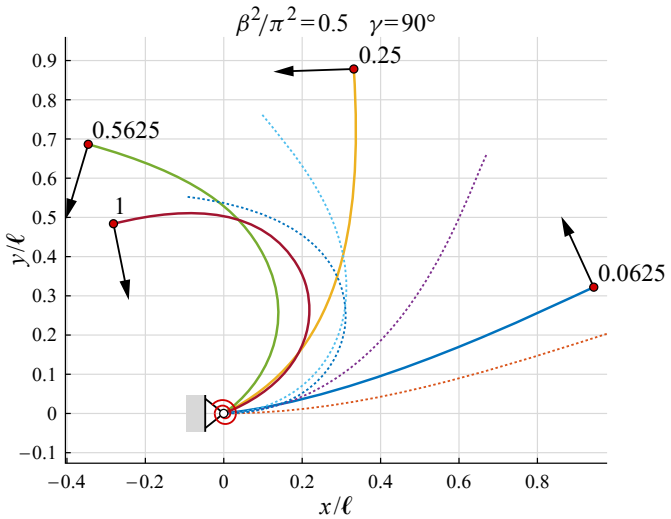

ω/π	F/F_E	x_0/ℓ	y_0/ℓ	θ_0°	θ_1°
0.25	0.0625	0.94249	0.32144	24.710	7.094
0.5	0.25	0.33137	0.87781	92.127	24.778
0.75	0.5625	−0.34491	0.68558	163.135	34.097
1	1	−0.28124	0.48360	191.425	20.612

Figure 10. Top: equilibrium shapes of a spring-supported cantilever for various values of follower force. Dotted lines indicate the corresponding clamped cantilever beam. Bottom: numerical values for beam shapes shown on top. Note that $\beta^2 = \frac{1}{2}\pi^2$, $\gamma = \frac{1}{2}\pi$, $k = \sqrt{2}/2$.

equilibrium shapes. However, it is well-known that the uniqueness of the solution does not imply stability [Antman 2005; Bolotin 1963]. Thus, it is widely accepted that for a follower force, a loss of stability is dynamic; therefore, its stability conditions should be determined by considering small oscillations about the equilibrium state [Elishakoff 2005].

6. Conclusions

For the spring-hinged cantilever beam under pure compression, we prove that the first buckled mode is unconditionally stable, i.e., the beam retains its loading capacity after buckling; all higher buckling modes are unstable. The spring-hinged cantilever beam under an inclined force has two stable equilibrium solutions. A completely stable solution is obtained for the initial state, and a partly stable solution is obtained for a predeformed state. We also provide an analytical solution for a cantilever subjected to a follower force.

Finally, we note that, for a closed form analytical solution, we have an entire phase plane, from which we can easily determine the equilibrium conditions and their stability.

References

[Alfutov 2000] N. A. Alfutov, *Stability of elastic structures*, Springer, Berlin, 2000.

[Antman 2005] S. S. Antman, *Nonlinear problems of elasticity*, 2nd ed., Springer, New York, 2005.

[Armanini et al. 2017] C. Armanini, F. D. Corso, D. Misseroni, and D. Bigoni, "From the elastica compass to the elastica catapult: an essay on the mechanics of soft robot arm", *Proc. Royal Soc. A* **473**:2198 (2017), art. id. 20160870.

[Batista 2014] M. Batista, "Analytical treatment of equilibrium configurations of cantilever under terminal loads using Jacobi elliptical functions", *Int. J. Solids Struct.* **51**:13 (2014), 2308–2326.

[Batista 2015a] M. Batista, "A simplified method to investigate the stability of cantilever rod equilibrium forms", *Mech. Res. Commun.* **67** (2015), 13–17.

[Batista 2015b] M. Batista, "On stability of elastic rod planar equilibrium configurations", *Int. J. Solids Struct.* **72** (2015), 144–152.

[Batista 2016] M. Batista, "A closed-form solution for Reissner planar finite-strain beam using Jacobi elliptic functions", *Int. J. Solids Struct.* **87** (2016), 153–166.

[Batista 2018] M. Batista, "Elfun18 — a collection of Matlab functions for the computation of elliptical integrals and Jacobian elliptic functions of real arguments", preprint, 2018. arXiv

[Bigoni 2015] D. Bigoni (editor), *Extremely deformable structures*, Springer, Wien, 2015.

[Bigoni et al. 2018] D. Bigoni, O. N. Kirillov, D. Misseroni, G. Noselli, and M. Tommasini, "Flutter and divergence instability in the Pflüger column: experimental evidence of the Ziegler destabilization paradox", *J. Mech. Phys. Solids* **116** (2018), 99–116.

[Bolotin 1963] V. V. Bolotin, *Nonconservative problems of the theory of elastic stability*, Pergamon, Oxford, 1963.

[Elishakoff 2005] I. Elishakoff, "Controversy associated with the so-called "follower forces": critical overview", *Appl. Mech. Rev.* (*ASME*) **58**:2 (2005), 117–142.

[Fox 1954] C. Fox, *An introduction to the calculus of variations*, Oxford University Press, 1954.

[Frisch-Fay 1962] R. Frisch-Fay, *Flexible bars*, Butterworths, London, 1962.

[Glavardanov et al. 2017] V. B. Glavardanov, R. B. Maretic, M. M. Zigic, and N. M. Grahovac, "Secondary bifurcation of a shearable rod with nonlinear spring supports", *Eur. J. Mech. A Solids* **66** (2017), 433–445.

[Goss 2003] V. G. A. Goss, *Snap buckling, writhing and loop formation in twisted rods*, Ph.D. thesis, University Collage London, 2003, Available at https://tinyurl.com/Goss-thesis.

[Guran and Plaut 1993] A. Guran and R. H. Plaut, "Stability of a column with a follower load and a load-dependent elastic support", *Acta Mech.* **97**:3-4 (1993), 205–214.

[Kar and Sujata 1990] R. C. Kar and T. Sujata, "Parametric instability of an elastically restrained cantilever beam", *Comput. Struct.* **34**:3 (1990), 469–475.

[Koiter 1996] W. T. Koiter, "Unrealistic follower forces", *J. Sound Vib.* **194**:4 (1996), 636.

[Love 1944] A. E. H. Love, *A treatise on the mathematical theory of elasticity*, 4th ed., Dover Publications, New York, 1944.

[Mahnken 2015] R. Mahnken, *Lehrbuch der Technischen Mechanik — Elastostatik Mit einer Einführung in Hybridstrukturen*, Springer, Berlin, 2015.

[Ohtsuki and Yasui 1994] A. Ohtsuki and T. Yasui, "Analysis of large deflections in ppring-hinged cantilever beam under inclined tip load", *Trans. Japan Soc. Mech. Eng. A* **60**:577 (1994), 2100–2106.

[O'Reilly 2017] O. M. O'Reilly, *Modeling nonlinear problems in the mechanics of strings and rods: the role of the balance laws*, Springer, 2017.

[Popov 1986] E. P. Popov, *Theory and calculation of flexible elastic rods*, Moscow, 1986. In Russian.

[Rao and Raju 1979] G. V. Rao and P. C. Raju, "Post-buckling analysis of spring-hinged cantilever columns", *Comput. Struct.* **10**:3 (1979), 495–497.

[Rao and Raju 2002] G. V. Rao and K. K. Raju, "Stability of spring-hinged cantilever column under combined concentrated and distributed loads", *AIAA J.* **40**:8 (2002), 1687–1689.

[Rao and Rao 1975] G. V. Rao and R. V. N. Rao, "Stability of spring-hinged cantilever columns subjected to follower forces — a galerkin finite element solution", *Comput. Struct.* **5**:4 (1975), 261–262.

[Rao and Rao 1987] B. N. Rao and G. V. Rao, "Large deflections of a spring-hinged tapered cantilever beam with a rotational distributed loading", *Aeronaut. J.* **91**:909 (1987), 429–437.

[Rao et al. 1987] B. N. Rao, G. L. N. Babu, and G. V. Rao, "Large deflection analysis of a spring hinged cantilever beam subjected to a tip concentrated rational load", *Z. Angew. Math. Mech.* **67**:10 (1987), 519–520.

[Reinhardt and Walker 2010] W. P. Reinhardt and P. L. Walker, "Jacobian Elliptic Functions", in *NIST handbook of mathematical functions*, edited by F. W. J. Olver et al., Cambridge University Press, New York, 2010.

[Rzhanitsyn 1955] A. R. Rzhanitsyn, *Stability of equilibrium of elastic systems*, State publishing house of technical-theoretical literature, Moscow, 1955. In Russian.

[Sankaran and Rao 1976] G. V. Sankaran and G. V. Rao, "Stability of tapered cantilever columns subjected to follower forces", *Comput. Struct.* **6**:3 (1976), 217–220.

[Shvartsman 2007] B. S. Shvartsman, "Large deflections of a cantilever beam subjected to a follower force", *J. Sound Vib.* **204**:3-5 (2007), 969–973.

[Simitses and Hodges 2006] G. J. Simitses and D. H. Hodges, *Fundamentals of structural stability*, Elsevier, Amsterdam, 2006.

[Timoshenko 1961] S. Timoshenko, *Theory of elastic stability*, 2nd ed., McGraw-Hill, New York, 1961.

[Zakharov et al. 2004] Y. V. Zakharov, K. G. Okhotkin, and A. D. Skorobogatov, "Bending of bars under a follower load", *J. Appl. Mech. Tech. Phys.* **45**:5 (2004), 756–763.

[Zhang and Shan 2008] N.-H. Zhang and J.-Y. Shan, "An energy model for nanomechanical deflection of cantilever-DNA chip", *J. Mech. Phys. Solids* **56**:6 (2008), 2328–2337.

[Ziegler 1977] H. Ziegler, *Principles of structural stability*, 2nd ed., Birkhäuser, Basel, Stuttgart, 1977.

Received 7 Jan 2019. Revised 4 Apr 2019. Accepted 8 Apr 2019.

MILAN BATISTA: milan.batista@fpp.uni-lj.si
Faculty of Maritime Studies, University of Ljubljana, Slovenia

SUBMISSION GUIDELINES

ORIGINALITY

Authors may submit manuscripts in PDF format online at the Submissions page. Submission of a manuscript acknowledges that the manuscript is original and has neither previously, nor simultaneously, in whole or in part, been submitted elsewhere. Information regarding the preparation of manuscripts is provided below. Correspondence by email is requested for convenience and speed. For further information, write to contact@msp.org.

LANGUAGE

Manuscripts must be in English. A brief abstract of about 150 words or less must be included. The abstract should be self-contained and not make any reference to the bibliography. Also required are keywords and subject classification for the article, and, for each author, postal address, affiliation (if appropriate), and email address if available. A home-page URL is optional.

FORMAT

Authors can use their preferred manuscript-preparation software, including for example Microsoft Word or any variant of TEX. The journal itself is produced in LATEX, so accepted articles prepared using other software will be converted to LATEX at production time. Authors wishing to prepare their document in LATEX can follow the example file at www.jomms.net (but the use of other class files is acceptable). At submission time only a PDF file is required. After acceptance, authors must submit all source material (see especially Figures below).

REFERENCES

Bibliographical references should be complete, including article titles and page ranges. All references in the bibliography should be cited in the text. The use of BibTEX is preferred but not required. Tags will be converted to the house format (see a current issue for examples); however, for submission you may use the format of your choice. Links will be provided to all literature with known web locations; authors can supply their own links in addition to those provided by the editorial process.

FIGURES

Figures must be of publication quality. After acceptance, you will need to submit the original source files in vector format for all diagrams and graphs in your manuscript: vector EPS or vector PDF files are the most useful. (EPS stands for Encapsulated PostScript.)

Most drawing and graphing packages—Mathematica, Adobe Illustrator, Corel Draw, MATLAB, etc.—allow the user to save files in one of these formats. Make sure that what you're saving is vector graphics and not a bitmap. If you need help, please write to graphics@msp.org with as many details as you can about how your graphics were generated.

Please also include the original data for any plots. This is particularly important if you are unable to save Excel-generated plots in vector format. Saving them as bitmaps is not useful; please send the Excel (.xls) spreadsheets instead. Bundle your figure files into a single archive (using zip, tar, rar or other format of your choice) and upload on the link you been given at acceptance time.

Each figure should be captioned and numbered so that it can float. Small figures occupying no more than three lines of vertical space can be kept in the text ("the curve looks like this:"). It is acceptable to submit a manuscript with all figures at the end, if their placement is specified in the text by means of comments such as "Place Figure 1 here". The same considerations apply to tables.

WHITE SPACE

Forced line breaks or page breaks should not be inserted in the document. There is no point in your trying to optimize line and page breaks in the original manuscript. The manuscript will be reformatted to use the journal's preferred fonts and layout.

PROOFS

Page proofs will be made available to authors (or to the designated corresponding author) at a Web site in PDF format. Failure to acknowledge the receipt of proofs or to return corrections within the requested deadline may cause publication to be postponed.

Journal of Mechanics of Materials and Structures

Volume 14, No. 2 March 2019